

THE MAGNETIC CHARACTERIZATION OF PERMALLOY AND PERMALLOY
OXIDE GROWN BY RF MAGNETRON SPUTTERING

by

Binod D.C., M.Sc.

A thesis submitted to the Graduate Council of
Texas State University in partial fulfillment
of the requirements for the degree of
Master of Science
with a Major in Physics
December 2019

Committee Members:

Wilhelmus J. Geerts, Chair

David Donnelly

Luisa M Scolfaro

Erik Samwel

COPYRIGHT

by

Binod D.C.

2019

FAIR USE AND AUTHOR'S PERMISSION STATEMENT

Fair Use

This work is protected by the Copyright Laws of the United States (Public Law 94-533, section107), Consistent with fair use as defined in the Copyright Laws, brief quotations from this material are allowed with proper acknowledgment. Use of this material for financial gain without the author's express written permission is not allowed.

Duplication Permission

As the copyright holder of this work I, Binod D.C., authorize duplication of this work, in whole or in part, for educational or scholarly purposes only.

ACKNOWLEDGMENTS

Foremost, I would like to express my sincere gratitude to my advisor Dr. Ir. Wilhelmus J. Geerts for the continuous support of my Master study and research, for his patience, motivation, enthusiasm and immense knowledge. The door to professor Geerts was always open whenever I ran into a trouble spot or had a question about my research or writing. He consistently allowed this thesis to be my own work but steered me in the right direction whenever he thought I needed it. I would also like to thank my committee members Dr. David Donnelly, Dr. Ir. Erik Samwel (MicroSense) and Dr. Luisa Scolfaro for serving my thesis committee. Furthermore, I would like to thank Sarah Beth Ragan (Dripping Springs High School) for helping me with magnetic characterization, Anival Ayala (MSEC Texas State), Ghatak-Roy Amiya (Cerium Labs) and Tim Hossain (Cerium Labs) for helping me with XPS characterization, Dr. Casey Smith (ARSC), Barry D Koehne (ARSC) and John Miracle (ARSC) for training me on the equipment and solving instrumental problems. I am grateful to my family and friends for their encouragement and motivations all these years of my study. I would like to acknowledge travel support of the Department of Physics, the College of Science, and the graduate college of Texas State University through the course of my thesis project. I acknowledge financial support from DOD (HBCU/MI grant W911NF-15-1-0394) and by an NSF grant via a DMR-MRI grant (award 1726970).

Part of this thesis was published in the following paper:

[1] Binod D.C., Andres A. Oliva, Anival Ayala, Shankar Acharya, Fidele Twagirayezu, James Nick Talbert, Luisa M. Scolfaro, and Wilhelmus J. Geerts, “Magnetic Properties of reactive co-sputtered NiFe-oxide samples”, IEEE Transactions on Magnetism, vol. 55, no. 2, February 2019.

Furthermore, part of the thesis was presented at the following conferences:

[1] Binod D.C., Andres Oliva, James, Anival Ayala, Shankar Acharya, Fidele Twagirayezu, James Nick Talbert, Luisa Scolfaro, Wilhelmus J. Geerts, “Magnetic Properties of NiFe-oxide samples”, poster presentation at TSAPS spring-2018, Tarleton State University in Stephenville.

[2] Binod D.C., Andres Oliva, James, Anival Ayala, Shankar Acharya, Fidele Twagirayezu, James Nick Talbert, Luisa Scolfaro, Wilhelmus Geerts, “Magnetic properties of reactive sputtered NiFe-oxide sample”, poster presentation at the 2018 International Conference on Magnetism in San Francisco.

[3] Binod D.C, Wilhelmus Geerts, Luisa Scolfaro, “Pole figure measurement on RF-sputtered Ni_{0.81}Fe_{0.19} Thin films”, poster presentation at TSAPS spring-2019, F. Austin State University in Nacogdoches.

TABLE OF CONTENTS

| | Page |
|--|-------------|
| ACKNOWLEDGMENTS | iv |
| LIST OF FIGURES | ix |
| LIST OF TABLES | xvi |
| LIST OF SYMBOLS | xvii |
| ABSTRACT | xviii |
| CHAPTER | |
| 1 INTRODUCTION | 1 |
| 1.1 Motivation | 1 |
| 1.2 Magnetic materials | 3 |
| 1.3 Literature review of the texture and magnetic properties of NiFe | 6 |
| 1.4 Literature review of the texture and magnetic properties of NiFeO..... | 12 |
| 2 VIBRATING SAMPLE MAGNETOMETER | 17 |
| 2.1 Working principle of Vibrating Sample Magnetometer (VSM) | 17 |
| 2.2 Errors in VSM Measurements | 20 |
| 2.2.1 Background Subtraction..... | 20 |
| 2.2.2 Image effect | 22 |
| 2.2.3 Sample position..... | 24 |
| 2.2.4 Remove Sweep Field Lag | 26 |
| 2.2.5 Angular sensitivity | 27 |
| 2.2.6 Remove Signal Offset | 27 |
| 2.2.7 Remove Signal Drift | 28 |
| 2.2.8 Field Reading Correction..... | 29 |
| 2.2.9 Sensitivity Correction | 29 |
| 2.2.10 Resonance of sample rod system | 30 |
| 2.3 Different parts of VSM..... | 36 |
| 2.3.1 Water-cooled electromagnet | 36 |
| 2.3.2 Vibration head and sample holder (with angle indicator)..... | 37 |
| 2.3.3 Pickup coils | 37 |

| | |
|--|----|
| 2.3.4 Lock-in amplifier | 38 |
| 2.3.5 Computer interface..... | 38 |
| 2.4 Options available in MicroSense Easy VSM | 38 |
| 2.4.1 The VSM Option..... | 38 |
| 2.4.2 The Torque Option..... | 39 |
| 2.4.3 The Temperature Control Option..... | 39 |
| 2.4.4 The Magnetoresistance option | 40 |
| 2.4.5 The MOKE Option | 40 |
| 2.4.6 FMR Option | 40 |
| 2.5 Available Measurement procedures for the VSM | 41 |
| 2.5.1 Virgin Curve | 41 |
| 2.5.2 AC Remanence Measurement..... | 43 |
| 2.5.3 Isothermal Remanence Measurement (IRM)..... | 43 |
| 2.5.4 DC Demagnetization Measurement (DCD)..... | 45 |
| 2.5.5 Hysteresis Loop Measurement..... | 51 |
| 2.5.6 Angular Remanence Measurement (ARM) | 52 |
| 2.5.7 Time-Dependent Measurement..... | 53 |
| 2.5.8 Temperature Scan | 54 |
| 2.5.9 Torque Measurement | 54 |
| 2.5.10 Miyajima Method of Torque Measurement..... | 60 |
| 2.6 Demagnetizing Field Correction of Measured Data..... | 61 |
| | |
| 3 LAB INSTRUMENTS AND RESULTS..... | 63 |
| | |
| 3.1 AJA Magnetron Sputtering System..... | 63 |
| 3.1.1 Sample preparation | 65 |
| 3.1.2 Effect of Oxygen flow on deposition rate..... | 67 |
| 3.2 Physical Property Measurement System | 69 |
| 3.2.1 Measurement procedure..... | 70 |
| 3.2.2 Measurement of magnetic properties of the sample | 71 |
| 3.2.3 Variation of saturation magnetization with oxygen concentration..... | 73 |
| 3.3 X-ray Photoelectron Spectroscopy (XPS) | 75 |
| 3.3.1 XPS Measurement Procedure | 77 |
| 3.3.2 XPS measurement result | 78 |
| 3.4 X-ray Diffractometer (XRD) | 80 |
| 3.4.1 System Preparation and Measurement Methods..... | 81 |
| 3.4.2 The influence of rotation on chi, Phi and Omega to remove the substrate(silicon) peak | 83 |
| 3.4.3 Texture of thin films | 91 |

| | |
|---|-----|
| 4 VSM MEASUREMENTS | 105 |
| 4.1 Measurement Errors in VSM..... | 105 |
| 4.1.1 Effect of sweep speed and integration time in the hysteresis loop measurement | 105 |
| 4.1.2 Effect of the shape of the sample on the angular dependence of the measured saturation magnetic moment | 111 |
| 4.1.3 Effect of the sample position on the measured saturation magnetic moment..... | 114 |
| 4.1.4 Effect of shape and sample position on the measured remanent magnetic moment..... | 115 |
| 4.1.5 Angle dependence of coercivity of a circular floppy sample .. | 118 |
| 4.1.6 Derivation of sensitivity function and cross talk | 119 |
| 4.1.7 Calculation of Sensitivity and cross talk..... | 136 |
| 4.2 VSM Measurement Results | 143 |
| 4.2.1 IRM and DCD Measurement of 3.5” floppy | 143 |
| 4.2.2 IRM and DCD measurement of 3.5” floppy | 144 |
| 4.2.3 IRM and DCD measurement of Ni _{0.81} Fe _{0.19} sample | 147 |
| 4.2.4 Time-Dependent Measurements | 150 |
| 4.2.5 Angle-dependent coercivity of Ni _{0.81} Fe _{0.19} sample..... | 160 |
| 5 OVERALL SUMMARY | 161 |
| REFERENCES | 166 |

LIST OF FIGURES

| Figure | Page |
|---|------|
| 2.1. Illustration of the position of the sample between the coils of electromagnets in VSM. As the sample moves up and down, a flux change in the detection coils will be created. | 18 |
| 2. 2. Signals before background subtraction(red) and after subtraction (black) [35]. | 21 |
| 2. 3. Effect of image correction [41]...... | 23 |
| 2. 4. X-Signal as a function of X-position (left) Y-position (center) and z-position (right) [35]...... | 25 |
| 2. 5. Unloaded 8mm transverse holder (a) 80 Hz: slightly from bottom left to top right (b) 85 Hz: from bottom left to top right, more than 80 Hz. | 36 |
| 2.6. Virgin curve of the demagnetized sample [41]...... | 42 |
| 2. 7. AC remanence measurement [41]...... | 43 |
| 2. 8. IRM measurement procedure [41]...... | 44 |
| 2.9. DCD measurement procedure [45]. | 46 |
| 2. 10. when the projection of M_r on H is zero, M_r is also zero [45]. | 47 |
| 2.11. Hankel plot for gamma-Fe ₂ O ₃ and a Ba-Fe floppy[45]...... | 49 |
| 2.12. delta-M plot for gamma-Fe ₂ O ₃ and a Ba-Fe floppy [45]...... | 50 |
| 2.13. Hysteresis loops for hard and soft magnetic materials [46]...... | 51 |

| | |
|--|----|
| 2. 14. Angular remanence and magnetization angle as a function of field angle for Co- γ Fe ₂ O ₃ VHS tape, Co- γ Fe ₂ O ₃ floppy tape, and ME tape all measured in the plane of the sample [45]..... | 53 |
| 2.15. Angle definition for torque calculation [45]. | 55 |
| 2. 16. Torque as a function of the angle of the magnetization on a gamma-Fe ₂ O ₃ [45]... | 58 |
| 2. 17. The variation of N _x as a function k. | 59 |
| 2. 18. Loop before applying the demagnetizing field (in grey) and after applying the demagnetizing field (in red) [41]..... | 62 |
| 3. 1. AJA sputtering system..... | 63 |
| 3. 2. Deposition rate as a function of the oxygen flow for NiFe-19% co-sputtering at 200 Watt..... | 69 |
| 3. 3. Left to Right: PPMS apparatus (a), VSM attachments for PPMS (b), photograph of the VSM puck (c), a cross-section of VSM puck (d), at Texas State University..... | 72 |
| 3. 4. The sample holder fully covered by the sample (in the middle) + substrate tiles. The effect if the substrate is suppressed since it is longer than the distance between the pick-up coils [54]..... | 73 |
| 3. 5. Variation of saturation magnetization with oxygen concentration for different films. | 74 |

| | |
|---|----|
| 3. 6. Magnetic moment $m(H)$ per unit volume at 300K for NiFeO and NiO samples, sputtered at different O pressure. Shows a decrease in saturation magnetization at higher O pressure..... | 75 |
| 3. 7. XPS measurement procedure on NiFeO samples..... | 77 |
| 3. 8. XPS spectra of RF-sputtered NiFe-oxide samples sputtered at different oxygen flow rates covered with the Pt cap layer. Ni spectrum (left). Fe spectrum(right). Spectra are shifted in the y-direction to reveal the detail..... | 79 |
| 3. 9. XPS spectra of RF sputtered NiFe-Oxide samples sputtered at different oxygen flow rate covered with Au cap layer: Ni spectrum (left) and Fe spectrum (right). Spectra are shifted in the y-direction to reveal detail. | 80 |
| 3. 10. Rigaku X-Ray Diffractometer (XRD) at Texas State University. | 83 |
| 3. 11. Theta/2theta scan of the sample in the range 30-90 degrees at $\chi=0$ degree..... | 85 |
| 3. 12. Theta/2theta scan near highest intensity Silicon peak (69.17 degrees, left) and film peak (44.2, right). | 86 |
| 3. 13. Scan of Omega at the diffraction condition of silicon peak(left) and film peak(right)..... | 87 |
| 3. 14. Scan of phi at the diffraction condition of silicon(left) and film(right) in the range of -90 to 90 degrees. | 89 |
| 3. 15. Scans of chi at the diffraction condition of silicon peak (left) and film peak(right)..... | 90 |

| | |
|--|-----|
| 3. 16. Scan of theta/2theta of the sample at chi=0 degree (left) and chi=5 degrees (right). | 91 |
| 3. 17. Comparison of theta-2theta plot of Ni _{0.81} Fe _{0.19} (a) high-pressure thick samples (b) high-pressure thin samples (c) low-pressure thick samples. | 94 |
| 3. 18. Pole figure of Ni _{0.81} Fe _{0.19} with low gas pressure, thickness 100nm, at H=0, (a) with PSA 0.5 and (b) with PSA Open. | 97 |
| 3. 19. Pole figure of Ni _{0.81} Fe _{0.19} with high gas pressure measurement done by using PSA Open, (a) thickness 100 nm, at H=0, (b) thickness 50 nm, at H < >0 and (c) thickness 50 nm, at H=0. | 98 |
| 3. 20. Pole figure of Ni _{0.81} Fe _{0.19} sample (thickness 100nm) sputtered without rotating the sample holder during deposition and pole figure measurement done by using PSA 0.5 (left) and PSA Open (right)..... | 99 |
| 3. 21. Change in shape and orientation of irradiated footprint on the sample surface for tilt angle α and Bragg angle 2θ [73]. | 101 |
| 3. 22. Defocusing correction sample prepared by using superglue: showing nonuniform thickness..... | 102 |
| 3. 23. Defocusing correction sample prepared by using hair spray. | 103 |
| 3. 24. Defocusing correction sample prepared using double-sided tape..... | 104 |
| 4. 1. Comparison of hysteresis loops measured at different sweep rate with the hysteresis loops measured in step mode all measured with a lock-in amplifier time constant of 0.1 seconds. | 107 |

| | |
|--|-----|
| 4. 2. (a) Variation of coercivity with sweep rate (blue) and measurement time with sweep rate (red) in a semi-log graph (top); (b) variation of measurement time with sweep rate in a linear graph (bottom). | 109 |
| 4. 3. Comparison of hysteresis loops measured at different sweep rate with the hysteresis loops measured in step mode at time constant of 0.01 seconds. | 111 |
| 4. 4. Spread of measured saturation magnetic moment of an asymmetric 3.5" floppy sample with a trapezoid shape as a function of the field angle..... | 113 |
| 4. 5. Spread of measured saturation magnetic moment of a circular 3.5" floppy sample versus field angle..... | 114 |
| 4. 6. Variation of the measured magnetic moment as a function of field angle in the 3.5" floppy sample which is aligned at 180 degrees before the first measurement. | 115 |
| 4. 7. Angle-dependence of measured remanent magnetic moment of asymmetric sample aligned at each angle (a), of circular sample aligned at each angle (b) and of circular sample aligned at 180 degrees only (c)..... | 117 |
| 4. 8. Angular dependence of coercivity of circular 3.5 "floppy sample. | 119 |
| 4. 9. wobble circle ($r=1$) at position (1,0) (left) and at wobble circle ($r=1$) at position (1,1). | 129 |
| 4. 10. Normalize angular dependence of sensitivity: sample centered by positioning at average alignment position (left) and normalized symmetric angular | |

| | |
|---|-----|
| sensitivity ($S_{xx}'(\theta)/S_{xx}(0)=0.5(S_{xx}(\theta)/S_{xx}(0)+S_{xx}(\theta+\pi)/S_{xx}(0))$) calculated by averaging the normalized sensitivity at θ and $\theta+180$ degrees (right)..... | 130 |
| 4. 11. M_y hysteresis curve measured at 0, 180, and 360 degrees, and M_x hysteresis curve of circular 3.5” floppy sample at 0 degrees. | 132 |
| 4. 12. Normalized Sensitivity (top)and normalized cross talk (bottom) as a function of the position for the Mallinson’s coil configuration. Coil position in mm. | 137 |
| 4. 13. Dependence of normalized sensitivity (S_{xx}) on the sample position for the sample displacement in (a) x' -direction assuming perfect alignment for y' and z' (b) y' -direction assuming perfect alignment for x' and z' | 139 |
| 4. 14. Position dependence of normalized cross-talk on the sample position for the sample displacement in (a) x' -direction assuming perfect alignment for z' and $y'=-1$, (b) y' -direction assuming perfect alignment for z and $x'=-1$ | 141 |
| 4. 15. Angular dependence of normalized sensitivity with (a) wobble center at the origin, (b) wobble off-centered. | 142 |
| 4. 16. Angular dependence of normalized cross-talk with (a) wobble centered at the origin, (b) wobble off-centered. | 143 |
| 4. 17. (a) and (b) IRM and DCD measured between 0- 6000 Oe. (c) Hankel plot and (d) Delta m plot showing the negative magnetic coupling of floppy..... | 146 |
| 4. 18.(a) IRM, (b) DCD, (c) IRM and DCD measured 0-6000 Oe, (d) Hankel plot, (e) Delta M plot showing the negative magnetic coupling of $Ni_{0.81}Fe_{0.19}$ sample. | 150 |

| | |
|---|-----|
| 4. 19. calculation of the slope of magnetic moment versus time graph of circular 3.5” floppy disc sample as a function of the magnetic field..... | 153 |
| 4. 20. variation of the slope with applied magnetic fields in the opposite direction of initial magnetic moment. | 154 |
| 4. 21. Decay of magnetic moment in the presence of the constant magnetic fields of VHS tape..... | 155 |
| 4. 22. Variation of change of magnetic moment with the applied fields of VHS tape.. | 156 |
| 4. 23. Variation of X- signal slope with applied fields of o Ni _{0.81} Fe _{0.19} sample. | 157 |
| 4. 24. Variation of the Y-signal slope with an applied field of Ni _{0.81} Fe _{0.19} sample. | 158 |
| 4. 25. Comparison of variation of slope of M _x and M _y signals of Ni _{0.81} Fe _{0.19} samples measured at (a) 0 degrees, (b) 45 degrees and (c) 90 degrees. | 159 |
| 4. 26. Variation of coercivity of NiFe sample. | 160 |

LIST OF TABLES

| Table | Page |
|--|-------------|
| Table 1. materials parameters Pyrex and fused quartz. | 32 |
| Table 2. Measured and calculated parameters MicroSense sample rods. | 32 |
| Table 3. Measurement parameters for theta/2theta measurement to determine diffraction condition. | 85 |
| Table 4. Measurement parameters for omega scan. | 87 |
| Table 5. Measurement parameters for phi scan. | 88 |
| Table 6. Measurement parameters for Chi scan. | 90 |
| Table 7: Coercivity values at different sweep rate in sweep mode and step mode. | 107 |

LIST OF SYMBOLS

| Symbols | Description |
|----------------|---------------------------------------|
| m_s | Saturation magnetic moment. |
| m_r | Remanent magnetic moment. |
| H_c | Coercive field. |
| N | Demagnetizing factor |
| K | Aspect ratio. |
| K_d | First order shape anisotropy constant |
| L | Torque |
| K_u | Uniaxial anisotropy constant |
| K_{eff} | Effective anisotropy constant. |
| χ | Susceptibility. |
| S_{xx} | Sensitivity. |
| S_{xy} | Cross-talk. |
| \mathbf{m} | Dipole moment. |

ABSTRACT

This thesis describes the results on my thesis research. I investigated properties of Permalloy and Permalloy oxide thin films with Xray photoelectron spectroscopy (XPS), Xray diffractometry (XRD) and vibrating sample magnetometry (VSM). Focus was on properties that had not been investigated in detail by former graduate students from Dr. Geerts. The thesis also contains a literature study on the texture of Permalloy and Permalloy oxide RF sputtered films, and preliminary magnetic measurements performed on those samples and magnetic recording samples to learn more about the new MicroSense biaxial VSM.

The first chapter first introduces different types of magnetic materials followed by a literature review of Permalloy and Permalloy oxide focused on texture and magnetic properties related to this thesis research. The second chapter starts by introducing the reader to the working principle of the MicroSense vibrating sample magnetometer (VSM). This chapter includes a discussion of the measurement principle, noise sources and systematic errors associated with the VSM measurement method. The available measurement procedures of the VSM lie in the heart of this chapter. The third chapter talks about the AJA Sputtering System which was used to deposit the Permalloy and Permalloy oxide thin films. It includes details on the sputtering system and describes the process used to make the samples. It includes the results of the XPS and magnetic studies on Permalloy Oxide. The chapter also talks about the X-ray diffractometer (XRD) which was used to

determine the texture of the Permalloy films and includes the XRD measurement results. The fourth chapter mainly focuses on the magnetic case studies on floppy and VHS samples to better understand the MicroSense VSM and its measurement methods. In addition, this chapter also contains the preliminary results on floppy, VHS tape, and Permalloy samples. And finally, the fifth chapter summarizes the most important results of this research work; this chapter also contains details about suggested future works.

CHAPTER

1 INTRODUCTION

1.1 Motivation

Permalloy is an unordered ferromagnetic nickel-iron alloy with extremely high magnetic permeability, small coercive force, a small hysteresis loss, and small remanence. The material is interesting for applications because its magnetic properties can be modified by magnetic field annealing and the material has a very small magnetostriction, which means that magnetic properties of devices made with Permalloy are not easily changed by strain which is not easily controlled in thin films. It has become more and more important for modern nanotechnology and nano-electronics due to its particular magnetic properties. The first application of Permalloy was in telegraphic communication to maintain signal degradation caused by the distortion of communication cables. Due to its high permeability, Permalloy is also applied in sensing devices and actuators [1]. It is notable for its very high magnetic permeability, which makes it useful as a magnetic core material in electronic equipment, and in magnetic shielding to block magnetic fields. Due to its giant magnetoresistance, Permalloy is often applied in all kind of sensors [2][3][4]. In particularly, Permalloy ($\text{Ni}_{0.8}\text{Fe}_{0.2}$) is well known due to its wide use in the magnetic recording industry: it is attractive because of its high permeability, low coercivity, and small magnetic anisotropy. Since Permalloy has a vanishing magnetostriction it has been employed in many applications, such as anisotropic

magnetoresistance (AMR) and planar Hall effect (PHE) field sensors [5] [6], magnetic recording heads and magnetoresistive random access memory (MRAM).

NiO is an antiferromagnetic material. NiO thin films and its doped cousins have been extensively studied for a large variety of applications, including use as a biasing layer in spintronic devices, an electron blocker in solar cells, an electrode in novel batteries, a memory material in resistive nonvolatile Random-Access Memory, a catalyzer in chemical catalyzers and a gas sensing layer in gas sensors [7]. Its applicability originates from the ability to modify its properties by changing the ratio of O to metal atoms and to modify its crystallinity by doping with other transition metals. Fe alloying of NiO gives rise to NiFeO which is also considered as the oxide of Permalloy ($\text{Ni}_{0.8}\text{Fe}_{0.2}$). Because of the important applications of Permalloy, interest in the study of Permalloy Oxide ($\text{Ni}_{0.8}\text{Fe}_{0.2}\text{O}$) has also been greatly increased among the scientific community. Another way for obtaining Permalloy oxide is by Fe doping of NiO. Currently little is known on how Fe doping affects its properties. Recently, Permalloy Oxide has been shown to enhance strongly the performance of lateral spin valve devices [8][9][10]. Not a little bit but significantly, i.e. a factor 5-10, so possibly interesting for applications. In order to apply PyO in devices, though, it is necessary to know more about its properties. In particular, its optical, magnetic, and electrical properties need to be well understood.

1.2 Magnetic materials

To some extent all materials are magnetic. To classify them in different categories one often compares their magnetization, i.e their magnetic moment per unit volume ($M=m/V$) or their susceptibility, i.e. the slope dM/dH of the $M(H)$ curve.

The susceptibility of the sample can be easily calculated by using the following relation:

$$\chi = \frac{\bar{M}}{H} \quad (\text{emu/cm}^3 \text{ Oe}) \quad [11] \quad (1.1)$$

The total angular momentum and nature of electron's interactions in matters are responsible for the phenomenon of Magnetism. In terms of magnetic behavior, there are five classes of magnetic materials, i.e. diamagnetic, paramagnetic, ferromagnetic, antiferromagnetic and ferrimagnetic materials [11].

Diamagnetism originates from Faraday's induction law, is a fundamental property of matter and takes place in all substances, although it is usually very weak and often overshadowed by other magnetic properties. Diamagnetic substances are composed of atoms which have no net magnetic moment (i.e., all the orbital shells are filled and there are no unpaired electrons). Under the influence of an applied magnetic field, a diamagnetic material obtains a nonzero magnetic moment. The magnetic moment as a function of the applied magnetic field, $m(H)$ for a diamagnetic material is a linear curve that slowly decreases from zero; this means that a diamagnetic material has a negative susceptibility χ . The value of the susceptibility is independent on the temperature.

In Paramagnetic materials, some or all of the atoms or ions in the material have a net magnetic moment due to unpaired electrons in partially filled orbitals. However, the

individual atomic magnetic moments do not interact magnetically, and like diamagnetism, the average magnetization is zero when the field is removed. When an external magnetic field is applied, there is a partial alignment of atomic magnetic moments in the direction of the applied magnetic field. This means that the paramagnetic material carries a net magnetic moment in the presence of a magnetic field. The field dependence of the magnetic moment of a paramagnetic material ($m(H)$), at small magnetic fields is a linear graph; this means that its susceptibility χ is positive. At higher fields, the alignment of the magnetic moments saturates. The magnetic moment of a paramagnet is inversely proportional to the temperature, so the higher the temperature the less the magnetic moments are aligned.

The ferromagnetic materials often have a large non-zero magnetic moment at zero field because the magnetic dipole moments of neighboring atoms prefer to be aligned in the same direction. For ferromagnetic materials, spins on neighboring atoms are aligned due to exchange interaction. Therefore, the net magnetic moment of ferromagnetic material can be non-zero in zero magnetic field and depend on the field that was applied to the material in the past. In other words, ferromagnetic materials seem to remember their history of the magnetic field applied to the material and show hysteresis. The $m(H)$ curve for a ferromagnetic material is often non-linear and exhibits hysteresis. As ferromagnetic materials are heated, the thermal agitation randomizes the alignment of the atomic's magnetic moments and hence the saturation magnetization decreases. Eventually, the thermal agitation becomes so great that the material becomes paramagnetic; the temperature of this transition is the Curie temperature, T_C .

An antiferromagnetic material is a substance with a zero net magnetic moment because the moment of nearest neighbor's atoms are aligned antiparallel. This leads to the cancelation of the net magnetic moment on a macroscopic scale. So similar to ferromagnetic materials, antiferromagnetic materials are ordered at a lower temperature. Like ferromagnetic materials, these materials become paramagnetic above a transition temperature, known as the Neel temperature, T_N . One of the characteristics of antiferromagnetism is that they show a non-zero positive susceptibility above T_N . Above this temperature, the susceptibility obeys the Curie-Weiss law with a negative intercept indicating negative exchange interaction. Small grains of anti-ferromagnetic material tend to have a magnetic moment because of uncompensated spins near the surface of the antiferromagnetic material. The magnetic susceptibility of an antiferromagnet typically shows a maximum at the Neel temperature.

Ferrimagnetism is only observed in compounds, which have a more complex crystal structure than a pure metal. Similarly, to antiferromagnetic material, in ferrimagnets the magnetic dipole moment of neighboring atom planes are anti-parallel to each other. The ferrimagnets however have a non-zero net magnetic moment because the magnetic moments of neighboring atoms are not equal. The magnetic moments in this material are aligned antiparallel. The magnetic behavior of a ferrimagnetic material is also similar to that of ferromagnetic materials, although ferrimagnetic materials usually have a lower saturation magnetization.

The magnetic materials that show spin order in zero magnetic field, i.e. the ferromagnetic, ferrimagnetic, and antiferromagnetic substances, often only show order on a microscopic scale. Areas that are ordered are referred to as domains.

1.3 Literature review of the texture and magnetic properties of NiFe

P. Prieto et al. found that the nanocrystalline $\text{Ni}_{80}\text{Fe}_{20}$ thin films prepared by dual ion-beam sputtering and $\text{Ni}_{80}\text{Fe}_{20}$ thin films assisted during the deposition with different concentration of N_2^+ , the X-ray diffraction (XRD) pattern show the reflection corresponding to (111), (200) and (220) planes of face centered cubic (fcc) Permalloy phase. As the concentration of N_2^+ ion increased up to 50%, the XRD diffraction peaks start to broaden which is an indication of the nanocrystalline nature of the film [12]. They claimed that for N_2^+ concentration $\geq 75\%$, complete change of structure is noticed and the (111), (200), and (220) reflections of the fcc $\gamma\text{-Ni}_3\text{FeN}$ are observable in the corresponding XRD pattern. According to P. Prieto et al. the ion bombardment during growth induces preferential growth of (220) planes and (111) preferential orientations as compared to a non-assisted film [12]. From angular remanence measurement, they found that both non-assisted and N_2^+ assisted thin films show in-plane uniaxial anisotropy but the assisted film does not have as well-defined as the non-assisted film [12].

Zeeshan Ali found that Permalloy films deposited under an angle have a dependent uniaxial anisotropy. For the deposition angle < 70 degrees, the easy axis is in the plane but perpendicular to incident flux direction. As the deposition angle increase beyond 70 degrees, the easy axis reorients along the in-plane-parallel direction. Also, when the deposition angle is gradually increased, the coercivity and saturation field are increased, but saturation magnetization is reduced [13]. O.D. Roshchupkina et al. compared the texture of as-deposited Permalloy film, the film implanted with ion influence and film annealed at 800 degree Celsius. They found that all samples exhibit strong (111) texture

and weak (220) texture. Furthermore, extra textures develop with ion-implanted samples [14].

J.C.A. Huang et al. found that the single crystalline Permalloy films grown on MgO substrate are almost strain-relieved for the thickness above 250 Å. They also found that the film grown on MgO substrate exhibit small coercive field (H_c) as compared to the polycrystalline film grown on a silicon substrate. That might be caused by the reaction of Ni with silicon that forms a silicide (harder ferromagnet than Permalloy) in the silicon-Permalloy interface [15]. E. B. Park et al. found that the Permalloy film grown on SiO₂/Si substrate in the presence of a magnetic field, the strong uniaxial anisotropy develops along the applied field direction. This induced magnetic anisotropy is related to deposition-induced anisotropic stress. Also, the XRD results of the Permalloy film deposited without the magnetic field, (111) plane is the most preferred orientation in the direction parallel to the film surface and there is no preferred orientation in the perpendicular direction to the film surface [16].

Xiaoyu Li et al. found that Permalloy film grown on Silicon substrate with Cu underlayer, below the critical thickness, the direction of the in-plane easy axis is perpendicular to the deposition direction, while the hard axis is along the deposition direction. The hysteresis loops measurement along easy axis show high squareness with a residual magnetization ratio $M_r/M_s \sim 1$ while along the hard axis, they found quite linear curves with nearly zero-remanent magnetization. This indicates the existence of well-defined in-plane uniaxial magnetic anisotropy which can be generated by obliquely sputtered Cu underlayer. The origin of the in-plane uniaxial magnetic anisotropy might be attributed to the anisotropic topological interfacial roughness between Cu and

Permalloy layer. Also, they found that easy axis coercivity, hard axis coercivity and anisotropic field (H_k) decrease with increase in film thickness below the critical thickness [17].

Gaoxue Wang et al. found that Permalloy film deposited by radio frequency sputtering in an oblique incidence on Si substrate, there exists an in-plane anisotropy which was confirmed by the difference in hysteresis loop measured along the easy axis and hard axis. Also, for the film thicker than 140 nm, a rotatable stripe domain (an array of oscillating “up and down” magnetic domain, known as stripe domain or SD) was observed, which resulted in the reduction of remanence and enhancement of coercivity along the hard axis. SD formation is also indicated by linear magnetization rotation part and steep switching parts of small fields [18]. M. Goto et al. found that there are dead (which is formed at the initial stage of deposition) and induced anisotropy layers in $Ni_{80}Fe_{20}$ film evaporated in the magnetic field. In the study of magnetic anisotropy (K_u) and saturation magnetization (M_s) of Permalloy films of varying thickness, they found that K_u decreases with decreasing the thickness while M_s is independent with the film thickness [19].

R. Romera et al. investigated the effect of the layer thickness on the magnetic properties of Permalloy deposited by DC Magnetron sputtering on thermally oxidized Si substrate. They witnessed the change in anisotropy from in-plane anisotropy (for thinner samples) to an out of plane anisotropy (for thicker samples). Because of the columnar nature of sample growth, thicker the sample is, higher is the perpendicular anisotropy induced. Also, they found an increase in coercivity and saturating field as film thickness increases. At a certain thickness, magnetization has a component perpendicular to the surface of the

film, and the sign of this magnetization component alternates from one domain to another to reduce the magnetostatic energy. As a result, thicker layers require a much higher field to saturate the in-plane hysteresis loops [20].

M. Maicas et al. compared the magnetic properties of 150 nm thick Permalloy samples deposited on a glass substrate with perpendicular incidence using in-plane magnetic field and oblique incidence. They found that the saturating field for the first sample is 6 Oe and that of the second sample is 40 Oe. Furthermore, they compared the magnetic properties of Permalloy film by growing the samples with 2,4,8 and 16 layers with alternating perpendicular anisotropies with relative thickness $t:2t$ and the total thickness is 150 nm for each sample. They found that the saturating field decreases from about 15 Oe for the sample with 2 layers down to 4 Oe for the sample with 16 layers. This is because of the sample with many layers, the thickness of the smaller layer ($t=6\text{nm}$) is much smaller than the exchange-correlation length (180 nm), as a result, magnetization rotation between the layers is so small that it remains nearly parallel in the whole sample for every magnetic field. This causes the hysteresis loop to increase in linearity. This effect makes a difference in the saturating field. The coercivity field depends also on the number of layers and is found to be smaller for the thinner film [21].

According to F. Czerwinski et al., nanocrystalline $\text{Ni}_{80}\text{Fe}_{20}$ Permalloy samples obtained by electrodeposition exhibit the fiber texture with a major component of the (100) axis, aligned perpendicular to the specimen surface and weaker component along (111). They claimed that (111) texture becomes stronger than the strength of (100) after annealing but the strength of (111) texture after annealing is lower than (100) texture after deposition. Also, it is relatively difficult to produce the (111) texture, especially as a single and

strong component. It exists usually as a minor component in along with another texture [22]. C.S. Ha et al. found that nanocrystalline Ni-Fe alloy foils fabricated by electroforming method, exhibited strong (100) texture perpendicular to the surface normal and weak (111) fiber texture. They observed the transformation of texture from (100) to (111) after annealing [23].

Y. B. Park et al. found that nanocrystalline Fe-78% Ni alloy foil fabricated by using an electrodeposition method at a temperature of 45 degrees Celsius and a current density of 10 A/dm², the intensity of (111) peak is drastically increased and its full-width half maximum is decreased when sample is annealed at 400 degree Celsius. This indicates that grain growth takes place after annealing. From pole figure measurement, they found a strong (100) texture and weaker (111) fiber texture perpendicular to the specimen surface. They witnessed that the textural state is completely reversed after annealing. The (111) texture becomes predominant and (100) texture decreases to a low level.

Furthermore, when compared to the as-deposited sample, the XRD diffraction angle for the (111) peak decreases while for the diffraction angle for the (200) peak increases. This means that the interatomic spacing for (111) grains increases and for the (100) grains shrinks during annealing. This abnormal growth of (111) texture during annealing is related to the lower energy density of (111) plane compared to (100) plane. They claimed that because of the lower surface energy of (111) plane than to other planes if the electrodeposition is carried out under a condition close to equilibrium (111) texture is expected to be stronger [24].

H. Li et al. found that nanocrystalline Ni-20%Fe prepared by electrodeposition, the strong (111) texture. They claimed that texture depends on the deposition rate. At lower

deposition rate (111) texture becomes dominant but at higher deposition rate a site does not have sufficient time to reach the lowest energy state orientation, so (111) texture is weaker [25].

J.H. Seo et al. found the mixture of strong (100) and weak (111) fiber texture perpendicular to the specimen surface of the as-deposited Ni-20%Fe nanocrystalline deposited by the electroforming method. The textural state is completely reversed after annealing. After annealing the sample at 390 degree Celsius for 30 minutes, the development of the (111) texture becomes predominant while the intensity of (100) texture decreases to some extent. The energy of the (111) is smaller than (100) plane, so during annealing, the abnormal growth of the (111) grains (which are more coarser than (100) grains in fully annealed system) takes place to decrease the interfacial energy and hence total energy of the system [26].

D.N. Lee found strong (100) and weaker (111) fiber texture which changes to the texture characterized by major (111) and minor (100) after annealing of the nanocrystalline Ni-20% Fe samples prepared by electrodeposition. This is due to the fact that $\langle 111 \rangle / \langle 111 \rangle$ tilt boundary has the highest average mobility [27].

S.F. Cheng et al. studied the effect of sputtering pressure, sputtering power as well as Ta and Cr seed layer on the texture of the Permalloy thin film grown by DC magnetron sputtering. They found that at lower power (100W), the orientation is random. With reducing gas pressure, (111) intensity is gradually increased and a weak fiber texture is developed. They claimed that higher power (300W) in combination with low gas pressure is more effective in inducing the (111) texture. This is because of the larger atom's mobility at lower pressure and arrival of energetic atoms for the film sputtered at higher

power. Furthermore, they found that with the Ta seed layer, the intensity of (111) texture is increased by two orders of magnitude compared to without Ta as the seed layer. Ta has a tetragonal structure with a strong (002) texture that promotes the epitaxial growth of Permalloy that results in strong (111) texture. On the other hand, Cr has BCC structure with weak (110) texture that does not promote epitaxial growth of Permalloy, so Cr seed layer does very little (111) enhancement. However, Ta seed layer has almost no effect in magnetic properties but the Cr seed layer is very effective in reducing saturation field and Coercivity of the film [28].

Movaffaq Kateb et al. found that Permalloy films of varying thickness, prepared by tilt deposition with and assisting in situ magnetic exhibited strong (111) texture perpendicular to the substrate without any tilt texture. The intensity of the (111) texture increases with increase in film thickness. Furthermore, they claimed that the rotation of the sample during growth encourages texture normal to the substrate, rather than a tilted texture. Also, they found a well-defined uniaxial anisotropy that is square easy axis with sharp switching and linear hard axis without hysteresis [29].

1.4 Literature review of the texture and magnetic properties of NiFeO

Yuan-Hua Lin et al. found that the Fe-doped NiO samples exhibit obvious ferromagnetic properties at room temperature and the magnetization loops exhibit a remanent magnetization and characteristic ferromagnetic hysteresis cycle. This magnetism in the Fe-doped NiO could be caused by the double exchange through the introduced magnetic Fe ions and the related defects [30]. Douvalis AP et al. found that 2% Fe-doped NiO

samples, prepared $\text{Ni}_{0.98}\text{Fe}_{0.02}\text{O}$ by chemical method and heated this precursor in air at temperatures between 673 and 873 K, are ferromagnetic and this magnetism is related to NiFe_2O_4 ferrimagnetic impurities, but this phase may not be detected by the XRD due to its small particle size effect or high dilution [31].

Twagirayezu et al. found that radio frequency sputtered $\text{Ni}_{0.8}\text{Fe}_{0.2}\text{O}_{1-\delta}$ have the NaCl-structure and have a strong (111) texture. This was confirmed by XRD results. From the magnetic measurements, they found high field magnetic slope in all Fe-doped NiO samples. They claimed that field hysteresis and high magnetic slope depend on temperature. Furthermore, for low oxygen flow sputtered samples, the high field slope increases with increasing temperature and for a high oxygen flow sputtered sample, the high field slope decreases with increasing temperature [32].

Ashish Gandhi et al. found that for Fe doped NiO samples at varying Fe concentration, prepared by the hydrothermal method, the intensity of X-ray diffraction peaks decreases with the increase of Fe concentration indicating that Fe-doping has led to an increase of disorders, which could be possibly originated due to defects such as substitutional Fe^{3+} at the Ni site [33].

K.O. Moura et al. found that Fe-doped NiO nanoparticles, prepared by Co-preparation method, the particle macro strain increases with the Fe insertion and decreases the particle size. These modifications can be associated with a small difference between the ionic radii of Ni^{2+} (0.69 Å) and Fe^{3+} (0.64 Å). The magnetization result measured under zero-field cooled curve (ZFC) displays a broad blocking temperature with a maximum of around 145 K for Fe-doped NiO and 155 K for NiO. This is likely to be caused by a

change in particle size due to the insertion of Fe in NiO. This fact is also associated with a decrease in the lattice parameter as a function of iron insertion [34].

P.M. Ponnusamy et al. found that the XRD diffraction peaks of Fe-doped NiO nanoparticle samples shift toward higher 2θ values compared to undoped NiO. This shift may be due to the occupation of Fe^{3+} ions at the Ni^{2+} sites. The doping of Fe ions into NiO creates internal macrostrain and microstructural disorder into NiO lattice which affects the grain growth and broadens the Bragg diffraction peaks. The NiO nanoparticles display a weak ferromagnetic phase because of the presence of a small hysteresis and it is increased when Fe is doped into NiO. The doping effect reduces the particle size and enhances the net magnetization [35].

S. Manna et al. found that pure NiO nanorods at room temperature exhibit a weak ferromagnetic phase due to the presence of a small hysteresis at low magnetic field, and a presence of antiferromagnetic phase [36]. The Fe doping increases the hysteresis compared to undoped NiO. Fe ions have two stable valence states Fe^{3+} and Fe^{2+} and the ferromagnetism may arise from Fe^{3+} , or a mixture of Fe^{2+} , and Fe^{3+} states [29]. The XRD results show six characteristic peaks of cubic crystalline NiO, i.e. (111), (200), (220), (311), (222), and (400). The same peaks appear for Fe-doped NiO which indicates that there is no presence of an impurity phase when substituting Ni with Fe at some of the Ni sites [29].

Shaohui Liu et al. found that the XRD pattern of $\text{Ni}_{1-x}\text{Fe}_x\text{O}$ ($x=0, 0.01, 0.02, 0.05$) nanofibers samples exhibit five diffraction patterns characteristic of the rocksalt crystal structure. The lattice constant does not change due to the increase of the Fe doping because the radii of Ni^{2+} , Fe^{2+} , and Fe^{3+} are very close [30]. Both NiO and Fe-doped NiO

show hysteresis. The magnetic moment $m(H)$ of NiO is almost linear, characteristic of an antiferromagnet, but the magnetization of $Ni_xFe_{1-x}O$ samples does not saturate until 3 Tesla which indicates the coexistence of ferromagnetic and antiferromagnetic phases. The XPS study of $Ni_{0.98}Fe_{0.02}O$ nanofibers exhibit Fe 2p_{3/2} and Fe 2p_{1/2} peaks which means that $Ni_{0.98}Fe_{0.02}O$ exists as Fe^{2+} , and no metallic Fe was observed. This indicates that the origin of ferromagnetism is governed by the ferromagnetic secondary phase [37].

According to J.F. Wang et al. the XRD pattern of $Ni_{1-x}Fe_xO$ sample with $x \leq 0.02$ exhibit single-phase i.e NiO fcc phase. As $x=0.05$, a trace of Fe_2O_3 appears in the XRD pattern of the sample. As the x increases further, the sample becomes a mixture phase of NiO, Fe_2O_3 and $NiFe_2O_4$ ferrite. As dopant Fe increases, the crystal size of the sample decreases. This is likely to be caused by a disturbance of Fe on the NiO crystal which obstructs the crystal growth. The magnetic moment of their $Ni_{0.98}Fe_{0.02}O$ samples is independent of the temperature in the temperature range from 78K to 300K This result suggests that the Curie temperature is above room temperature. They found large shifts of the hysteresis loop for lower temperature. The shift of the hysteresis loop at low temperature could be associated with a ferromagnetic cluster and ferromagnetic/antiferromagnetic coupling due to compositional inhomogeneities [38].

Jinda Khemprasit et al. found that $Fe_{0.01}Ni_{0.99}O$ nanoparticles samples prepared by diol-based sol-gel process have a cubic rock-salt structure, and their crystal structure does not change even calcining at a different temperature ranging from 400 to 1000 degree Celsius. They believe that the origin of the ferromagnetism in their Fe-doped NiO results from (a) the double exchange interaction through Fe ions and defects (e.g. Fe^*Ni) and (b) the presence of ferromagnetic and/or ferrimagnetic impurities co-existing within the main

phase. They claim that due to grain growth during the heat treatment, the particle size and crystal size increases when the calcining temperature is increased. Furthermore, they found that when the calcining temperature increases, the XRD peak intensities increase. This is related to more crystallization of $\text{Fe}_{0.01}\text{Ne}_{0.99}\text{O}$ [39].

2 VIBRATING SAMPLE MAGNETOMETERS

2.1 Working principle of Vibrating Sample Magnetometer (VSM)

The Vibrating sample magnetometer (VSM) was invented by Simon Foner in 1955 at MIT Lincoln Laboratory, so it is also referred to as a Foner magnetometer. Although the instrument has been improved a lot since the first publications, its basic principle remains the same.

The vibrating sample magnetometer (VSM) is a machine that measures the $m(H)$ relation of a magnetic sample. This relation is often referred to as the fingerprint of the magnetic material. The operation of the VSM is based on Faraday's law of induction, which tells us that a changing magnetic field will produce an electric field. This electric field can be measured with a voltmeter and can tell us information about the sample's magnetic moment. The VSM typically measures the voltage induced in stationary pickup coils, also known as detection coils, due to the harmonic vibration of the sample as a function of a uniform applied magnetic field [40].

In the VSM, a sample is connected through a rod (sample holder) to a vibration source. The sample is placed in the middle of a set of detection (pickup) coils. As the sample vibrates, the coupled flux through the pickup coils changes with time. Due to this flux change, a voltage is induced across the terminals of these pickup coils. This voltage is proportional to:

- a. The magnetic moment of the sample

- b. The vibration speed of the sample
- c. The shape and size of the coils, including the number of windings
- d. The number of the detection coils and their position
- e. The average position of the sample with respect to the pick-up coils
- f. The shape and size of the sample

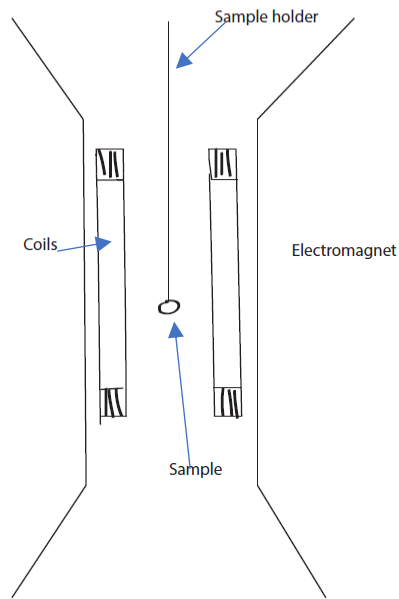


Figure 2.1. Illustration of the position of the sample between the coils of electromagnets in VSM. As the sample moves up and down, a flux change in the detection coils will be created.

For magnetic measurements, one is generally interested in the magnetic moment of the sample as a function of field, i.e. $m(H)$ or the magnetic moment as a function of temperature, i.e. $m(T)$ [41]. A large electromagnet that surrounds the sample and pickup coils is used to apply a magnetic field to the sample. As a result, the magnetization can be

measured as a function of the applied field. The VSM's operating software can be set up to measure different magnetic parameters in order to characterize a wide variety of magnetic samples of both high and low coercivity.

Many tricks have been applied to enhance the sensitivity of VSM, such as the use of lock-in amplifiers. Besides the electrical noise that is always present in VSM, it is generally sensitive to fluctuations of the field of the electromagnet, vibrations of the pickup coils and instability in sample vibration speed.

Most of those noise signals can be limited by a good design of the VSM including (1) securing of the wires of the pickup coils to the yoke of the magnet so they can-not move during the measurement; (2) encapsulating the coils in a fixture and securing them to the pole pieces of the electromagnet so they will not move during the measurement; (3) using various forms of active and passive vibration isolation to confine the vibration to the sample-rod; (4) use of multiple coils symmetrically placed around the sample, so that coupled flux fluctuations caused by sources other than the sample and sample-rod cancel out. If all those tricks are implemented correctly, the main noise source left is the Johnson noise of the wire used for the pickup coils. The signal-to-noise ratio of the VSM is limited by the ratio of the induced voltage to the (Johnson) Noise voltage. Among other things the former depends on the distance between the sample and the pick-up coils: the design of the detection coils is a tradeoff between absolute sensitivity (SNR) and the sensitivity of the instrument for small variations of sample size and sample position. Placing the coils very close to the sample can increase the sensitivity, but the measured signal becomes a strong function of the position of the sample.

2.2 Errors in VSM Measurements

The change in flux due to the vibration of the sample is measured by pickup coils.

However, not all of the measured signal is caused by the magnetic material under investigation. A variety of other things can contribute to the measured signal.

Furthermore, some of the unwanted signals distort the measured data. Data manipulation is carried out to remove the distortion and unwanted addition to the measured signal.

Depending on the types of measurement, several data manipulation functions can be applied.

The most important corrections for systematic errors in the measurement results are as follows:

2.2.1 Background Subtraction

The signal measured by VSM is the combination of the sample signal, signal of sample substrate, the signal of the sample holder and also the background signal produced by VSM itself. The largest systematic error originates from the magnetic properties of the sample holder. The transverse holders have a typical magnetic moment of 0.03 to 0.06 $\mu\text{emu/Oe}$. Two methods exist to subtract this background:

(a) One measures the empty sample rod and the sample with the sample rod under similar conditions and subtract both curves on a point by point basis; (b) If one assumes that the $m(H)$ curve of the sample rod is linear, one can determine the $m(H)$ curve from the slope of the hysteresis curve at high field. Note that such an approach is faster and for most

cases more accurate as only one measurement is required and both sample rod and sample are measured under exactly the same conditions. The background subtraction is carried out to separate the sample signal from all these other signals. In some cases, the signal from the sample substrate needs to be subtracted.

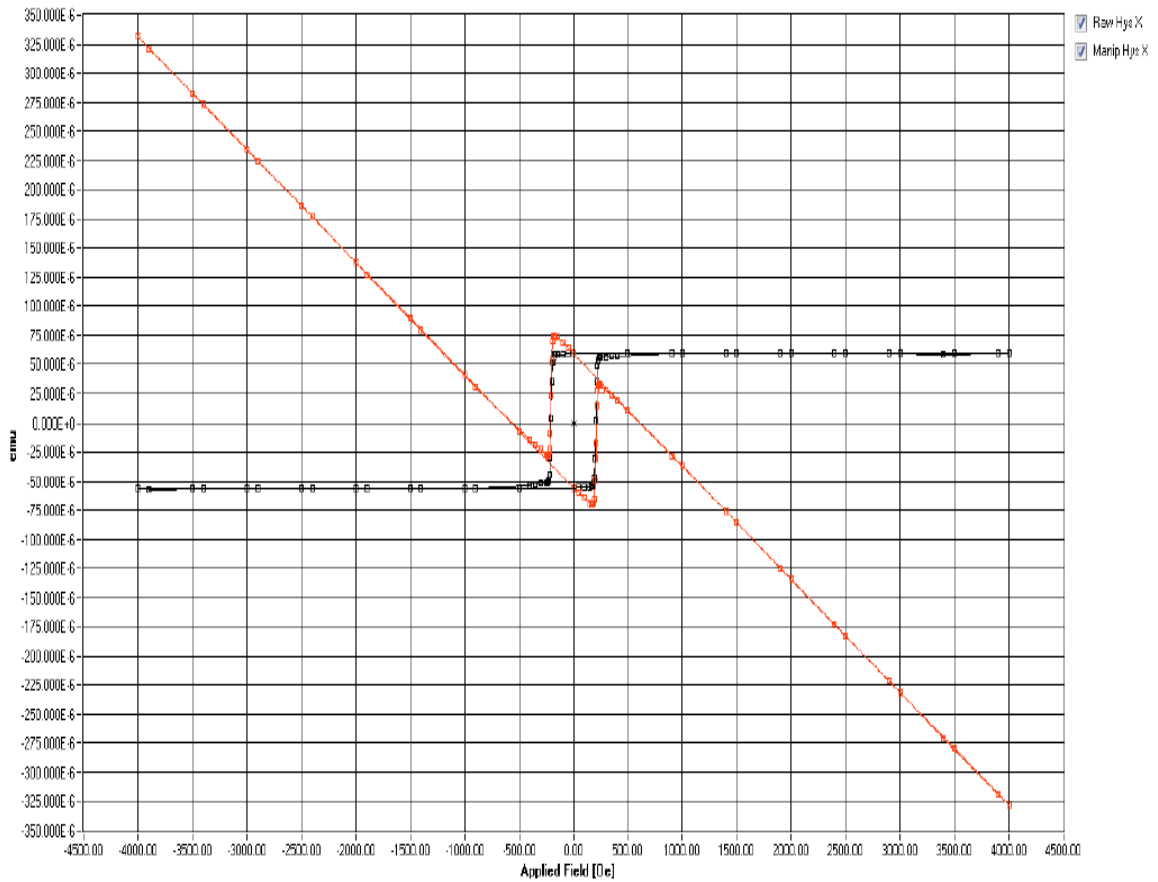


Figure 2. 2. Signals before background subtraction(red) and after subtraction (black) [35].

In most cases, diamagnetic background signals produced by sample holder (Pyrex or quartz), VSM system and silicon or glass substrate will have a straight line through the

origin with a negative slope. In all these cases, the background signal correction can be done by simply subtracting a straight line as a function of the field. In some cases, the straight line may have a small offset, the correction, in this case, will be:

$$M_{\text{corrected}(x,y)}(H) = M_{\text{measured}(x,y)}(H) - \text{offset} - \text{slope} \times H \quad (2.1)$$

In some cases, if the sample holder is not rotation symmetric, the slope of the background signal varies with angle. For this case, the correction will be:

$$M_{\text{corrected}(x,y)}(H) = M_{\text{measured}(x,y)}(H) - \text{offset} - \text{slope}(\text{angle}) \times H \quad (2.2)$$

When the sample substrate has a thin ferromagnetic thin coating, in this case, the background signal is not linear. In such a case, point by point background subtraction should be carried out. However, in the point by point subtraction, no data smoothing for the background signal is done so any noise in the stored background signal will show up in the corrected signal as well. Therefore, to suppress the noise in the background signal, it is advised to measure this background signal with sufficient averaging [41].

$$M_{\text{corrected}(x,y)}(H) = M_{\text{measured}(x,y)}(H) - \text{BGsignal}(H) \quad (2.3)$$

2.2.2 Image effect

When the magnetic material is placed near a highly permeable medium such as the pole pieces of the electromagnet, the magnetic charges on the sample will induce similar charges on the surface of that highly permeable medium. This effect is called the image

effect. In the VSM, when the sample is placed between the poles of an electromagnet, due to charges on the sample, images charges will be induced on the pole pieces of the electromagnet. The charges on the poles of the electromagnet can be described as an image sample. As the real sample is vibrating also its images are vibrating. Therefore, the pickup coils will also pick up the flux produced by the vibrating images. Thus, pickup coils for the magnetic moment parallel to the field receive extra signal for free.

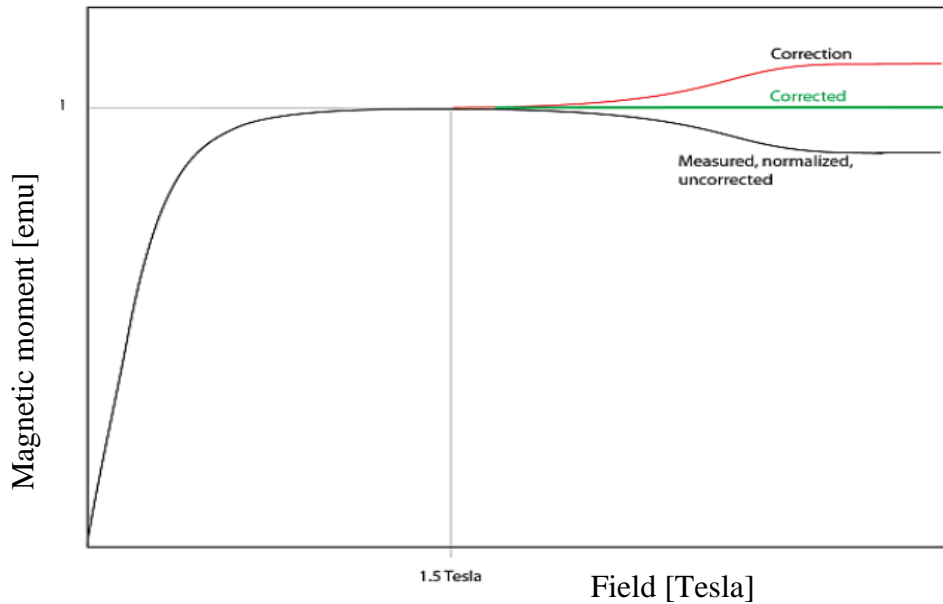


Figure 2. 3. Effect of image correction [41].

However, the poles of the electromagnet begin to saturate at fields above 1.5 Tesla. As a result, the magnetic permeability of the poles starts to decrease, and the strength of the image sample reduces. Note that the image sample disappears completely when the poles of the electromagnet are fully saturated. Once the poles of the electromagnet are

completely saturated, the pickup coils only see the flux changes of the actual sample and the sensitivity of the x-coils is reduced. The image effect correction compensates for this loss of magnetic signal as a function of the field [41],[40]. During the calibration of the setup, the sensitivity of a calibration sample is measured as a function of the field and stored in the calibration file.

For fields lower than the lowest field for which correction data is available (typically 15000 Oe):

$$M_{\text{correct}} = M_{\text{measured}} \quad (2.4)$$

For fields higher than the lowest field for which correction data is available (typically 15000 Oe):

$$M_{\text{correct}}(H) = M_{\text{measured}}(H)(1 + \text{image correction factor}(\text{correction}(H) - 1)) \quad (2.5)$$

2.2.3 Sample position

Sample position is another systematic error that occurs during VSM measurement. For optimal performance, the sample should be positioned in the center of the pickup coils. If the sample is very close to any one of the coils, the measured signal becomes a strong function of the position of the sample because the sensitivity of the pickup coil varies with the position of the sample. To limit the sample position effects, the sample position should be centered in between the pickup coils prior to starting the measurements. One should also center the sample position prior to starting the calibration process.

Horizontal centering i.e X-position adjustments can be performed by moving the sample left-right. If the sample is centered exactly at the center, the X-signal produced by the sample will reach a minimum in a saddle curve. Y-position adjustments can be done by moving the sample back and forth. The X-signal produced by the sample will reach a maximum when it is in the exact middle of the pick-up coil unit. Similarly, for the Z-position, the sample is moved up and down until the X-signal produced by the sample will reach a maximum in a saddle curve. Because of the design of the coils, the middle area of the saddle curve in the up-down (Z) direction is quite large and with some sample sizes, this saddle curve may show a small local minimum in the exact center of the coils. For a transverse sample-holder the adjustment of the z-position only has to be performed one time. For the perpendicular sample-holder it is recommended to adjust the z-position each time a new sample is loaded as the exact sample position on the perpendicular sample-holder determine the optimum z-height.

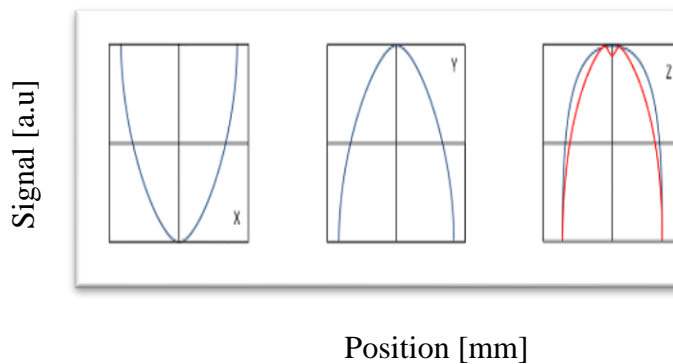


Figure 2. 4. X-Signal as a function of X-position (left) Y-position (center) and z-position (right) [35].

2.2.4 Remove Sweep Field Lag

In sweep-mode measurements are taken while the field is ramped up or down. In order to allow for high ramp-rates and high sampling rates, the lock-in amplifier signals are read through an AD-convertor that is connected to the analog output ports of the lock-in amplifiers. So, the data measured by the lock-in amplifier always lags the actual signal. For large field rates, this lag can be up to a few times the time-constant of the lock-in amplifiers. The software allows correcting for this delay. The remove sweep field lag function corrects for this issue and shifts the measured curve back over the calculated lag field. The software automatically determines the sweep lag based on the sweep rate used during the measurement. Note that this correction is not perfect and that significant errors in the hysteresis curves should be expected when ramping above 500 Oe/sec. The sweep mode will also add an offset to the measured magnetic signals which is caused by the offset of the DAQ card. This offset can be subtracted with the remove signal offset correction.

Most reliable hysteresis measurements are performed in step field mode. For this mode, the time constant of the field control circuit is reduced by the software just before the field is changed and then increased again after the field step is made. After this fast field change, the software waits a couple of time lock-in time constants so also the measurement moment signal has caught up. So, there is enough time between changing the field and measuring the actual signal.

2.2.5 Angular sensitivity

The sensitivity of the X-coils and Y-coils is angle-dependent, so there is a change in sensitivity of the system when the sample is rotated. This is especially true for the perpendicular sample-holder but even for the transverse sample holders, X-coil and Y-coil sensitivity depends on the angle. Such angle dependence is caused by centering errors when mounting the sample on the quartz sample rod and by the asymmetry of the sample. In addition, the exact sample position changes when changing the field angle causing a small contribution to the angular sensitivity.

The angular sensitivity correction function corrects for the change in sensitivity of the system due to the rotation of the sample. It is based on measurements one does during calibration. For the transverse holders, the angular correction only works if the calibration sample has exactly the same shape as the sample to be measured and sample and calibration sample are placed at exactly the same position of the quartz sample rod.

Normally, angular sensitivity correction is applied during data analysis. One can load the required correction values by pressing the Load Angular Sensitivity Curve from the calibration file button[41].

2.2.6 Remove Signal Offset

As the sample rod is rotated the actual position of the sample changes with respect to the pickup coils causing an offset in the hysteresis curves. Also, the DAQ card that is used to

read out the lock-in amplifier in the sweep mode adds an additional offset to the measured magnetic moment in the sweep mode. Based on the assumption that saturation moment should be identical for the positive and negative field, the software automatically calculates the signal offset. Using this correction, saturation magnetization at the positive side and negative side become identical. Note this correction only works for measurements like hysteresis loops in which signals at the maximum positive and negative fields should have identical values [41].

2.2.7 Remove Signal Drift:

Sometimes, if the measurement is started before stabilizing or warming up the system of the vibrator, the hysteresis loop may show some opening between the first few points and last few points. In such a case, one can use the remove signal drift function. This function replaces these bad data points with other data points. One can specify how many data points are replaced. Note, this function is only applicable for hysteresis loops. This can be done by specifying the number of data points that are replaced on remove signal drift menu under data manipulation in the software. This function is very useful for longitudinal MOKE measurements where a much larger drift is observed than for typical VSM measurements.

2.2.8 Field Reading Correction

The gauss probe in the VSM is normally mounted on the surface of the pole pieces of the electromagnet. This is done for convenience so that one doesn't accidentally touch the gauss probe with the vibrating sample and the oven/cryostat can freely slide around the sample. The disadvantage of having the gauss probe in a different location than the sample is that the field values measured at the magnet pole and sample location might not be the same. This difference is significant at the higher field values above 10,000 Oe and even worse as the magnet gap gets larger. Therefore, this function is used to correct this nonlinearity in the measurement of the magnetic field [41].

2.2.9 Sensitivity Correction

During the calibration process, if someone forgot to calibrate emu/V sensitivity or calibrated it with the wrong shape or size sample, the sensitivity correction function is used to correct the moment readings.

For instance, you did a measurement where the system used 65 as the emu/V sensitivity. Later you find out that for the sample size or sample orientation you used, the sensitivity should have been 55. The Sensitivity Correction factor allows you to correct for this by entering $55/65 = 0.8462$ as the sensitivity correction factor. This will change the scaling of the graph and all the moment related calculated parameters.

2.2.10 Resonance of sample rod system

The sample rod can be considered to be a one-side constrained beam which acts similar to a blade spring. So, sample holder and sample form a mass-spring system and will have a resonance frequency. It is important to understand how the resonance frequency depends on sample mass and sample rod properties and dimensions. The vibration frequency of the VSM should be chosen far enough away from the resonance frequency of the rod-sample system in order to avoid large transverse vibration amplitudes which result in broken sample holders. Therefore, in this section resonance of the sample-sample rod system is discussed.

2.2.10.1 Free vibration

It takes place when the externally applied forces are absent. The system oscillates under the action of forces inherent in the system itself due to initial disturbance. The system under free vibration will vibrate at one or more of its natural frequencies, which are properties of the dynamical system. In free vibration, the total energy of the system remains the same. It means that the amplitude of the vibration stays the same. This is a theoretical idea because in real systems the energy is dissipated to the surroundings over time and the amplitude decays away to zero. This dissipation of energy is called damping. Damping has very little effect on the natural frequency of the system, and hence, the calculations for natural frequencies are generally made on the basis of no damping. Damping is of great importance in limiting the amplitude of oscillation at resonance.

2.2.10.2 Forced vibration

It occurs when the object is forced to vibrate at a particular frequency by a periodic input of force. If an object is being forced to vibrate at its natural frequency, resonance will occur, and you will observe large amplitude vibrations. The frequency with the object vibrates is called the resonance frequency.

In the VSM, the vibration exciter is set to a particular frequency so that the vibration of the sample holder does not hit resonance. Before, setting the frequency in the system, one has to know the resonance frequency of the sample holder. The following procedure can be applied to find the resonance frequency:

The theoretical resonance frequency of the sample holder can be estimated from the following relation [42]:

$$w_1 = 1.875^2 \sqrt{\frac{k}{m}} = 1.875^2 \sqrt{\frac{K}{\rho AL}} \quad (2.6)$$

Where m is the mass, ρ is the density of the material of the sample holder, A is the areas of sample holder disc and K is stiffness of the sample holder which is given by:

$$K = \sqrt{\frac{3EI}{L^3}} \quad (2.7)$$

Where, E elasticity of the material of sample holder, L is the length of the sample holder outside the vibration exciter to a disc of the holder and I is the moment of inertia of the sample holder. For a hollow tube with diameter t and length L the moment of inertia is given by [43]:

$$I = 0.0491 * (L^4 - (L - t)^4)$$

Using the parameters of Pyrex and quartz we find for the resonance frequency of the tube 21.5 and 15.1 Hz. The difference for both materials is caused by the density difference and the rigidity modulus difference between both materials. See table below.

Table 1. materials parameters Pyrex and fused quartz.

| | Pyrex | fused quartz |
|------------------------------------|--------|--------------|
| Elasticity (E) (N/m ²) | 6.4E10 | 3.1E10 |
| Density (kg/m ³) | 2230 | 2203 |

Note that these frequencies are without loading the rod. We can correct the estimated natural frequency for the mass of the sample table and the mass of the sample with the procedure outlined in [42]. Then

$$w_1 = \sqrt{\frac{3EI}{L^3M}}$$

Where M is given by:

$$M = m_{\text{sample}} + m_{\text{table}} + 33/140 * m_{\text{tube}}$$

The parameters for our sample rods are provided in the table below.

Table 2. Measured and calculated parameters MicroSense sample rods.

| | m _{tube} calculated (gram) | m _{table} (gram) | m _{cal} 8 mm cal std. (gram) | m _{tube} +m _{table} (gram) |
|--|--|---------------------------|--|---|
| | | | | |

| | | | | |
|-------------|-------------|--------------|---------------|--------|
| 8 mm quartz | 2.200 | 0.190* | 0.112* | 2.135* |
| 8 mm Pyrex | 2.230 | | 0.112* | |
| 5 mm quartz | 2.2 | 0.074 | 0.112* | 3.6* |
| 5 mm Pyrex | 2.23 | | 0.112* | 2.545* |

* measured values, all other values are or estimated from density and volume indicated in the previous table.

The values in bold were used to estimate the natural frequency of the loaded sample holder. The natural frequency for the loaded holders are 21.8 and 13.1 Hz, so the loading of the sample-rod with the sample does not put the first harmonic close to the frequency of the vibrator head.

The 2nd transverse harmonic of an unloaded tube that is constrained on one side is given by [42]:

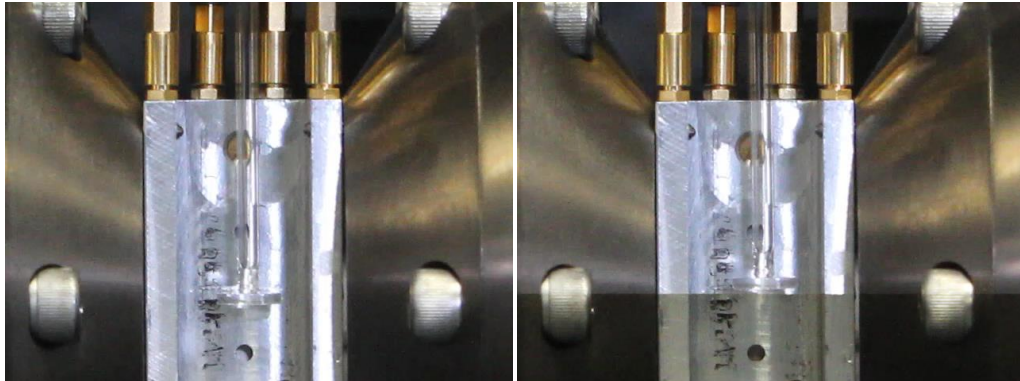
$$w_2 = 4.694^2 \sqrt{\frac{EI}{mL^4}}$$

Using the materials parameters of table 1 we estimate the resonance frequency assuming $m_{\text{tube}}=2.230$ gram, $m_{\text{sample}}=0.112$ gram, and m and $m_{\text{table}}=0.074$ gram and find 135 Hz for a Pyrex and 94.5 Hz for a quartz transverse sample holder. Assuming that the effect of the loading is similar for the 2nd harmonic as for the 1st harmonic, we find the estimated resonance-frequencies are 118 Hz and 82.2 Hz. Note that we expect quite a bit of error on this estimate for two reasons. Strictly speaking one can-not apply the same correction for the 2nd harmonics as for the 1st harmonics to estimate the effect of loading the rod. To correctly estimate the effect of loading on the 2nd harmonics one would need to use the

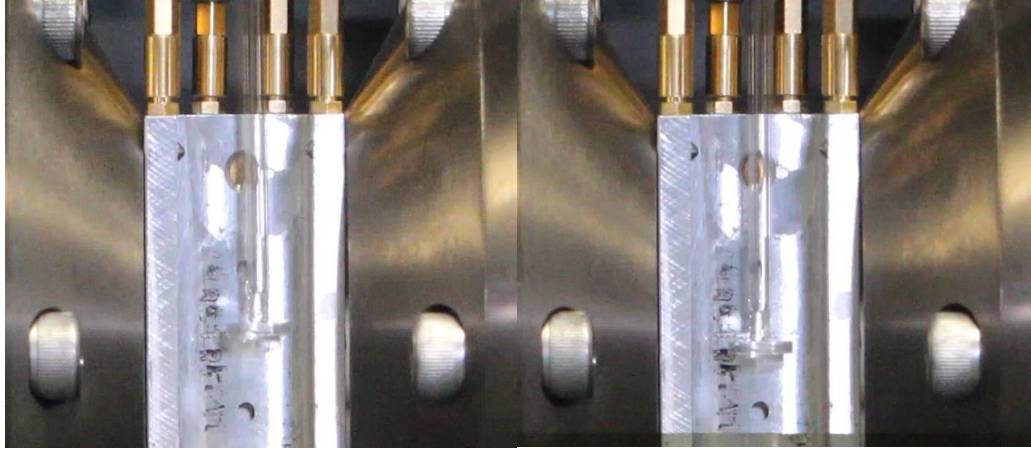
finite element method. Second, the measured mass values displayed in the last column of table 2 suggest that the wall thickness is not constant over different sample rods, so different 8 mm transverse quartz sample rods might have a slightly different resonance frequency.

Once the resonance frequency is calculated using the equations above, the set frequency in the system should be slightly higher or lower than the calculated resonance frequency to avoid large uncontrolled vibrations and risk breaking the sample rod similar to an opera singer breaking a wine glass. For example, if the calculated frequency is 80 Hz, the set frequency should be either 85 Hz or 75 Hz to avoid breaking the quartz sample rod. A more practical method to determine the correct set frequency of the lock-in amplifier is visually observing the vibration of the sample holder using a strobe light and camera. By changing the scope frequency, we can slow down the perceptive motion of the sample and see whether the sample just moves up and down or if it also moves slightly sideways. In our experiment, we fixed the position of the camera on a stand and used the camera zoom to capture the vibrations. A strobe flashlight was used to slow down the motion of the vibrating sample in the captured movie. This process was repeated for different sample vibration frequencies in the range of 75Hz to 85Hz. The vibration frequency of the VSM is set on Lock-in amplifier 1. The movies captured with the camera for each vibration frequency were analyzed with the Adobe program to estimate the transverse vibration amplitude of the sample. Images of the anti-node positions are displayed in Fig. 2.5 for the unloaded 8 mm sample holder at 80 and 85 Hz. A large horizontal vibration is observed at 85 Hz. For the transverse rods loaded with the calibration sample, the maximum horizontal vibration of the sample rod was observed near the set frequency of

80 Hz. At this frequency, the vibration of the sample holder table was not vertical but contained a large horizontal vibration component. Near resonance, the sample moves along an elliptical trajectory with the long axis oriented horizontally. Changing the field angle can cause the resonating sample rod to hit the aluminum casing of the biaxial pick-up coil set resulting in a broken sample rod. Over the course of a semester, half a dozen sample rods were destroyed before the problem was correctly identified. The vibration frequency was changed to 75 Hz which is far enough away from the resonance frequency of sample-sample rod system for a typical thin-film sample ($5 \times 5 \text{ mm}^2$ thin film on 0.5 mm thick silicon) as well as for the available calibration standards (Ni sheet metal). Since the vibration frequency was lowered to 75 Hz, not a single sample holder has been destroyed.



(a)



(b)

Figure 2. 5. Unloaded 8mm transverse holder (a) 80 Hz: slightly from bottom left to top right (b) 85 Hz: from bottom left to top right, more than 80 Hz.

2.3 Different parts of VSM

The VSM consists of the following parts:

2.3.1 Water-cooled electromagnet

Water cooled electromagnet along with power supply generates the constant magnetic field used to magnetize the sample. 50 mm Pole pieces are attached to the electromagnet. The pole pieces are structure composed of a material with high permeability that serves to direct the magnetic field produced by the magnet. Pole pieces simply extend the magnetic

core and can be regarded as a part of the electromagnet, particularly if they are made of the same materials.

2.3.2 Vibration head and sample holder (with angle indicator)

The sample holder rod is attached to the vibration head, and the end of it hangs down in between the pole pieces. It moves the sample up and down at a set frequency, typically 75Hz to avoid the breaking of sample holder due to the resonance issue described in the previous section. The sample rod can be rotated to achieve the desired orientation of the sample with respect to the external applied magnetic field. There are also three knobs for controlling the x, y, and z positions of the sample. These knobs are used to adjust the sample position prior to the measurement so it is perfectly centered in between the pick-up coils.

2.3.3 Pickup coils

The sample produces an alternating current in these coils at the same frequency as the vibration of the sample. The signal generated contains information about the magnetization of the sample.

2.3.4 Lock-in amplifier

This amplifier is tuned to pick up only signals at the vibrating frequency. This eliminates noise from the environment, such as from the overhead lights or hovering spacecraft nearby (unless the noise happens to be at exactly 75Hz and is phase-locked with the vibrator).

2.3.5 Computer interface

The software makes data collection easier by automating the control of the various components during data collection. The data can be graphed on the computer screen, printed, or written to file (pdf file, text file, or MS Excel file).

2.4 Options available in MicroSense Easy VSM

2.4.1 The VSM Option

The Microsense VSM at Texas State University has a conventional electromagnet which has a maximum field of 2.54 Tesla when the vector coil set is in place and 3.08 Tesla when the scalar coil set is used. This allows measurements over a temperature range from 77-1000 Kelvin. This instrument has a biaxial coil set which allows us to measure two components of the magnetic moment, i.e. the moment parallel to the applied field and the moment perpendicular to the applied field. The coil set is fixed to the pole pieces of the

magnet. The sample itself can be rotated to change the direction of the field with respect to the sample.

2.4.2 The Torque Option

The Torque Magnetometer option measures the torque exerted on the sample when exposed to an external magnetic field. The torque is typically measured as a function of the field angle and the applied magnetic field. The Torque Magnetometer option is required for the measurement of the magnetic anisotropy of the sample. Torque measurements are done at room temperature with an accuracy of 1%. It can measure the torque at the range of 1-400 dyne-cm in fields up to 28.5 kOe. This approach uses 5 mm pole faces at 10 mm distance. Noise is below 0.005 dyne cm with averaging. The switch between the VSM and torque option is easy.

2.4.3 The Temperature Control Option

The temperature control system allows us to study magnetic properties at a high and low temperature range from 70 K to 1000K. Heat or cold can change the properties of a magnetic material. For example, above the Curie temperature, the ferromagnetic and ferrimagnetic materials change into paramagnetic material and above the Neel temperature the antiferromagnet changes into a paramagnet. Note that above T_c , if a sufficiently large magnetic field (1 or 2 T) is applied then forced magnetism will appear. This is because the applied magnetic field energy wins over the temperature effects.

To measure the effect of temperature on the magnetization of a sample, the sample temperature can be varied by raising the quartz cryostat/oven. Argon gas is used for measurements above RT and nitrogen gas and liquid nitrogen is used for measurements below RT.

2.4.4 The Magnetoresistance option

The magnetoresistance option provides a 4-point probe to measure the resistance of a thin film sample as a function of the magnetic field, temperature, and field angle. It can measure the resistance between 1 to 10000 ohms, up to 100 kHz in the voltage range of -10V to 10V with an accuracy of 0.01%.

2.4.5 The MOKE Option

The MOKE option offers the ability to do very fast longitudinal or perpendicular Kerr measurements. Typical measurement time for a hysteresis loop with thousands of points is less than 1 minute. Switching between VSM and MOKE options (and back) takes less than 1 minute and doesn't require gap changes or recalibration [44].

2.4.6 FMR Option

In addition to the option mentioned above, the MicroSense tool will allow for FMR measurements that can help in determining the magnetic anisotropy of the samples. The

FMR is a spectroscopic technique to measure the magnetization resulting from magnetic moments of unpaired electrons of ferromagnetic materials. The FMR option also measures damping and gyromagnetic ratio. It can measure thin-film down to 1.4 nm. Note that MOKE, FMR, and anisotropy all depend on spin-orbit interaction.

2.5 Available Measurement procedures for the VSM

The EZ VSM at Texas State University supports the following types of pre-defined measurements:

2.5.1 Virgin Curve

Virgin curve is also known as the initial magnetization curve. It measures the magnetic behavior of the demagnetized sample as a function of the applied field. The measurement is done on an initially demagnetized sample or after demagnetizing (which can be obtained by applying a field equal to H_r to the previously saturated sample) the sample by measuring the magnetic moment of the sample as a function of the applied magnetic field that is slowly increased from zero to a certain maximum value.

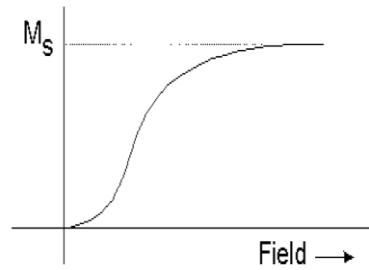


Figure 2.6. Virgin curve of the demagnetized sample [41].

A magnetic sample can be demagnetized in a number of ways. The easy VSM at Texas State University supports the following two different ways.

a. AC demagnetizing by means of applying a series of decreasing fields of alternating polarity. To AC-demagnetize a sample one needs to provide two parameters, i.e. the starting field value, and the AC demagnetization factor.

b. DC demagnetizing by applying a field just high enough to reverse half of the particles or domains in the sample. This field is equal to the remanent coercivity.

A demagnetized sample means that the summation of magnetization vectors of all the particles or domains or grains leads to zero. In AC demagnetization of the sample, the positively magnetized particles and negatively magnetized particles are equally spread. In the DC demagnetization process, the polarity of high field switching particles and low field switching particles becomes opposite. This is because the particles in the material have some sort of spread in their individual switching fields. Some of the particles switch at low field and others at high field.

2.5.2 AC Remanence Measurement

It measures the resistance of the material to AC magnetic fields. The sample is first saturated in a positive field, after which applied field is reduced to zero. Then the sample is subjected to a small AC field with decreasing amplitude. When the AC field reduces to zero, the remanent magnetization is measured and plotted against the initial amplitude of the AC field. Next, the AC field is applied again with a larger starting amplitude. This process is repeated until the remanent magnetization reduces to zero. The resulting curve looks like shown below.

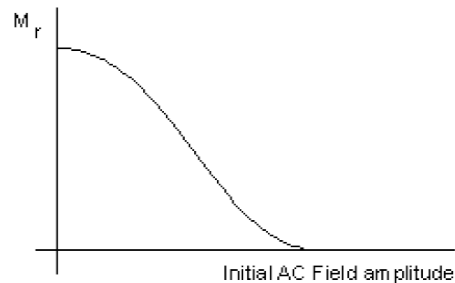


Figure 2. 7. AC remanence measurement [41].

2.5.3 Isothermal Remanence Measurement (IRM)

The Isothermal Remanence Measurement (also known as "forward remanence") measures the remanent magnetization as a function of an increasing magnetizing field starting from a demagnetized state.

For this, the sample is first demagnetized. Then a small field H_1 is applied, after which the field is reduced to zero and the remanent magnetization is recorded. Next, a somewhat larger field H_2 is applied and subsequently removed, after which next remanent magnetization is recorded. For each step, the remanent magnetization is plotted against the previously applied field [45][41]. This can be understood from the graph shown in Fig. 2.8. Starting from the demagnetized state (a) the field is increased to b, from which field is reduced back to zero. The remanence magnetization at c is then plotted at the field of b. Next, a slightly larger field is applied so that the field increased to d, from which is reduced to zero again. The remanence magnetization at e is then plotted at the field of d. This procedure is repeated until the resulting remanent magnetization is constant and equal to the remanence after saturation

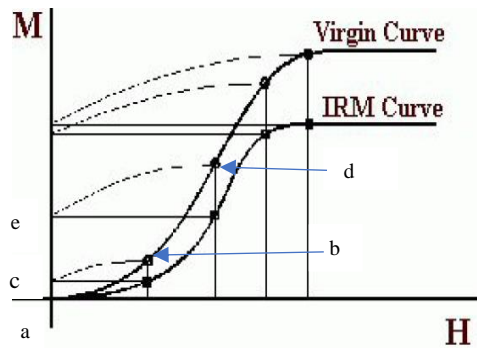


Figure 2. 8. IRM measurement procedure [41].

For many materials, the shape of the IRM depends significantly on the method of demagnetization. In an AC demagnetized sample, the magnetization direction of different

regions of high and low switching fields are equally spread. However, in DC demagnetized state the half of the material with the lowest switching fields is magnetized in one direction compared to the other half of the material with the higher switching fields.

2.5.4 DC Demagnetization Measurement (DCD)

The DC-demagnetization measurement (also known as "reverse remanence") measures the remanent magnetization as a function of the previously applied field starting from the saturated state.

First, the sample is saturated in the maximum negative field. Subsequently, a small positive field is applied and removed and the magnetization (at zero fields) is measured and plotted against the previously applied positive field. Subsequently, a slightly larger positive field is applied and removed. The resulting magnetization is again measured as the next point. This can be understood from the graph shown in Fig. 2.9 below. Starting from the negative saturation point (a) the field is increased to b, from which the field is reduced back to zero. The remanence magnetization at c is then plotted at the field of b. Next, the slightly larger field is applied so that the field increased to d, from which the field is reduced back to zero again. The remanence magnetization at e is then plotted at the field of d. This procedure is repeated until the resulting remanent magnetization is constant and equal to the remanence after saturation [45],[41].

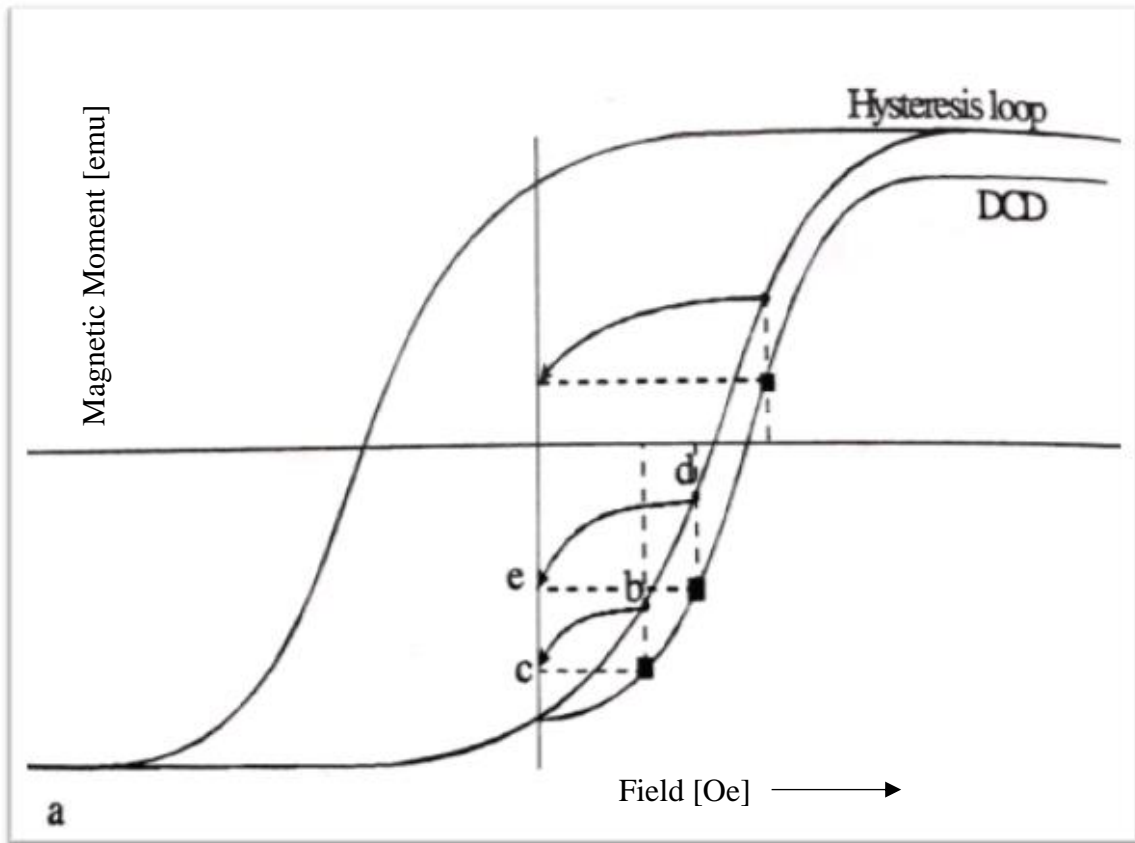


Figure 2.9. DCD measurement procedure [45].

In DCD, the field at which the curve crosses the horizontal axis is called the remanent coercivity, H_r . The value of H_r is always related to the average switching field. In the remanent state, the magnetization always points along the easy axis. Therefore, the projection of the unswitched part of the magnetization and the switched part of the magnetization cancel out leaving total magnetization zero.

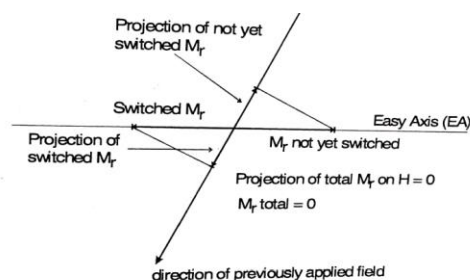


Figure 2. 10. when the projection of M_r on H is zero, M_r is also zero [45].

The DCD is often compared to the IRM since it is believed that the combination of the IRM and DCD data gives insight into the magnetic interaction in the material. If IRM and DCD measurements are combined as one measurement, it will result in only a single data file for these two measurements. The advantage of doing this is that the field set up for these two measurements will be identical and, after this measurement, the software can automatically generate a Henkel, Delta M or Delta H plot. Each of these plots represents the same data and information in a different way [45],[41].

Note that the AC remanence, the IRM, and the DCD measurement method all measure the remanent magnetization. For the AC remanence measurement and the DCD measurements, one starts from the saturated state, while for IRM measurements one starts from the demagnetized state.

2.5.4.1 Henkel Plot

Henkel plot shows the normalized DCD(H) curve as a function of normalized IRM(H) values which are obtained in the same field. It is presented together with the straight line representing the Wohlfarth relation which is a system of noninteracting particles. If the measured curve lies above the Wohlfarth line, the system shows positive (magnetizing) interaction. On the other hand, if the curve is positioned below this line, the system is said to show negative (demagnetizing) interaction. Positive interaction is governed by cooperative switching and the exchanging interaction, whereas negative interaction is caused by dipolar interaction. Exchange interaction is a quantum mechanical effect that occurs between identical particles and is responsible for ferromagnetism. The exchange interaction acts to align atomic dipole moment parallel to one another. In fact, all materials show both types of interaction, but in measurements, only the dominant type of interaction is observed [45].

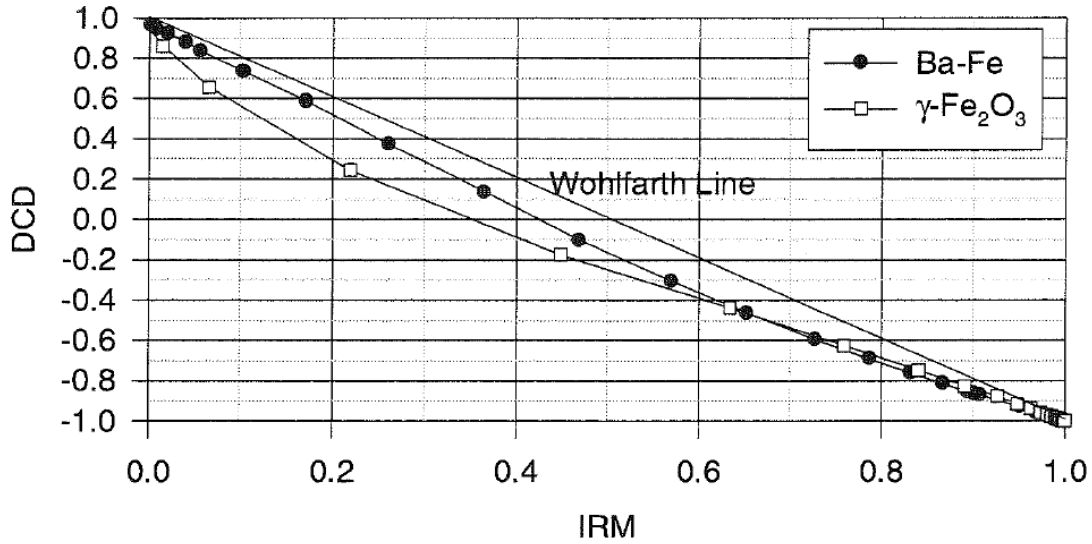


Figure 2.11. Hankel plot for gamma-Fe₂O₃ and a Ba-Fe floppy[45].

2.5.4.2 The delta-M Plot

The delta-M plot also gives the same information as the Henkel plot does. This plot is obtained by subtracting the normalized IRM(H) curve from the normalized DCD(H) curve.

$$\partial M(H) = \frac{DDC(H)}{DDC(\infty)} - 2 \frac{IRM(H)}{IRM(\infty)} + 1 \quad (2.8)$$

A positive delta-M in a delta-M plot indicates positive (magnetizing) interaction and a negative delta-M in a delta-M plot indicates negative (demagnetizing) interaction. The delta-M plot is the most frequently used method because it shows the difference between DCD and IRM much stronger than the other methods such as the Henkel plot.

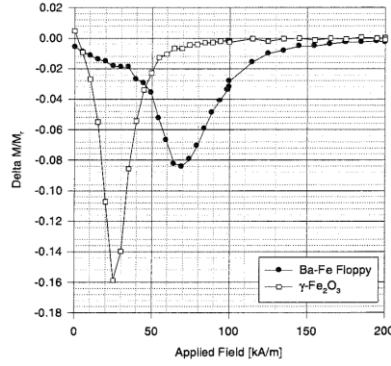


Figure 2.12. delta-M plot for gamma-Fe₂O₃ and a Ba-Fe floppy [45].

2.5.4.3 The delta-H plot

The delta-H plot is another way to represent the same information. This is a very useful way of representing data because it provides quantitative information on the interaction field. The curve is obtained by subtracting the H values at which the normalized DCD curve has the same value as a 2IRM-1 curve.

$$\partial M(H_{DCD}) = H_{DCD} - H_{IRM} \quad (2.9)$$

Where H_{DCD} and H_{IRM} are defined by

$$\frac{DCD(H_{DCD})}{DCD(\infty)} = 2 \frac{IRM(H_{IRM})}{IRM(\infty)} - 1 \quad (2.10)$$

This method is very sensitive to noise; therefore, the delta-H curve is obtained from smoothed data.

2.5.5 Hysteresis Loop Measurement

The hysteresis loop is the representation of the behavior of the magnetization as a function of the magnetic field. It is the most standard of all of the magnetic measurements. Many of the magnetic properties and parameters including remanence, coercivity, permeability, saturation magnetization, the easy and hard axis can be determined from the hysteresis loop.

The hysteresis loops depend strongly on the type of magnetic material. For instance, hard magnetic materials generally show low initial permeability (close to the origin) and high coercive force. These materials are generally used for permanent magnet applications. On the other hand, soft magnetic materials exhibit high initial permeability and also low coercivity. These materials are used for transformers or a magnetic recording heads or applied in novel sensors. Since both the types of ferromagnetic materials have different magnetic parameters associated with the hysteresis, their magnetization reversal behavior can be very different.

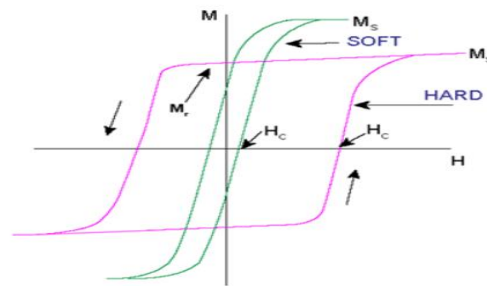


Figure 2.13. Hysteresis loops for hard and soft magnetic materials [46].

2.5.6 Angular Remanence Measurement (ARM)

The angular remanence measurement measures the remanent magnetization of the sample as a function of the field angle. This is performed by turning the sample to a certain angle, applying the maximum field, reducing the field to zero and measuring the resulting moment. This measurement is repeated for different angles and the remanence is plotted as a function of the field angle.

The angular remanence curve is very useful to determine the hard and easy axis direction as well as the anisotropy direction of the sample. Furthermore, the magnitude and direction of the remanence can be determined from the ARM curve. The angle where the minimum remanence is reached is the hard axis of the material. Conversely, the angle where M_r reaches its maximum value is the easy axis of the material. The direction of remanent magnetization is equal to the average anisotropy direction. For the materials having well defined preferential orientation, the remanence angle remains constant for the large field angle range, for the materials with a worse orientation, the area where the remanence angle stays constant will be much smaller or absent. Figure 2.7 below shows the angular remanence as well as the magnetization angle as a function of the field angle for Co- γ Fe₂O₃ VHS tape, Co- γ Fe₂O₃ floppy tape, and ME tape. All measurements were done with the transverse holder. Note that VHS tape and ME tape have a magnetic anisotropy, while the floppy tape is magnetically isotropic. [45],[41].

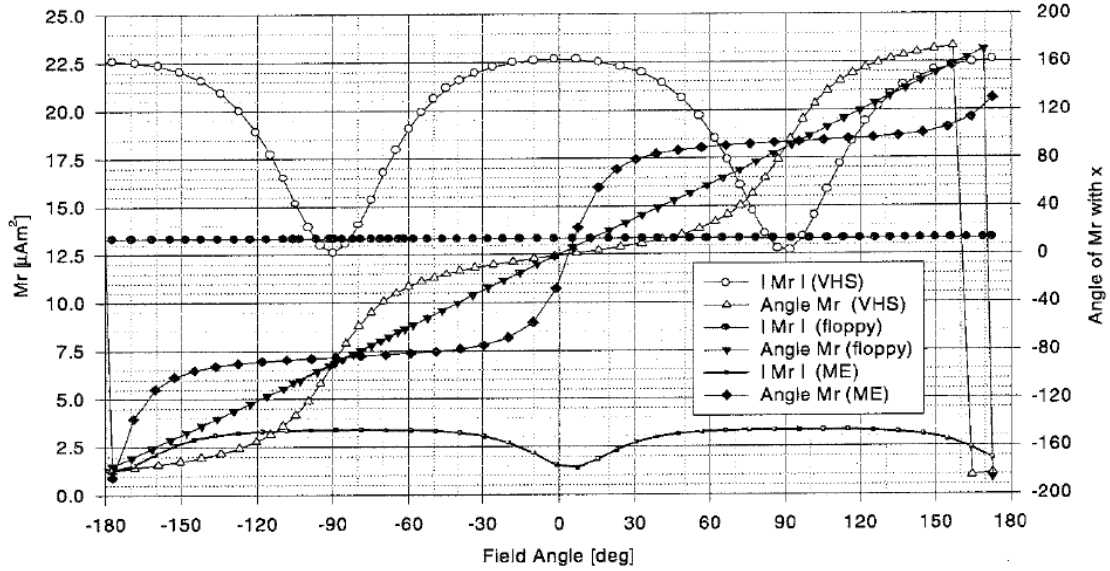


Figure 2. 14. Angular remanence and magnetization angle as a function of field angle for Co- γ Fe $_2$ O $_3$ VHS tape, Co- γ Fe $_2$ O $_3$ floppy tape, and ME tape all measured in the plane of the sample [45].

2.5.7 Time-Dependent Measurement

It provides the possibility of checking the stability of the magnetization at different applied fields. The sample is first saturated (for example, in a positive field) after which a negative field close to the coercivity (H_c) is applied. Then, over time, change in magnetization (M) is monitored.

The software automatically performs this measurement for a series of different measurement fields from which the highest magnetic time-dependence can be found. A plot of the magnetic moment as a function of time, as well as a plot of the relative change in magnetization as a function of the measurement field, will be obtained from the time-dependent measurements. One may choose the temperature and field angle at which the

measurement is taken. Upon our request, MicroSense modified the software so both the X and Y-signals are recorded as a function of the time.

2.5.8 Temperature Scan

A temperature Scan is a method used to find the Curie and Compensation temperature by measuring M_s and or M_r as a function of the sample temperature.

To measure the effect of temperature on the magnetization of the sample, the sample temperature can be varied by raising the cryostat/furnace quartz tube around the sample.

This requires optional hardware i.e. a temperature chamber that covers both 'cold' and 'hot' temperatures in a continuous range with the use of Liquid Nitrogen and Argon.

Argon gas is used for high temperatures. Liquid Nitrogen is used for low temperatures.

The temperature scan can be run in step mode or in Sweep Temperature mode [41].

2.5.9 Torque Measurement

The torque measurement measures the torque on a sample exposed to a magnetic field as a function of rotation angle and applied field. These are regarded as very important types of measurements since they present the information on the preferential direction of the magnetization in the sample. Similar to angular remanence curve, one can find the easy and hard axis in the sample from the torque measurements. In addition, the anisotropy constants can be determined from torque measurements. In most of the cases, torque

measurements are performed with a torque magnetometer. However, the torque curves can also be measured with a biaxial VSM.

When a field is applied to the sample with a certain angle, the sample will experience a force (torque) that tries to rotate the sample so that its magnetization (M) aligns with the field. At the same time, torque is exerted on the magnetization by the crystal structure (i.e magnetic moment of the sample the parallel to the field) as soon as the magnetization rotates away from the easy axis.

For the material with a single easy axis perpendicular to the hard axis (e.g Co, hcp structure) the energy density associated with magnetic anisotropy is given by:

$$E_a = K^* \sin^2(\theta) + K_2 \sin^4(\theta) \quad (2.11)$$

Where K^* is all first-order anisotropy constants and θ is the angle between the easy- axis (anisotropy) direction and magnetization.

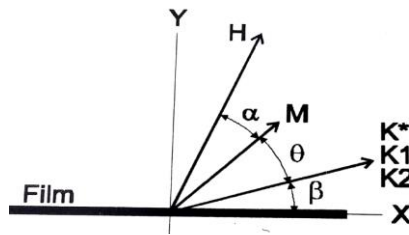


Figure 2.15. Angle definition for torque calculation [45].

Torque is exerted on the magnetization by the crystal structure (i.e magnetic moment of the sample parallel to the field) and given by:

$$L_{K-on-M} = \frac{\partial E_a}{\partial \theta} = K^* \sin(2\theta) - \frac{K_2}{2} \sin(4\theta) \quad (2.12)$$

This torque will tend to turn the magnetization back to the easy axis. The torque exerted by the field is given by:

$$L_{H-on-M} = -\mu_0 M \times H = -\mu_0 M H \sin \alpha \quad (2.13)$$

Where α is the angle between magnetization and field. At equilibrium, the magnetization direction is constant, therefore,

$$L_{K-on-M} = -L_{H-on-M} \quad (2.14)$$

The torque with torque magnetometer (TMM) can be determined directly as a function of field direction. If the field is applied either along with the easy ($\theta = 0$ degree) or hard axis ($\theta = 180$ degree), the torque will be zero. From equation (2.12), neglecting second order anisotropy constant, the first order anisotropy constant can be derived from the following relation:

$$L_{means} = L_{K-on-M} = K * \sin(2\theta) \quad (2.15)$$

To calculate K^* , one has to know the angle (θ) between the easy axis and the magnetization. However, this angle can't be measured by TMM. At $H=\infty$, the magnetization is along the field direction and θ will be in the field direction. The K^* is determined by calculating L from equation (2.15) with θ equal to the field direction and plotting L versus $1/H^2$ and extrapolating to $1/H^2=0$.

The torque can also be determined from the angular measurement of the perpendicular component (this component will decrease with the increasing field) of the magnetization vector at the constant field because this measurement provides both magnitude and direction of the magnetization. The torque exerted by applied field on magnetization can be calculated from equation (2.13) [45],[41].

The torque vs. angle plot is Fourier analyzed from which the software automatically and yields the anisotropy constants and the easy and hard axis of the magnetization. The second harmonic amplitude is equal to first-order anisotropy and the second harmonic phase is equal to anisotropy direction [41].

2.5.9.1 Field dependence of K^*

If the torque calculated from the VSM measurement is plotted as a function of the angle between the sample and magnetization yields a $\sin(2\theta)$ function provided higher order anisotropy constants are negligible. K^* is then equal to the amplitude of the sine function. Figure 2.15 shows the torque measured on the gamma- Fe_2O_3 sample as a function 2θ . The figure shows the sine function indicating the absence of second-order anisotropy constants.

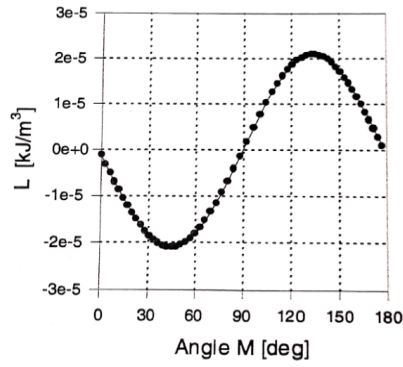


Figure 2. 16. Torque as a function of the angle of the magnetization on a gamma-Fe₂O₃ [45].

2.5.9.2 Demagnetization (shape) anisotropy constant

Unlike the magnetizing field, the demagnetizing field pulls the magnetization toward the plane direction that creates an additional torque. This torque can be created by first-order anisotropy K_d , defined by:

$$E_{\text{shape}} = K_d \sin^2 \theta = -(N_y - N_x) \frac{1}{2} \mu_0 M_s^2 \sin^2 \theta \quad (2.16)$$

Where θ is the angle between the film plane and magnetization and N_x and N_y are the demagnetizing factors parallel and perpendicular to the thin film. For an infinite plane, one can consider $N_y=1$ and, the value of N_x depends on the aspect ratio (k). Following the ellipsoid equation [47] is used to estimate N_x :

$$N_x = \frac{1}{2} \frac{k^2}{(k^2 - 1)^{3/2}} \sin^{-1} \sqrt{\frac{k^2 - 1}{k}} - \frac{1}{k^2 - 1} \quad (2.17)$$

The variation of N_x as function k is shown in the following figure.

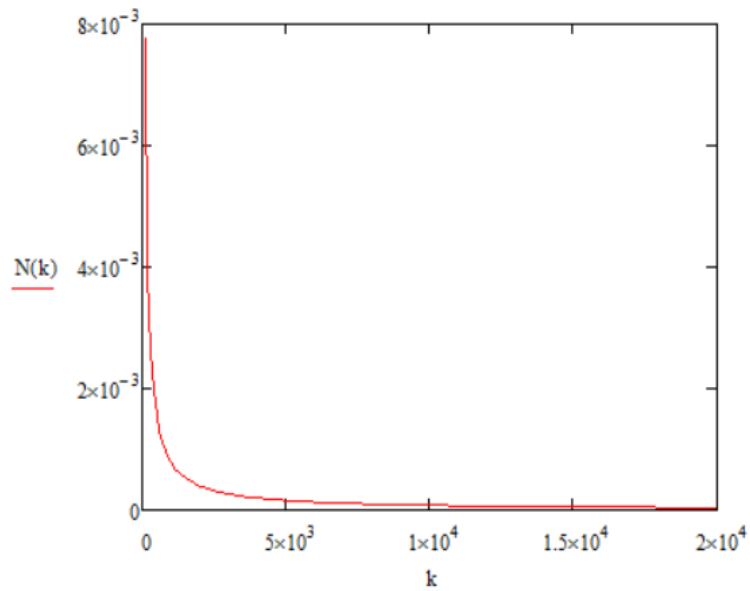


Figure 2. 17. The variation of N_x as a function k .

$$K_d \approx -\frac{1}{2} \mu_0 M_s^2 \quad (2.18)$$

Thus, K^* is defined as the sum of all first-order anisotropy constants including the demagnetization.

$$K^* = K_1 + K_d + \dots \quad (2.19)$$

2.5.10 Miyajima Method of Torque Measurement

The Miyajima method of Torque measurement provides a fast and easy way to determine the anisotropy of a magnetic material.

In this method, the torque on a sample is measured at an angle of 45 degrees with the easy axis of the sample. The torque is measured at different (high) fields and plotted on a graph of L/H versus L . The anisotropy can be determined by extrapolating the measured data and finding the slope of the extrapolated curve. The saturation magnetization is determined from the intersect of the slope of the extrapolated curve with the L/H axis.

The anisotropy that the software calculates is the effective anisotropy (K_{eff}). Depending upon the type of sample, the uniaxial anisotropy (K_u) can be calculated as follows. For two-dimensional random samples and measurement is done 45 degrees out of a plane, K_{eff} is given by:

$$K_{\text{eff}} = \frac{1}{2}K_u + \frac{1}{2}M_s^2 \quad (2.20)$$

If the anisotropy of individual particles aligns with the plane,

$$K_{\text{eff}} = K_u + \frac{1}{2}M_s^2 \quad (2.21)$$

For three-dimensional random samples,

$$K_{\text{eff}} = \frac{1}{2}M_s^2 \quad (2.22)$$

2.6 Demagnetizing Field Correction of Measured Data

The field inside a specimen (H_i) is different from the applied field (H) because of the magnetization of the specimen. The magnetization poles produce a demagnetizing field (H_d) inside the specimen which has opposite direction than that of magnetization. The strength of the demagnetization field H_d is calculated by:

$$H_d = -N_d M$$

Where N_d is a demagnetizing factor. The demagnetizing factor depends on the shape of the specimen. For ball-shaped specimen, the demagnetizing factor is 1/3 in all direction, in thin film 1 in a perpendicular direction and zero in the in-plane direction. The demagnetizing field correction function corrects for the demagnetizing field as follows:

$$H_{\text{corrected}} = H_{\text{applied}} - H_{\text{internal}} \quad (2.2)$$

Great attention should be paid while choosing the correct demagnetization factor.

Different parameters including the shape of the sample, proportion, orientations and sample thickness should be filled in correctly. If the sample volume is incorrect, the sample magnetization (sample moment/sample volume) will be incorrect and the demagnetizing field will be incorrect [41].

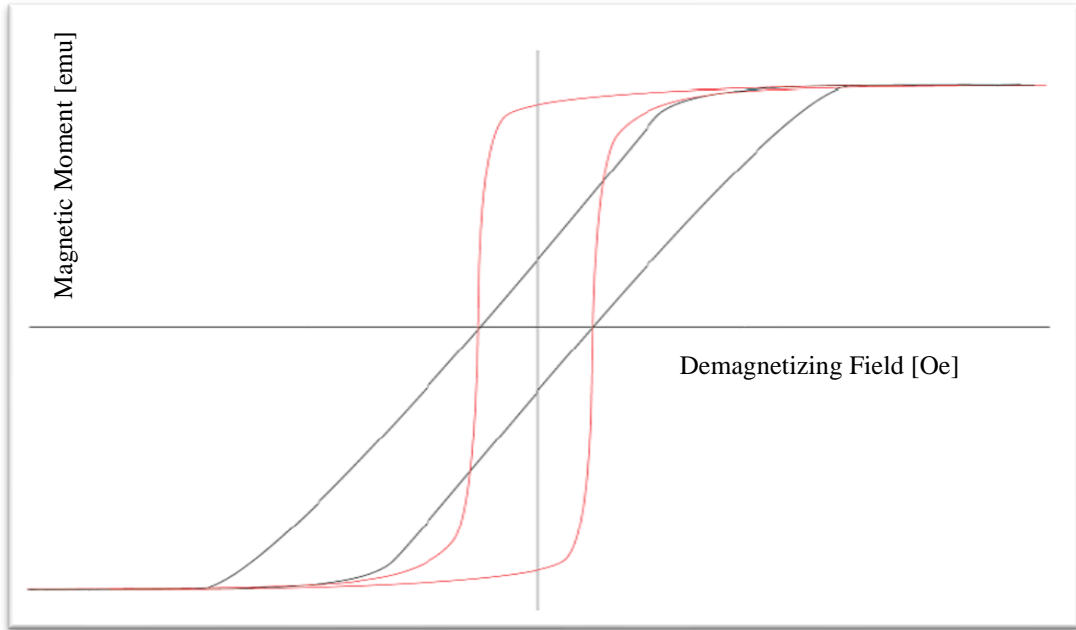


Figure 2. 18. Loop before applying the demagnetizing field (in grey) and after applying the demagnetizing field (in red) [41].

3 LAB INSTRUMENTS AND RESULTS

3.1 AJA Magnetron Sputtering System

The AJA Magnetron Sputtering System is a confocal thin-film deposition instrument which is usually utilized to deposit thin-films of metals and insulators on silicon wafers or other substrates. The system is equipped with five AJA high vacuum magnetron sputtering sources that are powered by RF generators (300W) or DC generators (500W) for single, multi-layer, or co-deposition. The system contains 3 DC and 2 RF magnetron sputtering guns. The system uses a LabVIEW based Phase II-J computer control system allowing both manual and automated modes [48].

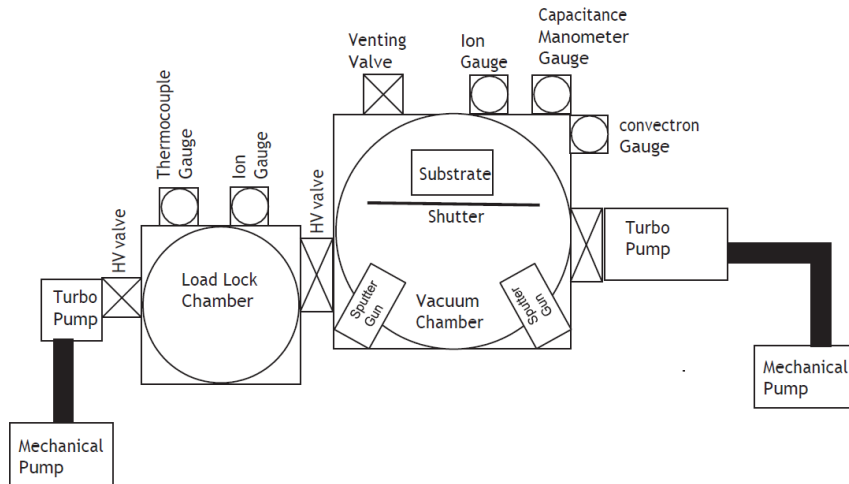


Figure 3. 1. AJA sputtering system.

The background vacuum level of the main chamber attains pressure as low as $4\text{E-}8$ Torr, while in the load lock system it often stands at $\sim 10^{-7}$ Torr. One is allowed to open the valve in between the deposition chamber and the load lock system to transfer the sample when the ratio of the pressures in both chambers is less than a factor 100 apart. A clamp at the end of a z-stage holds the substrate holder. The substrate holder can be rotated (from 0-40 rpm) while executing the deposition process. The substrate holder has a heating capacity of $\sim 700^\circ\text{C}$. To keep the targets cool while depositing, cold water is supplied by the chiller around the targets. Each deposition gun has its own shutter which can be opened or closed by the computer. The oxygen gas is let into the chamber at the substrate holder while the argon sputter gas is let into the chamber via the sputter guns. During the sputtering process, argon ions are accelerated into the target consisting of the material to be deposited, and due to the transfer of the energy and momentum, some of the target atoms are ejected. These ejected atoms form an atom beam and are deposited on the substrate. In the Direct Current (DC) sputtering mode, positively charged ions are accelerated to the target by a negative potential of hundreds of volts. Electrons created by impacting ions can also cause further ionization of the gas. However, this technique is limited to conducting materials such as metals and doped semiconductors. The main reason is that the non-conducting insulating materials take on charges over time which can result target poisoning. When too much charge is accumulated in the target, the sputter gun will no longer be able to sustain a plasma as the incident Ar ions are repelled by the charged target. To prevent the charge build-up RF sputtering is used for insulating targets. A Radio-Frequency (RF) alternating current (AC) voltage is applied to the target avoiding charge build-up in the target. Sputtering with an alternating voltage is called

RF-sputtering. To ignite an RF gun requires a large chamber pressure which depending on the material can be over 30 mTorr. As it is easier to strike a DC gun, we typically first ignite a DC sputter gun in the system. All DC guns in the system will strike at 15 mTorr. This pressure can be obtained by setting the main valve to the throttle position and flowing both Ar mass flow controllers at maximum flow, i.e. 50 sccm and 100 sccm. Once a DC gun is on, it is easier to start an RF gun as the plasma of the DC gun puts electrons and ions in the chamber. Once the RF guns are on, the DC gun is switched off. The samples reported on in this thesis were made by RF magnetron sputtering. Permalloy films were RF sputtered from NiFe targets using argon as a sputtering gas. Permalloy oxide films were RF sputtered from NiFe targets using a mix of argon and oxygen as a sputter gas. This deposition method is often referred to as reactive RF sputtering.

3.1.1 Sample preparation

The samples were deposited in an AJA Orion Sputtering System that is capable of depositing metal and dielectric films on substrates up to 4 inches in diameter. The system utilizes a motorized, rotating substrate holder to achieve excellent uniformity, allow the co-deposition of alloy films and/or the deposition of thin-film and multilayers [48]. The thin films reported on in this thesis were deposited by using different techniques. The Permalloy oxide (PyO) thin films were deposited from metallic Permalloy targets by reactive RF magnetron sputtering using two guns which are located on opposite sides of the chamber. The angle they make with the normal of the substrate holder is 107 degrees. To further improve the homogeneity of the films the substrate holder was rotated during

deposition. Films were deposited on glass microscope slides and Si wafers covered with a 2nm thick native SiO₂. All the films were deposited at room temperature. Prior to deposition, the substrates were sequentially rinsed in water, acetone, and methanol. Each next solvent was used to rinse the preceding solvent of the wafer. The last cleaning step was done on a spinner with isopropyl alcohol. The chamber was pumped down to a base pressure of $< 4 \times 10^{-7}$ Torr by a roughing and a turbo pump. Two similar RF sources at a power of 200 Watt each were used for deposition. The flow of the gas was controlled by an MKS mass flow controller (Ar) and an MKS mass flow meter (O₂). The total flow was kept at 50 sccm resulting in a sputtering pressure of approximately 8 mTorr. After opening the shutters mounted on the chimneys of the guns, the targets were pre-sputtered for 1 minute before the deposition rate was measured with the QCM (quartz crystal monitor) mounted to the back of the substrate shutter.

The accumulated film thickness was measured with the QCM over a period of 50 seconds prior to opening the substrate shutter and the deposition rate was calculated from this accumulated thickness. The total deposition time for each sample was kept at 1200 seconds. During the deposition, the substrate was rotated at 30 rpm. The deposition was done at room temperature. This method has been shown to produce high-quality polycrystalline films. The thickness of the thin film samples was verified by ellipsometry. The deposition rates calculated from the ellipsometry thickness and the deposition time were similar to the rate measured with the QCM. The films sputtered at low oxygen flow had a typical thickness of around 140 nm, while the films sputtered at 20 sccm were much thinner (17 nm). All samples were covered with a 5 nm thick Au or Pt cap layer to

avoid oxidation when taken out of the sputtering system. This layer was sputtered with a DC magnetron sputter gun at 50 Watts and 30 sccm Ar flow.

The Permalloy thin films reported in this thesis were deposited on 3” diameter fused quartz wafers. The material was sputtered from metallic Permalloy targets by RF magnetron sputtering using a single gun or two guns. The Permalloy was sputtered using argon gas while throttling the HV valve of the main chamber. The gas flow during deposition was varied from 5-30 sccm resulting in sputtering gas pressure 2-5 mTorr. For some of the depositions, the sample holder was rotated at maximum speed during deposition while other depositions were performed without rotating the sample holder during the deposition. The RF source was set to 200 watts.

3.1.2 Effect of Oxygen flow on deposition rate

Fig. 3.2 below shows the measured deposition rate as a function of the oxygen flow for our NiFeO deposition process. The total flow rate was kept at 50 sccm for this experiment. The deposition rate shows a maximum as a function of the oxygen flow. At low oxygen flow rates, the deposition rate increases with oxygen flow. We believe that this increase (24%) is due to the introduction of oxygen in the system resulting in oxidation of the freshly deposited Permalloy film. As for a fully oxidized film, one would expect an increase of 27%, the films sputtered at low oxygen flow are not stoichiometric but contain a significant amount of oxygen vacancies. At higher oxygen flow, i.e. above 5 sccm, the deposition rate decreases strongly. We believe that this is caused by the oxidation of the targets. This effect is often referred to as poisoning of the targets [49]. It

is well-known that NiFe-oxide has a much lower sputter rate than metallic Permalloy. Although oxidation of the targets also takes place at lower oxygen flow rates, at those low oxygen flow rates the removal rate of material from the targets is much higher than the rate with which an oxide layer is formed on the targets. So below 5 sccm, the surfaces of the target are clean of oxide and most of the sputtered material is metallic Permalloy. From 5 sccm and up the removal of the material from the targets can no longer keep up with the oxidation and the deposition rate collapses. For these oxygen flow rates it is expected that the sputter beam also contains oxygen atoms and NiO, FeO, and possibly NiFeO clusters. Note that for our process the QCM deposition rate is significantly lower than the rate with which material is removed from the targets. The short mean free path of the sputtered atoms at 8 mTorr results in a diverging sputter beam that has a diameter significantly larger than the target diameter at the location of the substrate. From measurements of the deposition rate versus the substrate distance, we expect at least a factor 10 difference between the QCM rate at our substrate position and the target material removal rate.

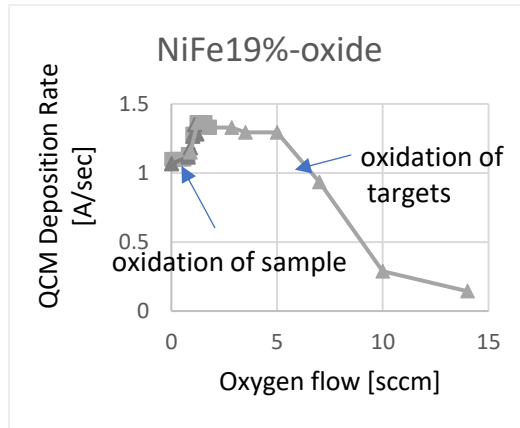


Figure 3. 2. Deposition rate as a function of the oxygen flow for NiFe-19% co-sputtering at 200 Watt.

3.2 Physical Property Measurement System

The Quantum design (Model 6000) the physical property measurement system (PPMS) is an instrument that allows for a variety of measurements to be performed in a variable temperature and field environment. Electrical, magnetic and optical measurements [50] can be performed at a temperature range from 1.9K to 300K. Magnetic properties are determined with the vibrating sample magnetometer (VSM) technique [51]. The PPMS has a superconducting magnet capable of producing a magnetic field ranging from -9 to +9 Tesla. The maximum sample size depends on the type of measurement technique [51]. For the VSM the maximum sample size is 4x4 mm².

3.2.1 Measurement procedure

To measure the magnetic properties by the PPMS certain procedure must be followed for the safety of both user and instrument. The system must be prepared for the VSM installation. The helium level in the system must be at least 70% to prevent the superconducting magnet from quenching. For each VSM measurement, the temperature, and magnetic field in the Multi Vu program are set to 300k and 0 Oe respectively, and then the system is vented. Before loading the sample, any existing sample in the sample chamber is removed. The coil set is inserted in the sample chamber using the puck-insertion tool. Then the sample tube is carefully lowered in the sample chamber until the centering ring touched the top flange. The linear motor is installed on the top flange, and the linear motor and VSM cables are connected to the system. The VSM is activated, and when it is ready, the chamber is opened, and the sample mounted on the sample holder is carefully lowered through the top of the linear motor. After sample loading, the chamber is closed and purged using the standard purge method. The sample position is set manually. Normally, the sample position can be set either manually or automatically, however, since our samples have a very weak magnetic moment, only the manual setting for sample position is possible. After the measurement, we followed the same procedure in reverse for sample unloading and instrument shutdown.

3.2.2 Measurement of magnetic properties of the sample

A Physical Property Measurement System (PPMS) with VSM attachments was used to measure the magnetic moment of the NiFeO samples. The magnetic moment of the samples was measured as a function of the magnetic field and temperature. The magnetic field was varied from -9T to 9T and the temperature was varied from 4K to 300K. The PPMS system and VSM attachments are shown in figure 3.2. The pick-up coils for this apparatus are located in the VSM puck (pictures c and d), which is inserted into the PPMS. For these measurements, the field was changed at a rate of 180 Oe/s, and most measurements were done at room temperatures. The PPMS VSM has a uniquely designed linear motor to vibrate the sample at a frequency of 40 Hz. A pickup coil set is placed around the sample. When the sample is moved the total magnetic field passing through the pickup coils fluctuates, and this magnetic flux induces an induction current in the coil set which is measured and recorded by the PPMS software. The induced current is proportional to the sample's magnetic moment. The sample-holder itself does hardly contribute to the signal as it extends above and below the pickup coils and vibrations of objects larger than the pickup coil distance will not cause significant flux changes.



Figure 3. 3. Left to Right: PPMS apparatus (a), VSM attachments for PPMS (b), photograph of the VSM puck (c), a cross-section of VSM puck (d), at Texas State University.

The magnetic moment in a material is not constant, but changes as the applied external field changes from a saturated positive value (M_s) to zero and then to the negative saturated value ($-M_s$). As NiO and NiFeO are antiferromagnetic materials, not a large magnetic moment is expected. Defects and the surface of the films, however, can have a magnetic signature. Since the moment of the film is small, a special technique is used to suppress the magnetic signature of the substrate which can be much larger than the thin film. Two techniques are employed:

1. A silicon wafer was used as a substrate because of the low magnetic moment of silicon (slightly diamagnetic) and the availability of thin wafers. Furthermore, it is rather easy to cut square samples from a single crystalline silicon wafer compared to cutting square samples from a fused quartz wafer.

2. Bare silicon tiles were mounted above and below the sample on the VSM sample-holder to suppress the magnetic signal of the diamagnetic silicon substrate [52][53][32].

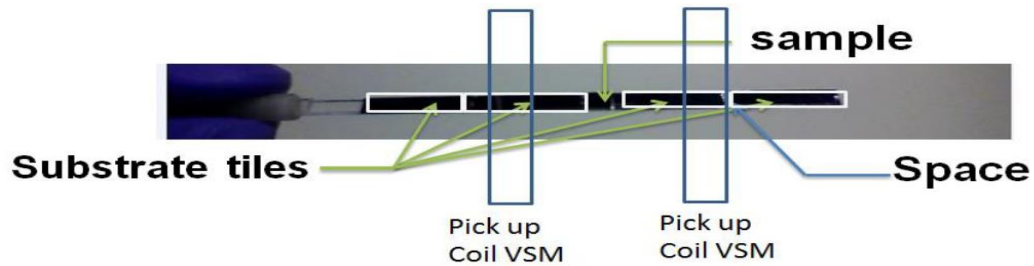


Figure 3. 4. The sample holder fully covered by the sample (in the middle) + substrate tiles. The effect if the substrate is suppressed since it is longer than the distance between the pick-up coils [54].

3.2.3 Variation of saturation magnetization with oxygen concentration

Fig.3.5 and 3.6 show the measured magnetic moment per unit volume as a function of the oxygen flow. A decrease in the saturation magnetization is observed for higher oxygen flows. This might be due to a more fully oxidation of the films sputtered at high oxygen flow. Note that NiFe-oxide was shown to have a rock salt crystal structure [55][56] and DFT calculations have shown it is antiferromagnetic [57]. A sharp decrease in the magnetic moment was observed when the oxygen flow was increased to 1.25 sccm. For films deposited at flows significantly above 1.25 sccm, the saturation magnetization slightly increases similar to what was observed by Twagirayezu on RF sputtered films

using a single source[32]. The decrease of the magnetization with oxygen flow is believed to be caused by a more complete oxidation of the material.

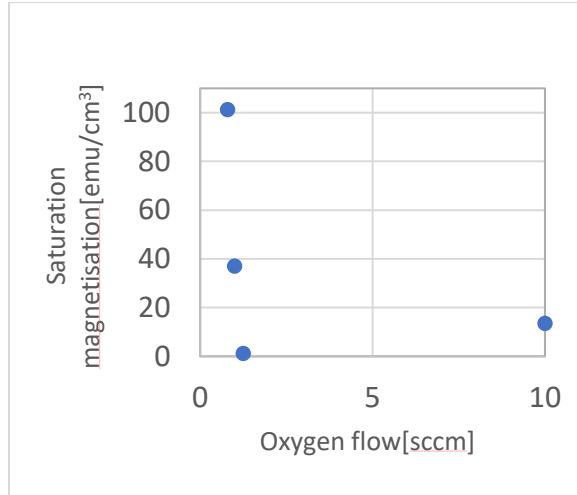
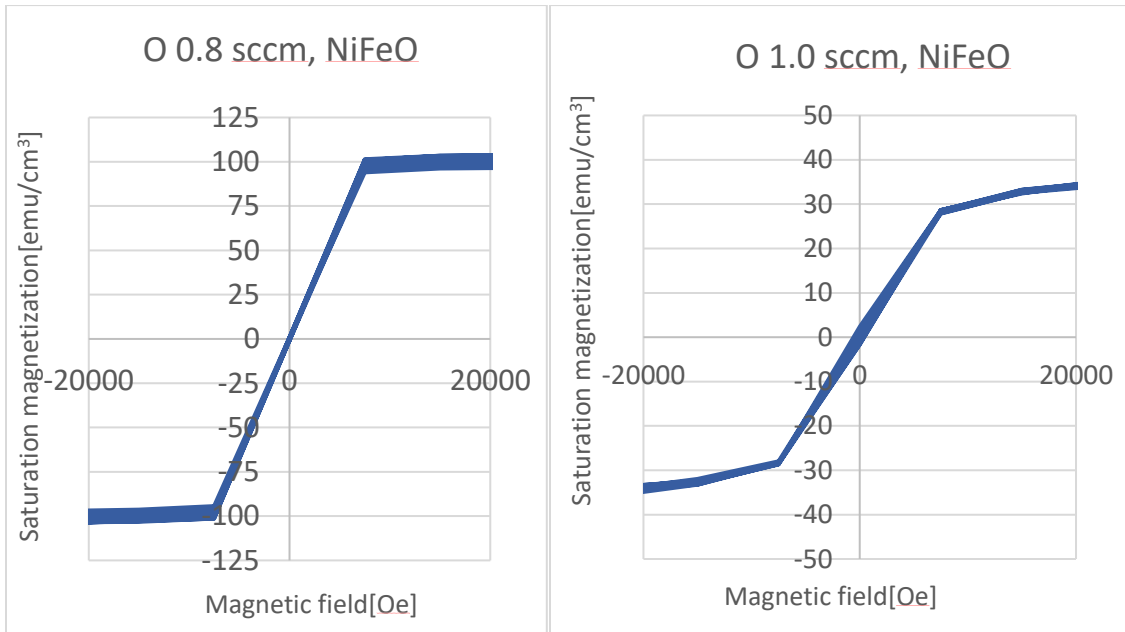


Figure 3. 5. Variation of saturation magnetization with oxygen concentration for different films.



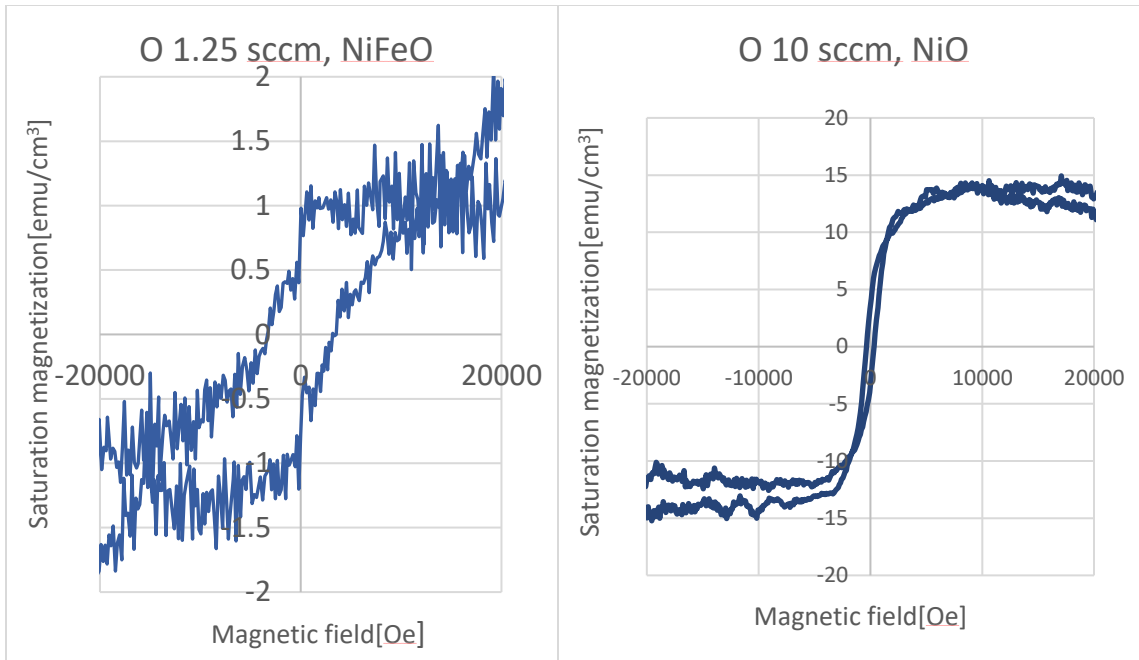


Figure 3. 6. Magnetic moment $m(H)$ per unit volume at 300K for NiFeO and NiO samples, sputtered at different O pressure. Shows a decrease in saturation magnetization at higher O pressure.

3.3 X-ray Photoelectron Spectroscopy (XPS)

The X-ray photoelectron spectroscopy (XPS) also known as electron spectroscopy for chemical analysis (ESCA) is the most widely used surface analysis technique because it can be applied to a broad range of materials and provides valuable quantitative and chemical state information from the surface of the material being studied. It is based on the photoelectric effect, which was discovered by Albert Einstein in 1905. The photoemission process from a solid sample takes place when a highly energetic photon interacts with matter, causing an electron to be removed from an atomic orbital or from a

band and to reach the vacuum level. The excitation energy must be large enough for the electrons to overcome the work function of the solid [58].

The surface analysis by XPS is performed by irradiating a sample with monoenergetic soft X-rays and analyzing the energy of the detected electrons. Mg K α (1253.6 eV), Al K α (1486.6 eV) or monochromatic Al K α (1486.7 eV) X-rays are usually used. XPS is a surface-sensitive technique because only the photo-electrons generated near the surface are able to escape and have a chance to be detected. Due to inelastic collisions with the sample's atomic structure, the photoelectrons originating more than 10 nm away from the sample's surface can't escape with sufficient energy to be detected [59]. Since X-ray photons are massless (zero rest mass) and chargeless, they are annihilated during photon-electron interaction with complete energy transfer during the interaction. If this energy is sufficient, it will result in the emission of an electron from the atom/ion or from the solid. Excess energy will be noticeable by measuring the kinetic energy (K.E) of the emitted electron. This kinetic energy is of a discrete nature and is a function of the electron binding energy (B.E.) which is given by [60]:

$$K. E. = h\nu - B. E. - \phi \quad (3.1)$$

Where ϕ is the work function of the specimen and $h\nu$ is the energy of X-ray photon.

The binding energy is regarded as the difference in kinetic energy between the initial and final state after the photoelectron has left the atom.

3.3.1 XPS Measurement Procedure

X-ray photoelectron spectroscopy (XPS) measurements were made using an XPS PHI Quantum 2000 Scanning ESCA microprobe. The XPS chamber contains an Al $\kappa\alpha$ X-ray source in which incoming X-rays are parallel to the surface normal. The system allows for measurements with an analysis resolution of about 1 eV [61]. The X-ray beam power was 50 W and the takeoff observation angle was 45° . The X-ray spot size was $200\ \mu\text{m}$ and the analysis was done on an area of $500\ \mu\text{m} \times 500\ \mu\text{m}$. Under these conditions, the information depth is approximately 10 nm. Prior to the scans, part of the Pt or Au cap layer was removed by argon sputtering. To avoid the effects of preferential sputtering of the NiFe-oxide on the XPS spectra, part of the Au or Pt cap layers were kept in place. As Au has a larger sputter rate, the samples with an Au cap layer were sputtered for only 1 min while the samples covered with a Pt cap layer were sputtered for 3 min. The pass energies were 187 eV for the survey and 58 eV for the high-resolution scans. All energies are referenced with respect to the main C peak at 284.8 eV.

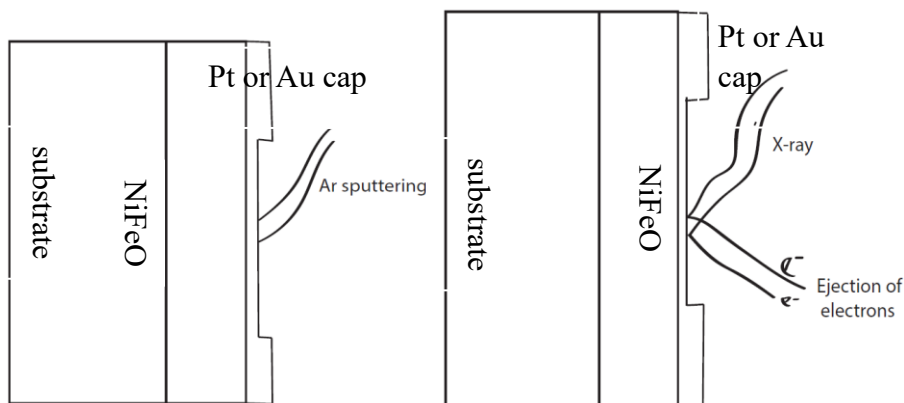


Figure 3. 7. XPS measurement procedure on NiFeO samples.

3.3.2 XPS measurement result

Fig. 3.8 shows the XPS spectrum of Ni(2p_{3/2}) and Fe(2p) of the samples sputtered at various oxygen flow rates. This is the XPS data obtained from the samples that had a Pt cap layer. Note that the ratio of the Ni⁰ to Ni²⁺ decreases with oxygen flow, but that the Ni⁰ peak is still visible in the Ni-spectrum for films sputtered at 20 sccm oxygen flow. The Fe-XPS spectra of the films sputtered at a different oxygen flow look very similar to each other (see Fig. 3.8). Our Fe spectra differ though from the XPS spectra of oxidized Permalloy films published in [61], which show a steep slope at 700 eV while all our films show a very gradual slope. The absence of a distinct Fe⁰ peak suggests that most Fe is oxidized, and oxygen vacancies prefer to reside next to nickel atoms. Since the resistivity of the films sputtered at 20 sccm O₂ is much lower than the films sputtered at 5 sccm, we believe that the films sputtered at 20 sccm oxygen flow contain metal vacancies. However, no Ni³⁺ peak was observed in our NiFe-oxide films [62]. The interpretation of the Fe-XPS spectrum is challenging as for Al K α radiation an Auger Ni-peak is present in the middle of the Fe-XPS spectrum, i.e., 712 eV. In addition, Pt has a peak in the Fe-XPS spectrum at 725 eV near the position of a metallic Fe peak. The XPS data for the samples covered with an Au cap layer is shown in Fig. 3.9. Note that the counts of the Au-capped samples of Fig. 3.9 are significantly lower than those of the Pt capped layers of Fig. 3.8. This suggests that the remaining Au cap layer in the samples of Fig. 3.9 is thicker than the remaining Pt cap layer in the samples of Fig. 3.8. A detailed analysis of the data of Figs. 3.8 and 3.9 using a rough estimate of the sputter rates of Au and Pt suggests that we might have sputtered through part of the Pt layer for the results shown in Fig. 3.8 and that

the ratio of the Ni⁰ to Ni²⁺ oxygen peaks in Fig. 3.8 might have been affected by preferential sputtering of oxygen of part of the NiFeO films of Fig. 3.8. The Fe spectra of Fig. 3.9 are similar to the Fe spectra of Fig. 3.9. It might not be possible to distinguish the metallic Fe-XPS peak at 707 eV from the Ni Auger peak at 712 eV. The gradual slope observed in the Fe spectrum might be characteristic for reactive RF-sputtered PyO films. It is definitely not caused by the cap layer and does not depend on the X-ray source, so is unlikely due to the Auger peak of nickel.

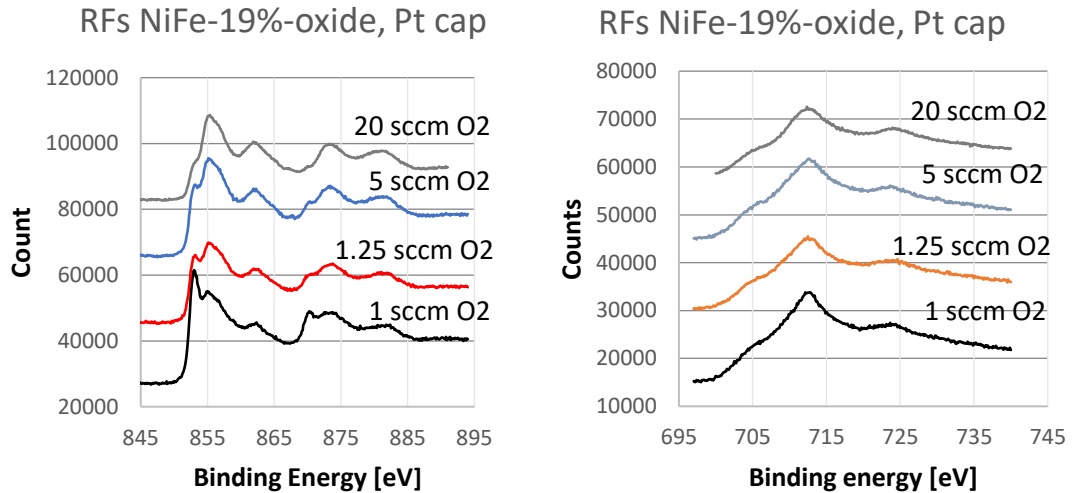


Figure 3. 8. XPS spectra of RF-sputtered NiFe-oxide samples sputtered at different oxygen flow rates covered with the Pt cap layer. Ni spectrum (left). Fe spectrum (right). Spectra are shifted in the y-direction to reveal the detail.

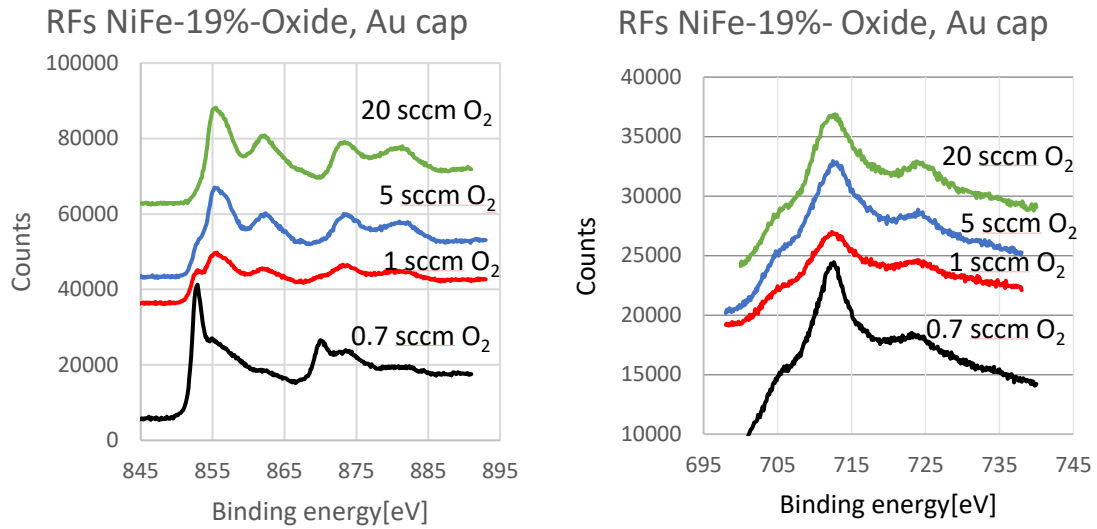


Figure 3. 9. XPS spectra of RF sputtered NiFe-Oxide samples sputtered at different oxygen flow rate covered with Au cap layer: Ni spectrum (left) and Fe spectrum (right). Spectra are shifted in the y-direction to reveal detail.

3.4 X-ray Diffractometer (XRD)

Wilhelm Röntgen was the first person who discovered X-rays while working with cathode rays coming from a vacuum tube. Later on, different people investigated different properties of X-rays. Since crystals act as diffraction gratings for X-ray wavelengths, X-ray diffraction can be utilized for the study of the crystal structure and the atomic spacing of the crystallites. The diffraction of X-ray is based on the constructive interference of EM-waves scattered from the atoms. Constructive interference is achieved for certain angles of the incident electromagnetic wave only when the interaction of X-rays and crystals satisfy Bragg's law ($2d \sin \theta = n\lambda$). A scan of the

sample through the full range of 2θ angles, allows for a determination of the d-spacing and the identification of the crystal structure and its orientation [63].

An X-ray diffractometer consists of three basic elements: An X-ray tube, a sample holder and an X-ray detector. In the X-ray tube, electrons produced from the heated cathode are accelerated by a potential difference applied between anode and cathode. The accelerated electrons that have sufficient kinetic energy upon arrival to the anode, interact with the anode and displace inner shells electrons of the material that leads to the emission of energy producing the X-ray spectra. This spectrum consists of several components, the strongest are K_α and K_β because this transition takes place from the L shell to K the shell and from the K shell to the M shell respectively. The K_α component of the X-ray spectra consists of two parts, i.e. $K_{\alpha 1}$ and $K_{\alpha 2}$. $K_{\alpha 1}$ has a slightly shorter wavelength and twice the intensity as $K_{\alpha 2}$ [64]. The X-rays are collected from the source by a collimator and directed towards the sample. The reflected X-rays are detected by a detector that is mounted on a goniometer and the intensity of the beam is recorded.

3.4.1 System Preparation and Measurement Methods

Measurements were made using a SmartLab Rigaku Diffractometer. The instrument is easy to use since it is a fully computer-controlled system with guidance software. Before any of the measurements, the water chiller is turned on. Wait time might be required for the chiller's temperature to reach 70F. Normally, this is the recommended temperature at which the XRD system is ready for operation. Next, the connected computers to the XRD system are powered up and the HyPix detector is connected. The smart lab guidance

software is started, and the X-ray generator is activated. For measurement, the voltage and the current are set to 40kV and 44mA respectively. The type of measurement is chosen and both optical and sample alignments are performed. For optical alignment, the system starts with the alignment of the source components and moves down the Xray path. For the sample alignment, the system aligns the sample parallel with the Xray beam. Center slit and height reference sample plate are usually required for the optical alignment of the setup.

Figure 3.10 shows the Rigaku X-ray Diffractometer (XRD) which was used for the measurements. After the system preparation, for the measurement with a piece of the wafer, the glass was placed between the sample and the sample stage and the sample was attached on glass with double sided tape to reduce the background noise. For each measurement with full wafer double sided tape is used to firmly attach the sample on the sample stage at four different positions. The sample stage was installed in the system in parallel beam (PB) configuration for a theta/2theta scan starting from 30 to 90 degrees.



Figure 3. 10. Rigaku X-Ray Diffractometer (XRD) at Texas State University.

3.4.2 The influence of rotation on chi, Phi and Omega to remove the substrate(silicon) peak

The rocking curve refers to the range of angles for which the sample will show a certain diffraction peak. So, for rocking curve measurements, the θ and 2θ are fixed for a certain diffraction condition, and the orientation of the sample with respect to the incident beam is varied. For example, one can rock the sample forward and backward in the ω direction as indicated in Fig.3.12 below. For a polycrystalline thin film sample, the width of the rocking curve provides a measure for the distribution of the crystallites with respect to the film normal. The wider the rocking curve the more of the crystals are oriented non-

perpendicular to the thin film. The width of the rocking curve is usually given as full width at half max. The point at which the slope of the rocking curve is greatest is the point where the intensity of the incident beam is reduced by half [65]. Here we use the rocking curve measurements to determine a measurement strategy on how to get rid of the large substrate(silicon) peak of the sample.

In order to study the influence of rotation of χ , ϕ and Ω , the $\Theta/2\theta$ scan with $\chi=0$ degree of Nickel-Iron film on a silicon substrate was done which is shown in figure 3.11. Except for the peak around 43.2 degrees, all peaks are caused by the silicon substrate. The silicon peaks are much larger than the thin film peak. Note that the penetration depth of X-rays is several microns and far exceeds the thickness of the NiFe film. As the silicon peak is so much larger than the peak of the thin film, any peak of the thin film near 70 degrees will be overshadowed by the silicon peak. It is therefore important to reduce the magnitude of the silicon peak by tilting the substrate slightly in ω , χ and ϕ to suppress the substrate peak.

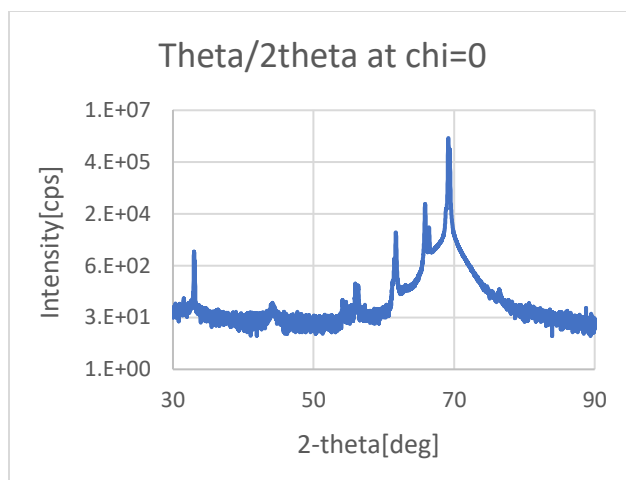


Figure 3. 11. Theta/2theta scan of the sample in the range 30-90 degrees at chi=0 degree.

To determine diffraction conditions, theta/2theta scans around the highest intensity Silicon and NiFe peaks were performed which are shown in figure 3.12. The following measurement conditions were used for both scans.

Table 3. Measurement parameters for theta/2theta measurement to determine diffraction condition.

| Scan conditions | For substrate peak | For film peak |
|----------------------|--------------------|----------------|
| Scan speed | 2.0249 deg/min | 0.0120 deg/min |
| Step size | 0.0100 deg. | 0.0100 deg |
| Incident slit | 2.00 mm | 2.00 mm |
| Length limiting slit | 5.00 mm | 5 .00 mm |
| Receiving slit#1 | Open | Open |

| | | |
|------------------|------|------|
| Receiving slit#2 | Open | Open |
|------------------|------|------|

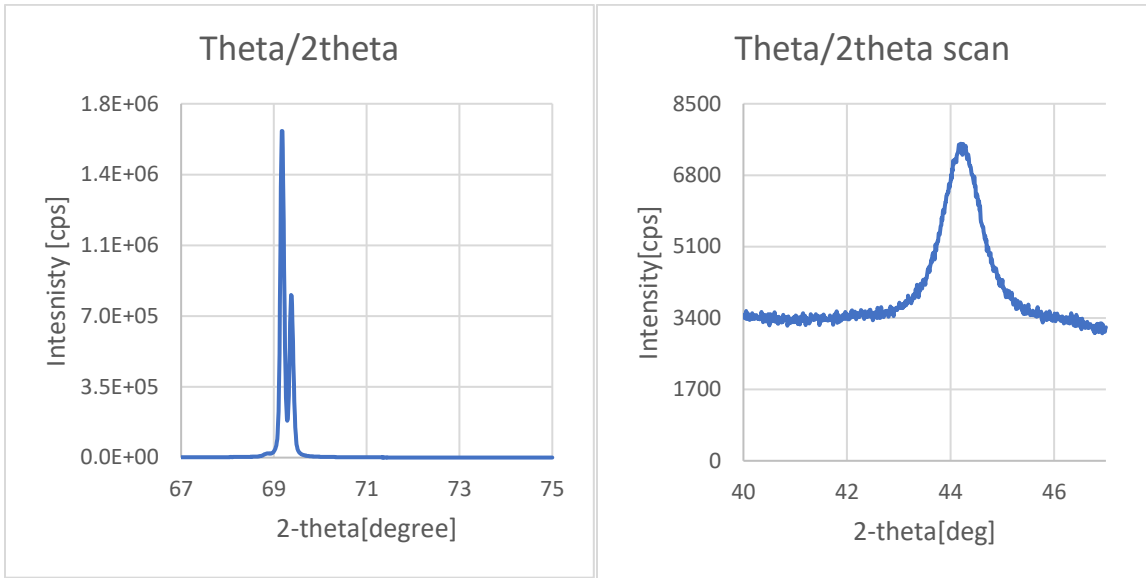


Figure 3. 12. Theta/2theta scan near highest intensity Silicon peak (69.17 degrees, left) and film peak (44.2, right).

Fig 3.13. shows the rocking curve of Omega when the θ - 2θ conditions are fixed for the silicon peak (Fig.3.13, left) and for the thin film peak at 43.3 degrees (Fig. 3.13, right) respectively. Note that a small re-orientation of around 0.5 degrees in ω will suppresses the silicon diffraction peak with more than a factor 1000. Unfortunately, such rotation will also reduce the intensity of the thin film peak at 43.2 degrees. Since silicon is single crystalline, it has a very narrow peak, so rotation was done within a small range, i.e. -0.5 to 0.5 degrees. NiFe is polycrystalline and has a wider peak. The scan range for the film peak was set in the range of -1.5 to 1.5 degrees. The following measurement conditions were used for both scans.

Table 4. Measurement parameters for omega scan.

| Scan conditions | For substrate peak | For film peak |
|----------------------|--------------------|----------------|
| Scan speed | 0.2002 deg/min | 0.0200 deg/min |
| Step size | 0.0100 deg. | 0.0100 deg |
| Incident slit | 2.00 mm | 2.00 mm |
| Length limiting slit | 5.00 mm | 5 .00 mm |
| Receiving slit#1 | Open | Open |
| Receiving slit#2 | Open | Open |

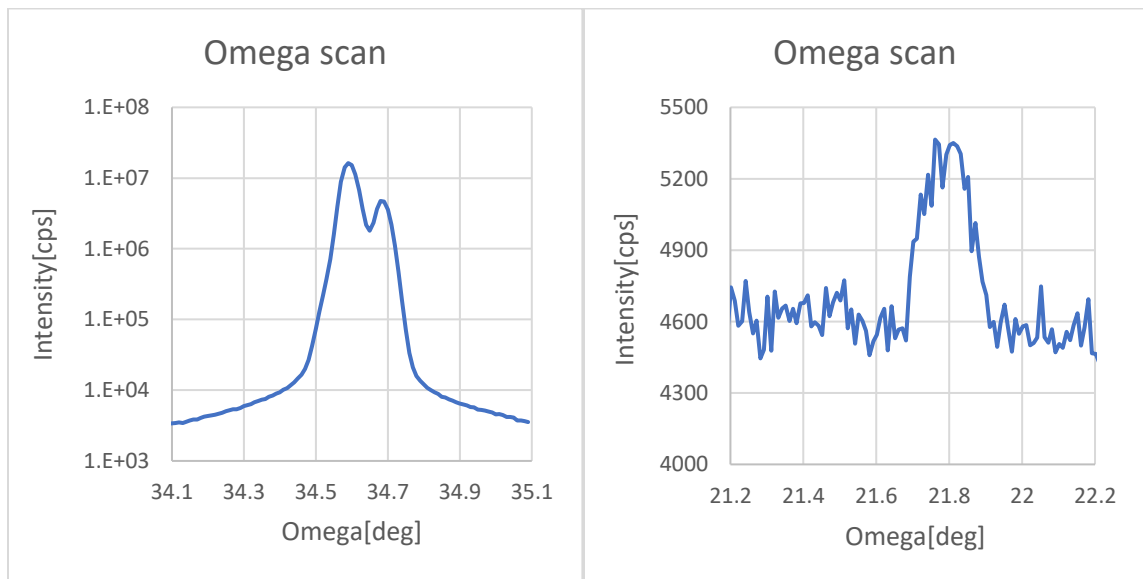


Figure 3. 13. Scan of Omega at the diffraction condition of silicon peak(left) and film peak(right).

Similarly, Fig 3.14. Shows the effect of rotation of phi for both at the diffraction condition (The measurement conditions for both scans are given in table 3) in the range of -90 to 90 degrees. In both scans, the rotation was done relative to the current position. Note that to suppress the silicon peak, one has to rotate the substrate by more than 25 degrees. Results show that scans of Omega and phi affect both silicon peak and film peak.

Table 5. Measurement parameters for phi scan.

| Scan conditions | For substrate peak | For film peak |
|----------------------|--------------------|----------------|
| Scan speed | 1.5116 deg/min | 0.6723 deg/min |
| Step size | 0.0120 deg. | 0.0120 deg |
| Incident slit | 2.00 mm | 2.00 mm |
| Length limiting slit | 5.00 mm | 5 .00 mm |
| Receiving slit#1 | Open | Open |
| Receiving slit#2 | Open | Open |

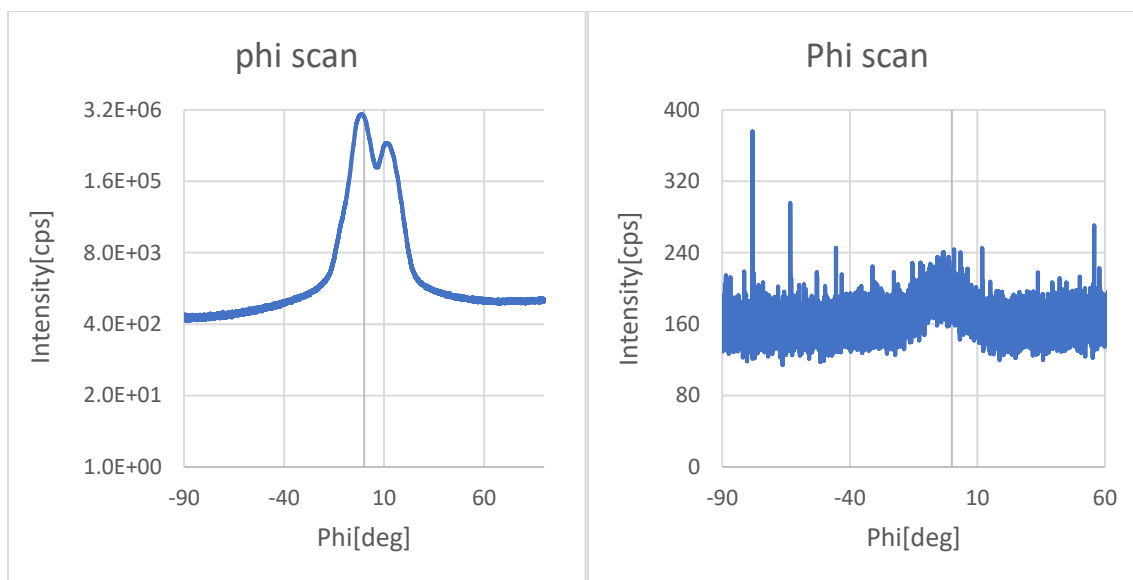


Figure 3. 14. Scan of phi at the diffraction condition of silicon(left) and film(right) in the range of -90 to 90 degrees.

Fig 3.15. shows the rocking of chi near the silicon peak (Fig.3.15, left) and near the thin film peak (Fig.3.15, right) (The following measurement conditions were used for both scans as shown in table 4). The plots show that the rotation of chi has little effect on the film peak but affects the silicon peak significantly. A change of chi with 5 degrees will suppress the silicon peak with more than a factor 10,000. The intensity of the thin film peak is little affected by this chi change. This leads to the conclusion that for these samples it is best to rotate chi rather than to rotate Omega and phi to get rid of substrate(silicon) peak without affecting the film peak. Fig 3.16(right) suggests that chi should be rotated at least by 5 degrees for complete removal of silicon peak without affecting the film peak.

Table 6. Measurement parameters for Chi scan.

| Scan conditions | For substrate peak | For film peak |
|----------------------|--------------------|----------------|
| Scan speed | 0.2002 deg/min | 0.0850 deg/min |
| Step size | 0.0100 deg. | 0.0100 deg |
| Incident slit | 2.00 mm | 0.1 mm |
| Length limiting slit | 5.00 mm | 5 .00 mm |
| Receiving slit#1 | Open | 10 mm |
| Receiving slit#2 | Open | 10 mm |

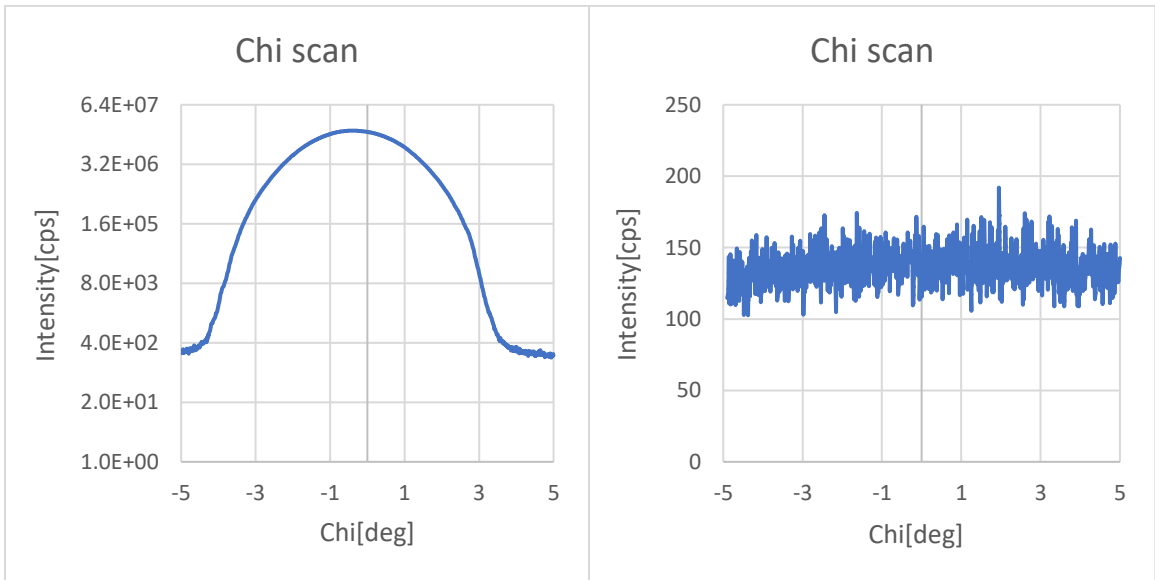


Figure 3. 15. Scans of chi at the diffraction condition of silicon peak (left) and film peak(right).

Fig.3.16. shows the theta/2theta scans for the sample at chi=0 and at chi=5 degrees. No evidence for thin-film peaks was observed behind the silicon peak.

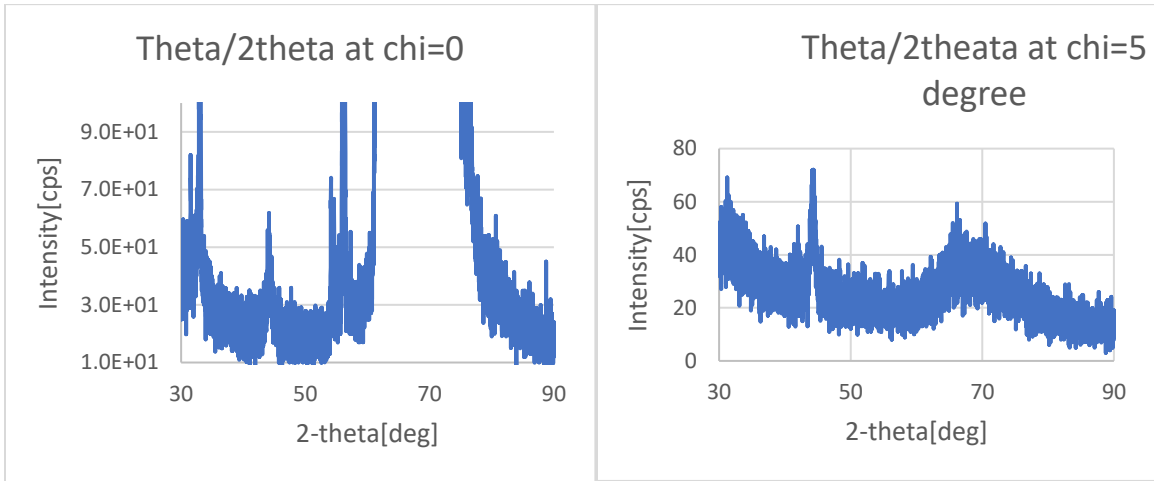


Figure 3. 16. Scan of theta/2theta of the sample at chi=0 degree (left) and chi=5 degrees (right).

3.4.3 Texture of thin films

Texture or preferred orientation is a description of the alignment of crystal grains in a thin Film. The sample in which the alignment of the crystal grains is fully random said to have no distinct texture. If the orientations of the crystal grains are not random and have some preferred orientation, then the sample has weak, moderate or strong texture [66]. The degree of preferred orientation in a thin film may range from weak fiber texture to epitaxy. Fiber-textured films are polycrystalline, with the preferred grain orientation only in the direction normal to the plane of the film. Ideal fiber texture is characterized by an

orientation distribution peak aligned with the film normal, and random grain orientation in the plane of the film [67]. Texture strength is usually defined by the volume fraction of grains with a given preferred orientation and by the angular distribution of grain orientation about a certain axis. Texture strength can vary considerably depending on the material system (film, substrate) and the deposition conditions including deposition geometry and deposition temperature [67]. The magnetic field applied during the deposition affect the texture of the magnetic thin film due to the preferential orientation of magnetic grains. The appropriate spacer layer also significantly affects the texture of the thin film.

Strongly textured films may have a majority of grains aligned within a fraction of a degree of the film normal. The remaining grains are often random in orientation, but mixed textures are also common. Driving forces for texture formation are surface energy minimization and strain energy minimization [68]. The former favors the formation of a $\{111\}$ texture, while the latter would favor a $\{100\}$ texture [69]. For face-centered cubic materials, (111) texture is generally favored. Other orientations, particularly $\{001\}$ and $\{110\}$, are also observed in these materials.

3.4.3.1 Theta-2theta Measurement

In order to find the 2θ position i.e diffraction conditions for pole figure measurement, we performed theta-2theta scan. Samples reported in this section were sputtered in a variety of methods, (a) two guns and rotating the sample holder at zero magnetic field, (b) two guns without rotating the sample holder at zero magnetic field, (c) single gun and rotating the sample holder at zero magnetic field, (d) single gun and without rotating the

sample holder at zero magnetic fields and (e) single gun and rotating the sample in magnetic field. Furthermore, some of the samples were sputtered at high gas pressure (i.e Ar 30 sccm) while others were sputtered at low gas pressure (i.e Ar 5 sccm).

Figure 3.17 shows the theta-2theta scan of $\text{Ni}_{0.81}\text{Fe}_{0.19}$ samples both at low and high Ar flow deposition process. For high Ar pressure and low thickness, samples show only (111) peak. The high pressure and high thickness samples also show (200) and (220) peaks along with (111) peak. The (220) peak seems slightly larger than (200) peak. For low pressure and high thickness, samples show two competing peaks i.e (111) and (200). It is noticed that sample sputtered in the magnetic field shows stronger texture than sputtered without the magnetic field of the same thickness. We believe that this is caused by the preferential orientation of magnetic grains. The peak at 42.3 degrees (red plot fig.3.17b) only appears in measurements done on wafer pieces and is believed to originate from the clips or the sample-holder of the X-ray system. We do not notice any significant difference in peak intensity whether the sample is sputtered using two guns or one gun and whether the deposition process was carried out rotating the sample holder with maximum speed or without rotating. But, of course, noticeable change in peak intensity of the samples can be noticed if we move from sample sputtered at high pressure to low pressure and samples sputtered in the magnetic field to at zero magnetic fields.

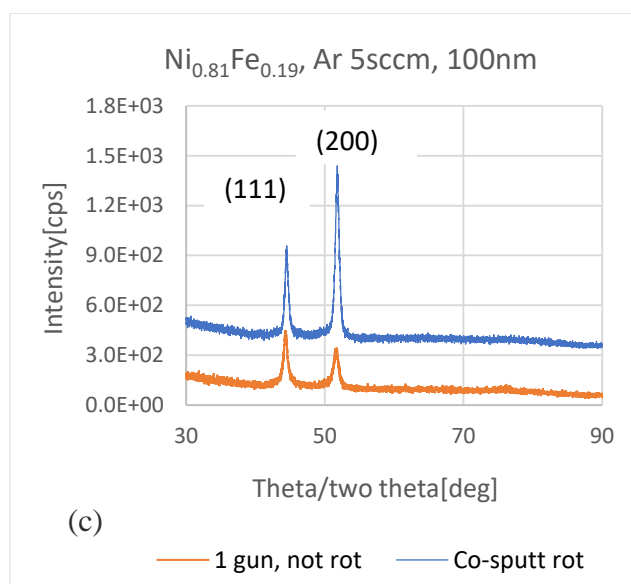
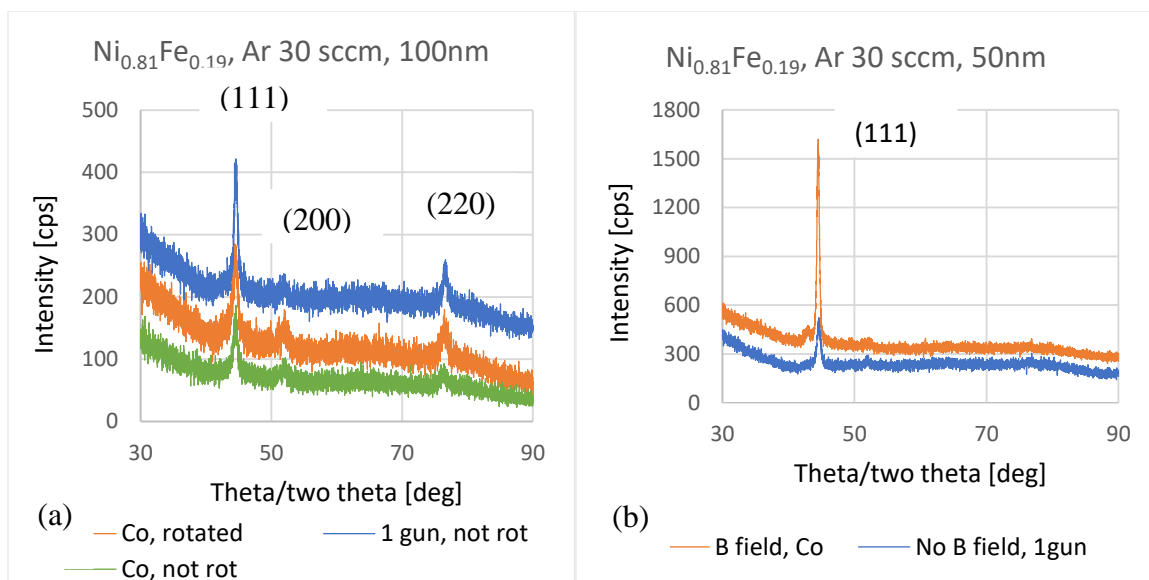


Figure 3. 17. Comparison of theta-2theta plot of $\text{Ni}_{0.81}\text{Fe}_{0.19}$ (a) high-pressure thick samples (b) high-pressure thin samples (c) low-pressure thick samples.

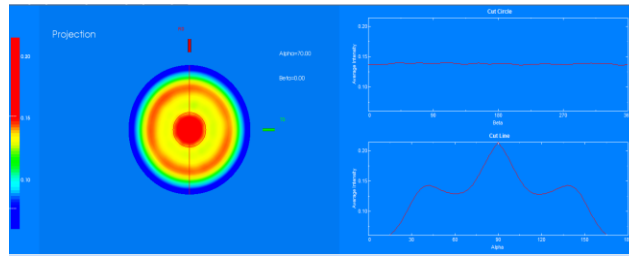
3.4.3.2 Pole Figure Measurements

A pole figure is an XRD technique to determine the texture of for example a polycrystalline film sample. For the measurement, the diffraction angle 2θ is fixed at an angle corresponding to specific d-spacing. In our case, 2θ is fixed at 44.5° , 51.8° or 76.6° corresponding to the (111), (200) or (220) peaks of $\text{Ni}_{0.81}\text{Fe}_{0.19}$. Then diffracted intensity is collected by varying two geometrical parameters α (tilt angle that is χ , from surface normal direction) and β angle (phi rotation angle around sample surface normal direction). α is scanned from 0-90 degrees and β is scanned from 0-360 degrees. Each α and β is measured with a step size of 3.00 degrees. To reduce the effect of sample size and geometry, the background signal is measured at ± 1.5 degrees and subtracted from the intensity at the diffraction condition. The obtained diffracted intensity data is plotted as a function of α and β . The most common representations of the pole figures are the stereographic or equal-area projection. The intensity of a given reflection (h, k, l) is proportional to the number of crystallites that have their Miller indices (h, k, l) parallel to the scattering vector (planes in reflecting condition (Bragg's law)). Hence, the pole figure gives the probability of finding a given crystal-plane-normal as a function of the specimen orientation.

For texture analysis, we used the pole figure analysis method of the Rigaku software. The measured data was loaded in the 3D- Explore software and analyzed by doing the first three different types of corrections- absorption, background and defocusing (which are explained in the sections below). Furthermore, the smoothing of the data and then the background subtraction was carried out. Finally, the intensity scale of pole figures was adapted to enhance its ring pattern.

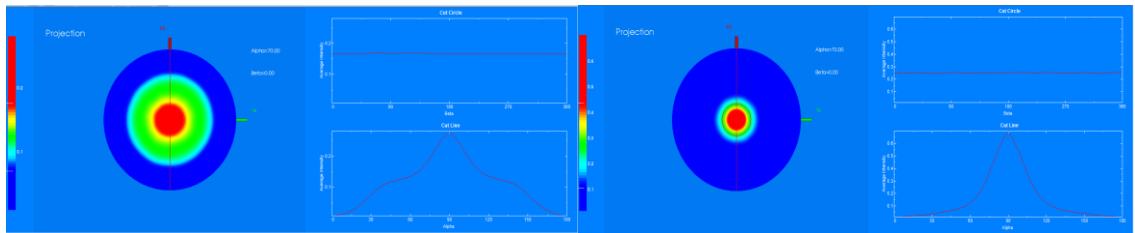
We found two competing textures i.e. (111) and (200) for films deposited at low gas pressure (i.e Ar 5 sccm). Films prepared at high gas pressure showed a dominating (111) texture (i.e Ar 30 sccm). It was further noticed that the texture of films deposited in a magnetic field is stronger than the texture of films deposited in zero magnetic fields (see figure 3.19 (b) and (c)). Similarly, thickness appears to have a significant effect on the texture of the films with thicker films have a stronger texture (fig. 3.19a) than thinner samples (figure 3.19b and fig. 3.19c) deposited under similar conditions. Figure 3.20 shows the polar plot of the Permalloy samples deposited without rotating the sample holder during deposition at low gas pressure and using a single gun. It can be noticed that both the (111) and (220) central peaks are slightly shifted toward the gun sides.

The polar plots shown in Figure 3.18 (a) and 3.20 (left) differ slightly from the rest of the plots shown below and were measured using a different measurement configuration. The polar plot shown in figure 3.18(a) and 3.20(left) were measured by using PSA 0.5 whereas the rest of the plots were measured by using PSA open. Corrected pole figures depend on measurement conditions revealing that the corrections are not complete and performing quantitative pole figure measurements on Permalloy films below 500 nm might not be meaningful at this moment. The results, however, show that the texture of Permalloy thin films is influenced by a large number of different factors including deposition angle, applied magnetic field during deposition, deposition gas pressure, and film thickness.



(111)

(a)

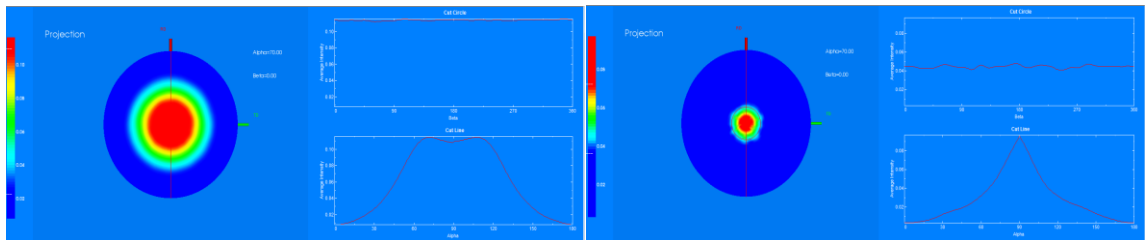


(111)

(200)

(b)

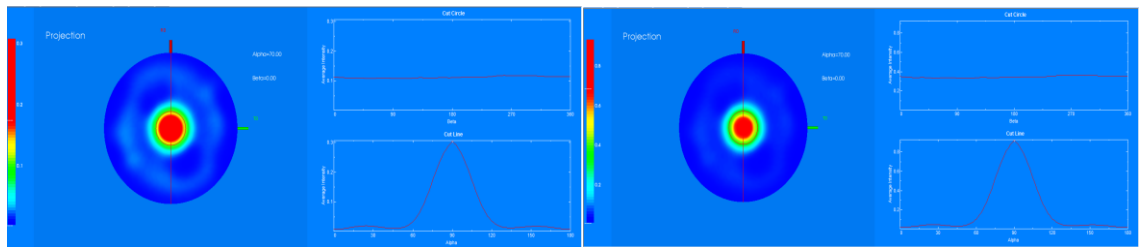
Figure 3. 18. Pole figure of $\text{Ni}_{0.81}\text{Fe}_{0.19}$ with low gas pressure, thickness 100nm, at $H=0$, (a) with PSA 0.5 and (b) with PSA Open.



(111)

(220)

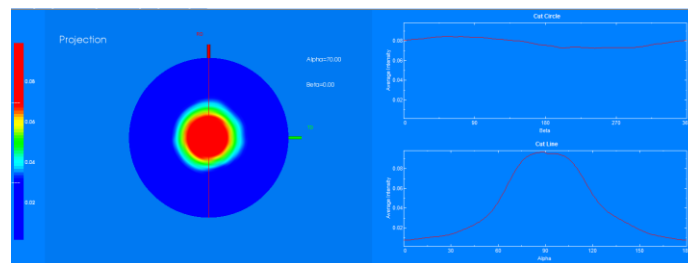
(a)



(111)

(220)

(b)



(111)

(c)

Figure 3. 19. Pole figure of $\text{Ni}_{0.81}\text{Fe}_{0.19}$ with high gas pressure measurement done by using PSA Open, (a) thickness 100 nm, at $H=0$, (b) thickness 50 nm, at $H > 0$ and (c) thickness 50 nm, at $H=0$.

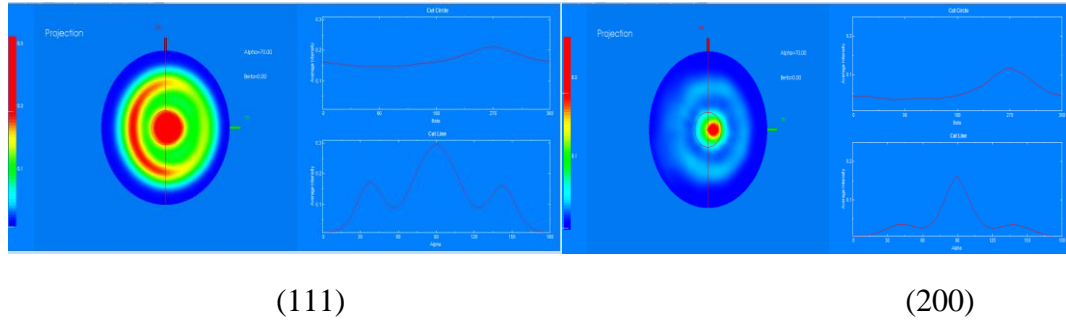


Figure 3. 20. Pole figure of $\text{Ni}_{0.81}\text{Fe}_{0.19}$ sample (thickness 100nm) sputtered without rotating the sample holder during deposition and pole figure measurement done by using PSA 0.5 (left) and PSA Open (right).

3.4.3.2.1 Absorption correction: In the case of pole figure measurements on film samples that have a thickness thinner than the penetration depth of the x-rays, the measured pole figure needs to be corrected to compensate for the θ and α dependence of the optical path length of the x-rays. As the sample is tilted through angles α , the total path length in the sample is changed because the incident X-ray reaches the substrate by transmitting through the thin film [70]. The following equation is used for the absorption correction [71]:

$$A_{\alpha} = \left[1 - \exp\left(-\frac{2\mu t}{\sin \theta \cos \alpha}\right) \right] \quad (3.1)$$

Where μ is the linear absorption factor of the layer and t is the thickness of the thin film.

3.4.3.2.2 Background correction: The signal collected during pole figure measurement, include the photons scattered from the substrate and sample holder. As for thin films, the photons diffracted by the thin film can be much smaller than the photons scattered by the substrate, it is common practice to subtract the substrate background. The background intensity during pole figure measurement must be accounted for and removed. The substrate background is typically estimated from the average of the intensity at $2\theta+1.5$ and $2\theta-1.5$ degrees. Background intensity is measured at each α angle and the intensity is subtracted from the intensity of the peak position. Note the absorption and background corrections are performed before the defocusing correction [70].

3.4.3.2.3 Defocusing correction (intensity normalization process): The broadening of the X-ray footprint on the sample surface is termed as a defocusing effect that becomes more severe at large angles α . The effect of defocusing is the broadening of the peaks because the cone of diffracted intensities broadens. As a consequence, some of the intensity is lost from the detector at large tilt angle α due to the numerical aperture of the X-ray optics. The defocusing correction enhances the intensity measured at large α . This correction compensates for the intensity lost from the detector. Since the defocusing effect depends on the 2θ position and width or size of the receiving slit and collimator, the use of the larger receiving slits remove the effect of defocusing to some extent. Larger receiving slits however decrease the angular resolution [72]. To obtain the correct interpretation of the defocusing effect, a randomly oriented powder sample must be used

as a reference. The powder sample should be measured using the same measurement conditions as the sample for a meaningful defocusing correction [70].

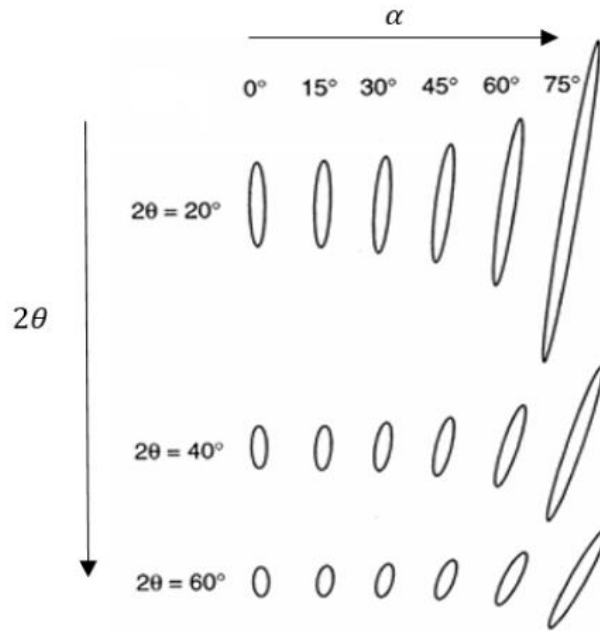


Figure 3. 21. Change in shape and orientation of irradiated footprint on the sample surface for tilt angle α and Bragg angle 2θ [73].

To prepare the defocusing correction sample, we used a custom-made defocusing calibration sample. Three calibration samples were prepared using commercial Nickel powder as a reference.

(A) Using superglue

In this technique, Ni powder was sprinkled on the clean quartz wafer and super glue was sprayed on the top of the Nickel powder to adhere the powder on the glass substrate.

Initially, we sprayed a few layers of glue which was not enough to stick the powder particles on the glass surface. Then we added more glue which made a stronger bond between the glass surface and powder particles, but we couldn't make the uniform thickness of the Ni powder on the surface of the quartz wafer. The created defocusing standard is shown in figure 3.22 below. As nonuniform thickness wafer can't be used to do pole figure measurement, we did not use this sample.



Figure 3. 22. Defocusing correction sample prepared by using superglue: showing nonuniform thickness.

(B) Using hair spray

For this technique, we sprayed a few layers of hair spray on the quartz wafer to wet the surface of the wafer. Then Ni powder was sprinkled on it. The powder was stirred with a cotton swab to make it uniform. Again, very few amounts of hair spray were sprayed to make a strong bond between Ni particles and the wafer surface. With this technique, we

were able to make a uniform Ni powder standard, but as the hair spray completely dries up, the powder starts to fall off. The sample made by this technique can't be used to do XRD measurement after twenty-four hours. A picture of the sample is shown in figure 3.23 below.



Figure 3. 23. Defocusing correction sample prepared by using hair spray.

(C) Using double-sided tape

At first, the double-sided tape was applied on the quartz wafer with great attention so that no air remains between the tape and wafer surface. Then, Nickel powder was sprinkled on the top of the tape. To make the powder film uniform, the powder was gently stirred with a cotton swab. Finally, the wafer is gently tapped on the table to remove excess powder. This procedure is the most reliable technique to make a powder sample. Fig. 3.24 shows a picture of the realized defocusing calibration sample.

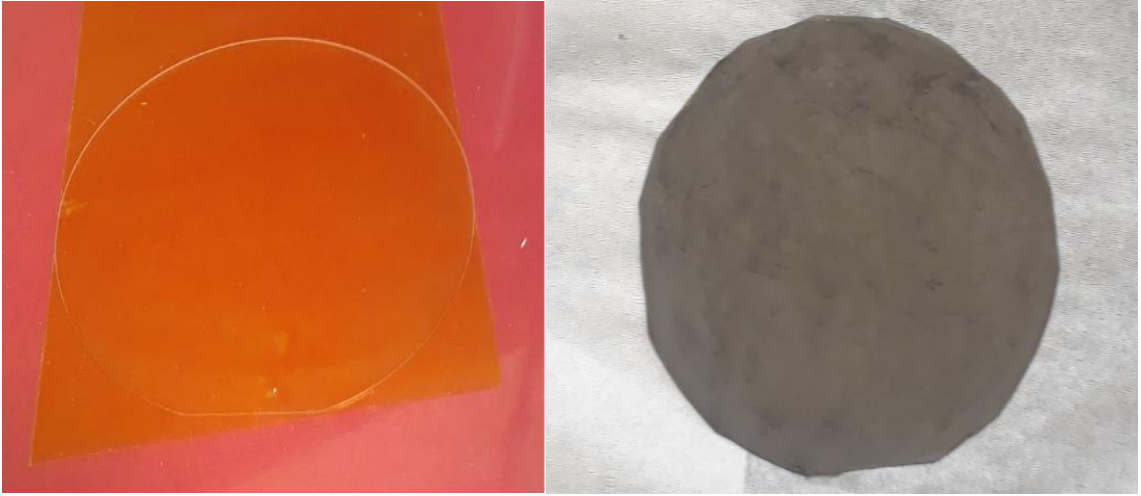


Figure 3. 24. Defocusing correction sample prepared using double-sided tape.

4 VSM MEASUREMENTS

The working principle of VSM and measurement procedures are described in chapter two. This chapter will describe the various types of measurement errors and measurement results performed with the new MicroSense VSM.

4.1 Measurement Errors in VSM

4.1.1 Effect of sweep speed and integration time in the hysteresis loop measurement

Figure 4.1(a) compares the hysteresis loops measured in sweep mode at varying sweep rates ranging from 450 Oe/s to 5000 Oe/s (blue curves) with the hysteresis loop measured in step mode (red curves). The measurements were done at time constant of 0.1 seconds. Except the hysteresis loop measured at 450 Oe/s which looks identical with the hysteresis loop measured in step mode, all other hysteresis curves measured in sweep mode look different than that measured in step mode. The coercivity values of a 3.5" floppy sample obtained from hysteresis curve measurements performed at different sweep speeds in sweep modes and different integration time in step mode are shown in table 4.1. The coercivity was determined after image correction and sweep lag correction for the curves measured in sweep mode and after image correction for the curves measured in step mode. It is noticed that the hysteresis curves measured in sweep mode yield a higher coercivity (10 Oe higher) than those measured in step mode. Furthermore, the hysteresis curves measured in sweep mode with a time constant of 0.1 sec are prone to significant

errors if the sweep speed is higher than 450 Oe/s. In addition, one can observe the considerable change in the shape of the hysteresis loop at higher sweep speeds. This is caused by the large time constant of the lock-in amplifier. The distortion of the loop shape at higher speeds can be reduced by decreasing the time constant of the lock-in amplifier as shown in figure 4.3.

The coercivities obtained from step mode measurement with two widely different integration times do not change significantly. They differ by only 2 Oe even if the measurement time is increased by a factor of four. Figure 4.2(a) shows the plot of the coercivity versus the sweep rate (blue curve) and the total measurement time versus the sweep rate (red curve). The straight blue line in figure 4.2 represents the coercivity versus time measured in step mode. It has been shown that the coercivity decreases rapidly when the applied field is swept at a higher rate than 450 Oe/s. It is believed that the hysteresis measured in step mode is closest to the true hysteresis curve and that coercivity variations of the sweep mode data are caused by imperfections of the sweep lag correction algorithm and are not caused by the physics properties of the material. From the figure below (fig.4.2b) it can be seen that the decrease in measurement time with sweep rate is not linear but decreases exponentially with the sweep rate.

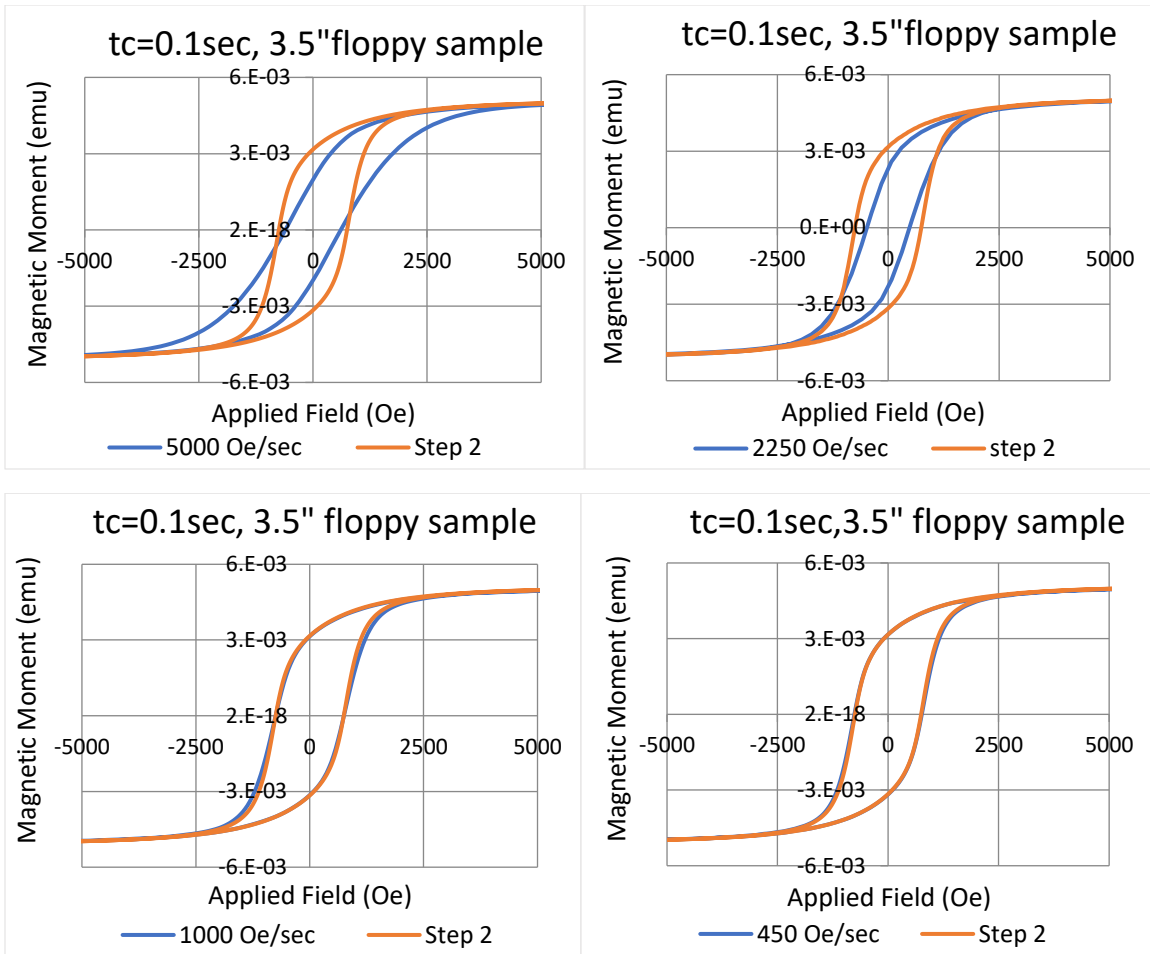


Figure 4. 1. Comparison of hysteresis loops measured at different sweep rate with the hysteresis loops measured in step mode all measured with a lock-in amplifier time constant of 0.1 seconds.

Table 7: Coercivity values at different sweep rate in sweep mode and step mode.

| Sweep rate (Oe/sec) | H _c ascending (Oe) | H _c descending (Oe) | Time for data collection (hr:min:sec) |
|------------------------|-------------------------------|--------------------------------|---|
| 5000 | 612.76 | 607.29 | 0:33 |

| | | | |
|--|--------|--------|---------|
| 2250 | 704.90 | 704.66 | 0:53 |
| 1000 | 750.70 | 747.60 | 1:37 |
| 450 | 762.00 | 761.29 | 3:14 |
| 200 | 763.86 | 762.51 | 6:56 |
| 100 | 761.17 | 759.83 | 13:36 |
| Step Mode (averaging 1 measurement) | 749.24 | 749.38 | 22:18 |
| Step Mode (averaging 100 measurements) | 747.58 | 747.48 | 1:20:57 |

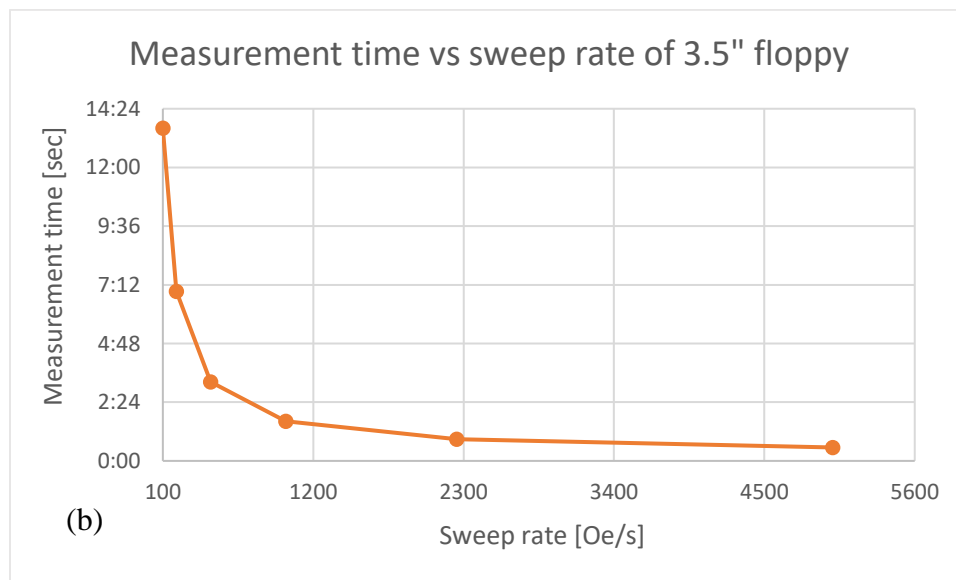
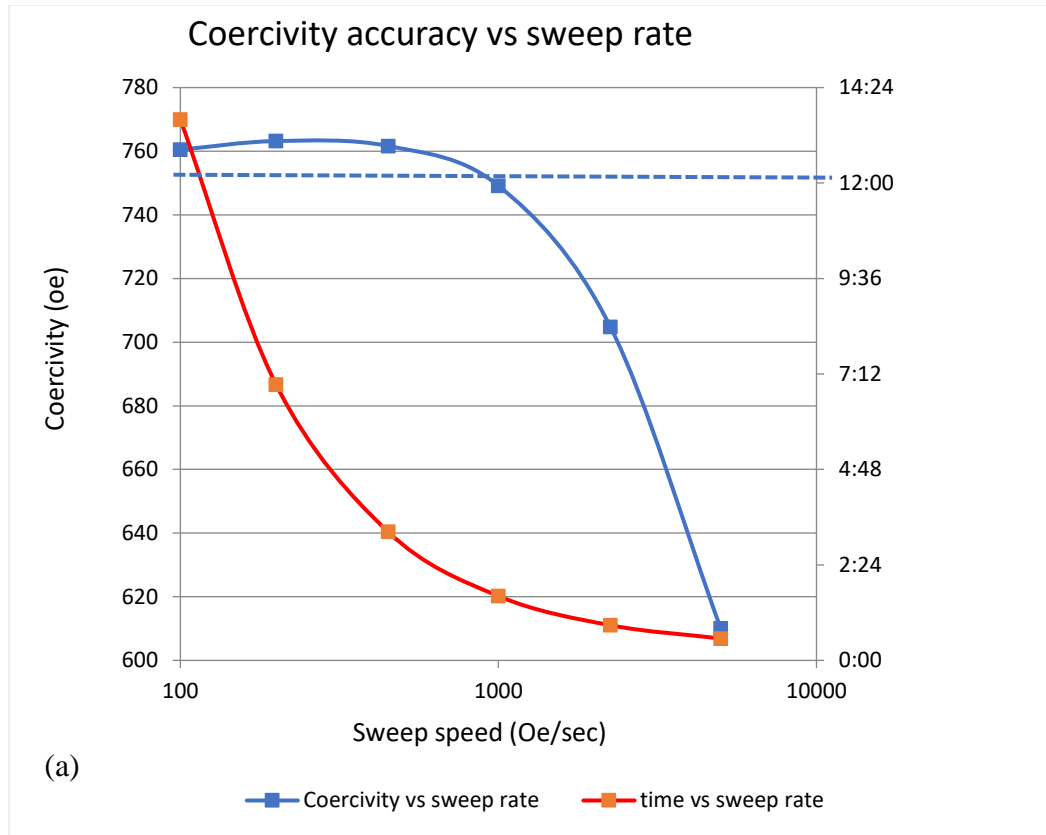
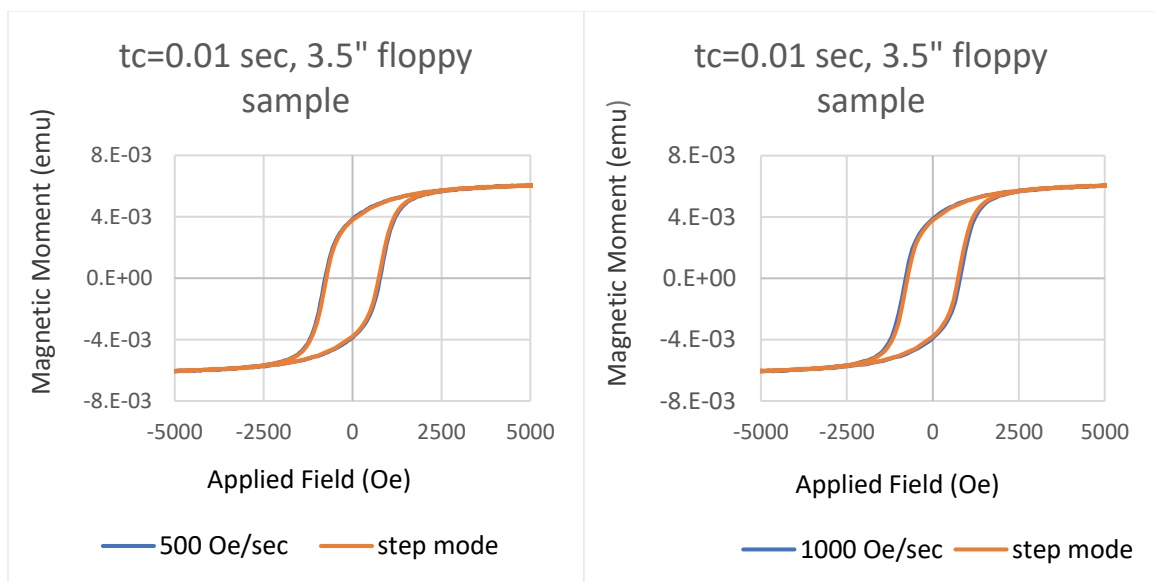


Figure 4. 2. (a) Variation of coercivity with sweep rate (blue) and measurement time with sweep rate (red) in a semi-log graph (top); (b) variation of measurement time with sweep rate in a linear graph (bottom).

The figure 4.3 below shows the comparison of the hysteresis loops of a 3.5" circular floppy sample measured in sweep mode at varying sweep rates ranging from 500 Oe/s to 5000 Oe/s (blue curves) with the hysteresis loop measured in step mode (red curves) for measurements done with a lock-in amplifier time constant of 0.01 seconds. From the hysteresis loops, one can see that now the coercivity increases with sweep speed. This suggests that with a smaller time constant, one can measure the hysteresis loop at higher speeds without distortion of their shape. Note that these measurements performed at a small-time constant contain more noise. Therefore, there is a trade-off between the accuracy of the shape of the hysteresis curve and the presence of noise. The hysteresis loop measured at 500 Oe/sec looks identical with the hysteresis loop measured in step mode. Hysteresis loops measured at higher field sweep rate look slightly different from the hysteresis curves measured in step mode and appear to have a larger coercivity. This could be caused by the magnetic viscosity of the sample[74] [75].



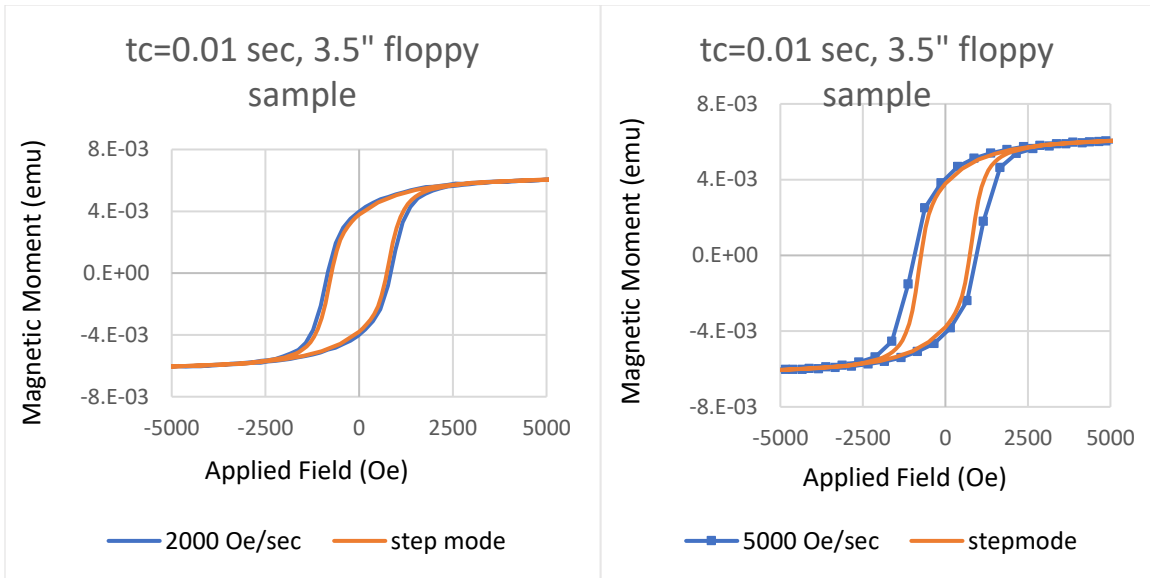


Figure 4. 3. Comparison of hysteresis loops measured at different sweep rate with the hysteresis loops measured in step mode at time constant of 0.01 seconds.

4.1.2 Effect of the shape of the sample on the angular dependence of the measured saturation magnetic moment

The influence of an asymmetric sample is shown below in figure 4.4. This was a floppy sample that was cut with a scissor and was asymmetric. The size of the sample was measured with a Hirox RH-2000 digital optical microscope and appeared to be equal to $3.44 \times 4.11 \text{ mm}^2$. The surface area determined with the Hirox polygon measurement tool and was approximately 14.37 mm^2 . The angular VSM measurements were made after each other, and after each angle change, the sample was first re-positioned by hand to minimize the X-signal versus x-position and maximize the X-signal versus y-position, and maximize the X-signal versus z-position. As one can see from figure 4.4, there is a

+/-5E-5 emu (+/-1%) variation in measured saturation magnetic moment for curves measured at different field angles. Note that since the position of the sample was adjusted prior to each measurement the sample is at exactly the same position for each measurement. Since the sample is isotropic it is expected that the observed angular variation of the measured m_s is solely due to the angular dependence of the x-coil sensitivity caused by the asymmetric shape of the sample. The difference between the m_s values measured at 180, and 360 could be partly due by the fact that the sample was more like a trapezoid than a rectangle. Note that the sample shape causes an α and 2α angular sensitivity variation that is not caused by the crystal anisotropy of the sample. A slight difference was observed at $\alpha=0$ and $\alpha=360$ degrees. This difference could also be caused by angle errors caused by slack in the belt of the step motor that controls the field-angle (angle control was done without friction correction) or more likely by errors made when centering the sample. In particular the y-position position control shows a lot of mechanical hysteresis which makes the exact adjustment difficult.

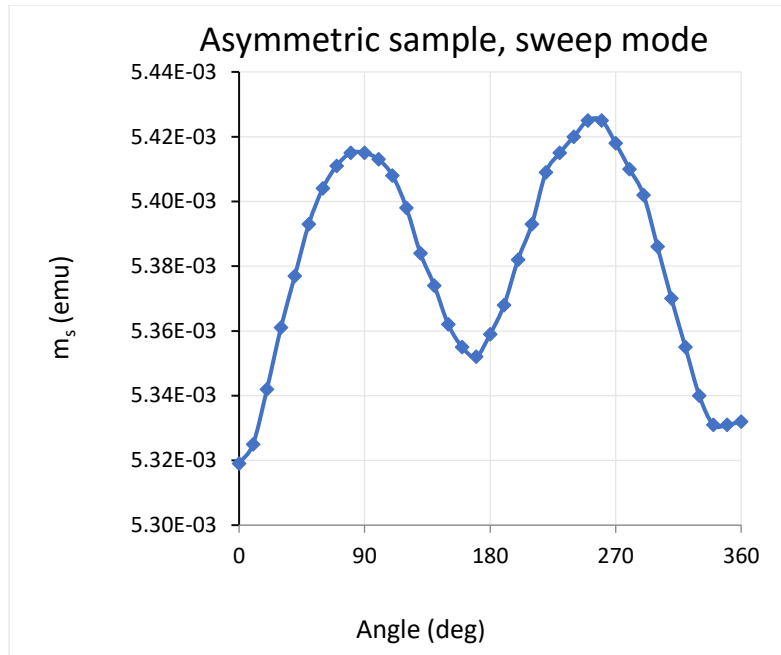


Figure 4. 4. Spread of measured saturation magnetic moment of an asymmetric 3.5” floppy sample with a trapezoid shape as a function of the field angle.

Samples should preferably be circular so rotating them does not change the sensitivity of the instrument. Figure 4.5 below shows the spread of the magnetic moment of the sample versus the field-angle for a circular 3.5-inch floppy sample (4.7+/-0.05 mm diameter) that was cut with a hole punch. The diameter was measured with the above-mentioned optical microscope. The surface area determined with the circular measurement tool of the optical microscope was approximately 17.19 mm². The VSM measurements were also made by hand, so after each angle change, the x-signal was minimized by adjusting the x-position and maximized by adjusting the y-position. For this and the following measurements, the z-position of the sample-rod was no longer adjusted. The variation is

$\pm 4.5 \times 10^{-6}$ emu ($\pm 0.1\%$) of m_s . These measurements were made in step mode averaging 50 measurements.

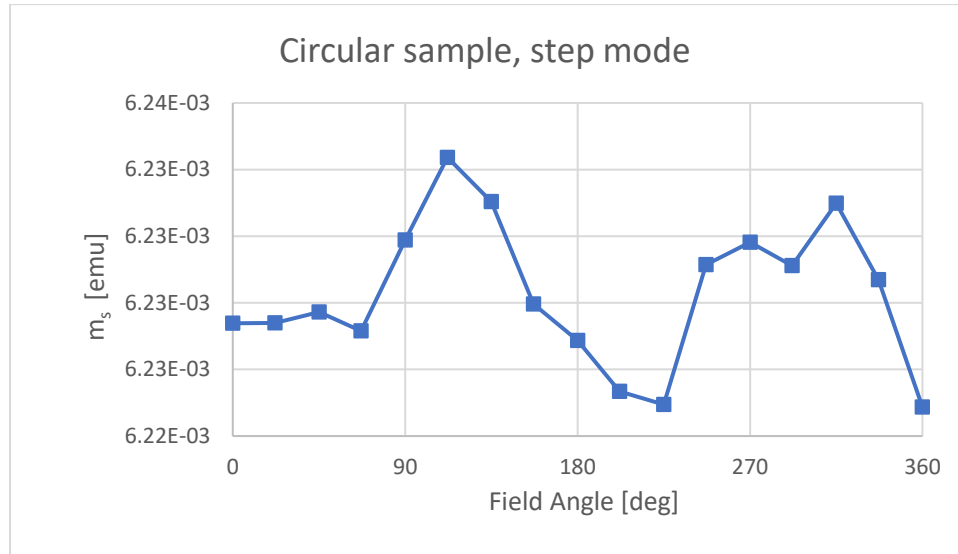


Figure 4. 5. Spread of measured saturation magnetic moment of a circular 3.5” floppy sample versus field angle.

4.1.3 Effect of the sample position on the measured saturation magnetic moment

Figure 4.6 shows the spread of the measured saturation magnetic moment for a circular 3.5-inch floppy sample (4.7 mm diameter) that was cut with a hole punch. For these measurements, the sample was aligned only at 180 degrees i.e. minimized the m_x signal by adjusting the x position and maximized the m_x signal by adjusting the y-position at a field angle of 180 degrees. There is a variation of $\pm 9 \times 10^{-5}$ emu ($\pm 1.4\%$) for the m_s determined from the hysteresis curves measured at different field angles which is significantly larger than the asymmetric sample shown in figure 4.1. We believe that this

variation is caused by a wobble of the sample rotation mechanism. This wobble causes the exact position of the sample to depend on the angle and affects both the sensitivity and the cross talk [76].

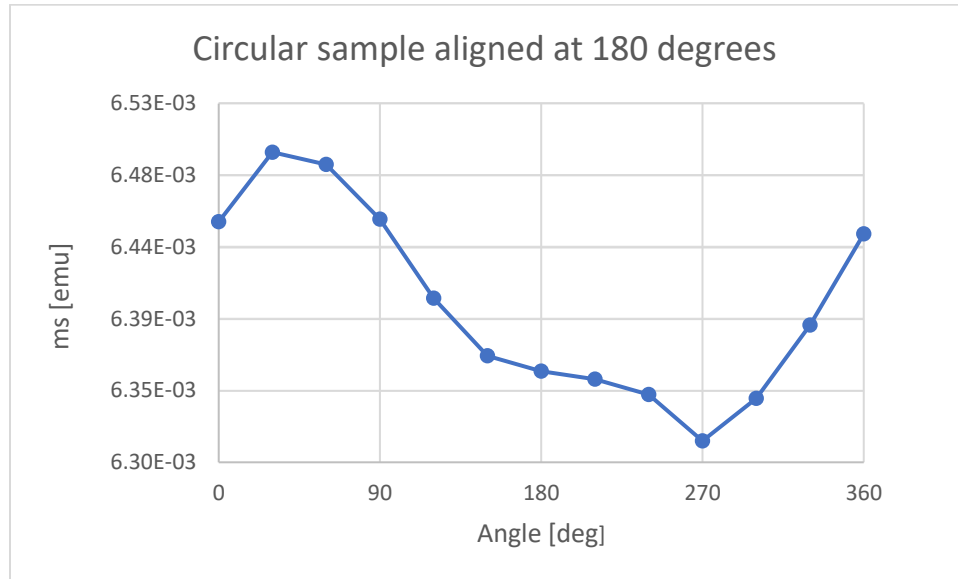
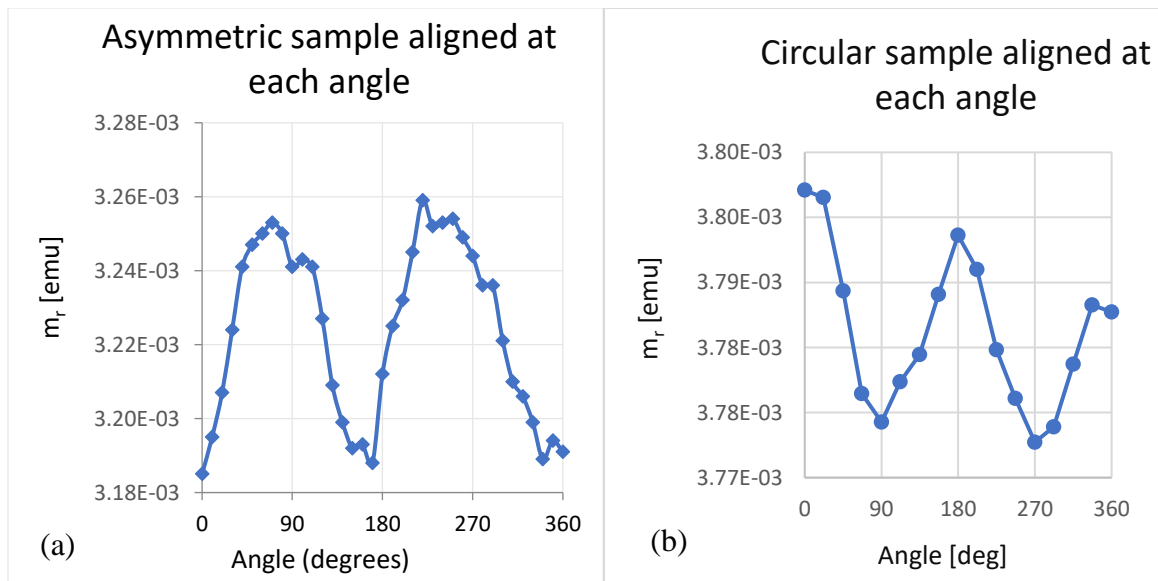


Figure 4. 6. Variation of the measured magnetic moment as a function of field angle in the 3.5” floppy sample which is aligned at 180 degrees before the first measurement.

4.1.4 Effect of shape and sample position on the measured remanent magnetic moment

Figure 4.7 shows the angular dependence of the m_r for the samples reported on in the previous section. As a floppy is isotropic, we expect a very small spread of the measured remanent magnetic moment with the angle. Similar to the case as for the angular dependence of the m_s , the sample’s asymmetry (figure 4.7(a)) and the variation of the

sample's position with respect to the pick up coils as a function of the field angle (figure 4.7(b)) also have an effect on the measured remanent magnetic moment. The largest angular variation of $\pm 7 \times 10^{-5}$ emu ($\pm 1.8\%$) is measured for the circular sample that is only aligned at 180 degrees (figure 4.7 (c)). The smallest variation of m_r , i.e. $\pm 1 \times 10^{-5}$ emu ($\pm 0.3\%$), was observed for the symmetric sample that was aligned after each field angle change (figure 4.7 (b)). The asymmetric sample that was aligned after each position showed a spread of $\pm 4 \times 10^{-5}$ emu ($\pm 1.2\%$) (figure 4.7 (a)), somewhere in between the two. When the sample is aligned at each angle, the position of the sample is the same for all measurements and a smaller angular variation of m_r is observed. On the other hand, if the sample is aligned at only one angle, the position of the sample varies with the field angle. Since the sensitivity of the system varies with sample position a larger variation with field angle is expected. This results in a large angular error shown in Fig. 4.7(c). Note that these values are larger than the angular dependence of the m_s . At the moment it is not clear what causes this. This could indicate that the sample is not perfectly isotropic.



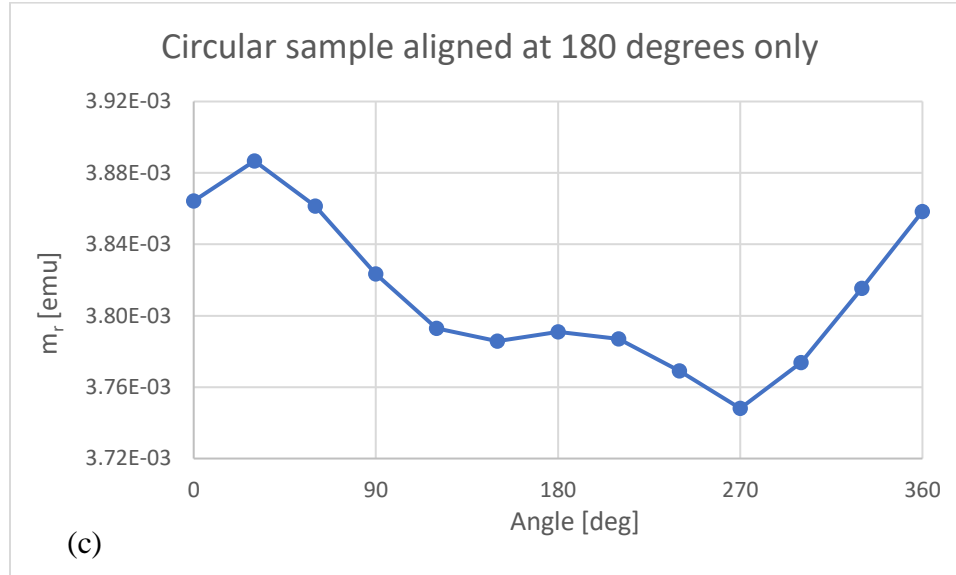


Figure 4. 7. Angle-dependence of measured remanent magnetic moment of asymmetric sample aligned at each angle (a), of circular sample aligned at each angle (b) and of circular sample aligned at 180 degrees only (c).

4.1.5 Angle dependence of coercivity of a circular floppy sample

The figure below (fig. 4.8) shows the angle-dependent coercivity of a circular 3.5” floppy sample. The measurements were done in step mode averaging 50 measurements. The sample was realigned after each angle position by minimizing the m_x signal by adjusting the x-position of the sample and by maximizing the m_x -signal by adjusting the y-position of the sample. Since the sample is isotropic and aligned at each angle position, we expect that cross-talk has no effect on the angular-background. As the sample is perfectly circular, the shape of the sample also does not have any effect on the variation of the coercivity. There is a spread of 16 Oe in H_c which is at least a factor 10 larger than the typical spread in H_c when measuring the same sample multiple times. Although currently it is not clear what causes this angular variation, it might be caused by the cross-talk as we aligned the sample based on the sensitivity not on the cross-talk. Note that the origin of the cross-talk which is determined by the exact position of the y-coils is different from the sensitivity origin which is determined by the exact positions of the x-coils. Both coordinate systems can even be slightly rotated with respect to each other.

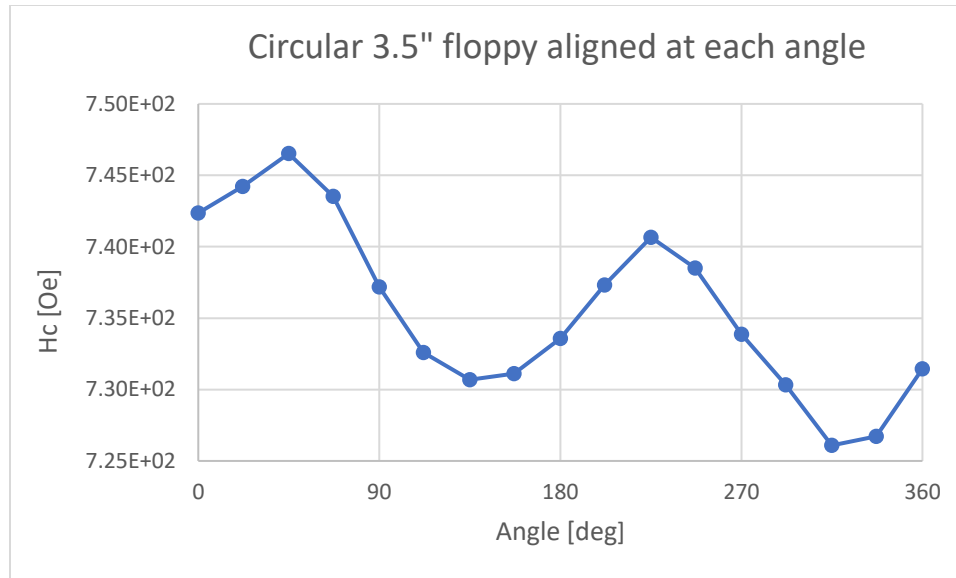


Figure 4. 8. Angular dependence of coercivity of circular 3.5 “floppy sample.

4.1.6 Derivation of sensitivity function and cross talk

As discussed in the previous sections, that hysteresis curve varies as a function of the field angle. This angle dependence can be caused by three different effects: (a) the crystal or shape anisotropy of the sample; (b) the asymmetric shape of the sample; (c) a small angle dependence of the position of the sample caused by concentricity issues of the sample-rod-sample system. Since the sensitivity of the VSM depends on the exact position of the sample the (b) and (c) introduce an angular-background signal that is not caused by the sample. In order to get a better understanding of these instrument issues, in this section expression for the sensitivity function will be derived.

Let us consider the magnetic stray field of a magnetic point dipole \mathbf{m} [77] as follows:

$$\vec{B} = \frac{\mu_0}{4\pi} \frac{1}{r^3} \{3(\vec{m} \cdot \hat{r})\hat{r} - \vec{m}\} \quad (4.1.6.1)$$

Where $\vec{r} = (x-x', y-y', z-z')$ with (x,y,z) the field point and (x', y', z') the position of the sample.

$$\hat{r} = \frac{(x-x')\hat{i} + (y-y')\hat{j} + (z-z')\hat{k}}{\sqrt{(x-x')^2 + (y-y')^2 + (z-z')^2}} \quad (4.1.6.2)$$

Let us assume

$\vec{m} = m \hat{i}$, so, the dipole moment is oriented in the positive x-direction:

$$\vec{B}_x = \frac{\mu_0}{4\pi} \frac{3m\hat{i} \cdot [(x-x')\hat{i} + (y-y')\hat{j} + (z-z')\hat{k}]\hat{r} - m\hat{i}}{\{(x-x')^2 + (y-y')^2 + (z-z')^2\}^{\frac{3}{2}}} \quad (4.1.6.3)$$

$$\vec{B}_x = \frac{\mu_0}{4\pi} \frac{3m(x-x')[(x-x')\hat{i} + (y-y')\hat{j} + (z-z')\hat{k}]}{r^5} - \frac{m\hat{i}}{r^3} \quad (4.1.6.4)$$

$$B_{xx} = \frac{\mu_0}{4\pi} \frac{[3m(x-x')^2 - m\{(x-x')^2 + (y-y')^2 + (z-z')^2\}]}{[(x-x')^2 + (y-y')^2 + (z-z')^2]^{\frac{5}{2}}} \quad (4.1.6.5)$$

$$= \frac{3\mu_0 m}{4\pi} \frac{[(x-x')^2 - \frac{1}{3}\{(x-x')^2 + (y-y')^2 + (z-z')^2\}]}{[(x-x')^2 + (y-y')^2 + (z-z')^2]^{\frac{5}{2}}} \quad (4.1.6.6)$$

Where B_{xx} is the magnetic field in the positive x-direction at the field point (x,y,z) caused by a magnetic dipole at the (x',y', z') pointing in the positive x-direction. This expression is in agreement with Gregory's expression [78] for $x'=y'=z'=0$ i.e the sample at the origin.

Now assume the magnetic dipole is oriented in the positive y-direction so $\vec{m} = m\hat{j}$

$$\vec{B}_y = \frac{\mu_0 3m\hat{j} \cdot [(x-x')\hat{i} + (y-y')\hat{j} + (z-z')\hat{k}]\hat{r} - m\hat{j}}{4\pi \{(x-x')^2 + (y-y')^2 + (z-z')^2\}^{\frac{3}{2}}} \quad (4.1.6.7)$$

$$= \frac{\mu_0 3m (y-y')[(x-x')\hat{i} + (y-y')\hat{j} + (z-z')\hat{k}]}{4\pi r^5} - \frac{m\hat{j}}{r^3} \quad (4.1.6.8)$$

$$B_{xy} = \frac{\mu_0 3m(y-y')(x-x')}{4\pi [(x-x')^2 + (y-y')^2 + (z-z')^2]^{\frac{5}{2}}} \quad (4.1.6.9)$$

Where B_{xy} is the magnetic field in the x-direction at the field point (x,y,z) caused by a magnetic dipole positioned at (x',y', z') pointing in the positive y-direction.

And for the magnetic dipole oriented in the positive z-direction, i.e. $\vec{m} = m\hat{k}$ we find:

$$\vec{B}_z = \frac{\mu_0 3m\hat{k} \cdot [(x-x')\hat{i} + (y-y')\hat{j} + (z-z')\hat{k}]\hat{r} - m\hat{k}}{4\pi \{(x-x')^2 + (y-y')^2 + (z-z')^2\}^{\frac{3}{2}}} \quad (4.1.6.10)$$

$$= \frac{\mu_0 3m (z-z')[(x-x')\hat{i} + (y-y')\hat{j} + (z-z')\hat{k}]}{4\pi r^5} - \frac{m\hat{k}}{r^3} \quad (4.1.6.11)$$

$$B_{xz} = \frac{\mu_0 3m(z-z')(x-x')}{4\pi [(x-x')^2 + (y-y')^2 + (z-z')^2]^{\frac{5}{2}}} \quad (4.1.6.12)$$

Where B_{xz} is the magnetic field in the x-direction at the field point (x,y,z) caused by a magnetic dipole positioned at (x',y',z') pointing in the positive z-direction.

Let us assume perfect alignment in z-direction so,

$$z' = \alpha \sin(\omega t) \quad (4.1.6.13)$$

where α is vibrational amplitude and ω is the angular vibrational frequency. Including this information in the equations (4.6.6), (4.6.9) and (4.6.12) and multiplying these equations by the surface area (A) of the coils and the number of windings (N) will get us the coupled flux through a single pick-up coil.

That is

$$\Phi_{xx} = NAB_{xx} \quad (4.1.6.14)$$

$$= \frac{NA3\mu_0 m \left[(x - x')^2 - \frac{1}{3} \{ (x - x')^2 + (y - y')^2 + (z - \alpha \sin(\omega t))^2 \} \right]}{4\pi [(x - x')^2 + (y - y')^2 + (z - \alpha \sin(\omega t))^2]^{\frac{5}{2}}} \quad (4.1.6.15)$$

$$\Phi_{xy} = NAB_{xy} = \frac{NA\mu_0}{4\pi} \frac{3m(y - y')(x - x')}{[(x - x')^2 + (y - y')^2 + (z - \alpha \sin(\omega t))^2]^{\frac{5}{2}}} \quad (4.1.6.16)$$

$$\Phi_{xz} = NAB_{xz} = \frac{NA\mu_0}{4\pi} \frac{3m(z - \alpha \sin(\omega t))(x - x')}{[(x - x')^2 + (y - y')^2 + (z - \alpha \sin(\omega t))^2]^{\frac{5}{2}}} \quad (4.1.6.17)$$

The induced voltage is proportional to change in magnetic flux with respect to time, so for the xx term (let's forget about proportionality constant)

$$\frac{\partial \Phi_{xx}}{\partial t} = \frac{\partial}{\partial t} \left\{ \frac{\left[(x - x')^2 - \frac{1}{3} \{ (x - x')^2 + (y - y')^2 + (z - \alpha \sin(\omega t))^2 \} \right]}{[(x - x')^2 + (y - y')^2 + (z - \alpha \sin(\omega t))^2]^{\frac{5}{2}}} \right\} \quad (4.1.6.18)$$

$$= \frac{\partial}{\partial t} \left\{ \frac{\left[\frac{2}{3} (x - x')^2 - \frac{1}{3} (y - y')^2 - \frac{1}{3} (z - \alpha \sin(\omega t))^2 \right]}{[(x - x')^2 + (y - y')^2 + (z - \alpha \sin(\omega t))^2]^{\frac{5}{2}}} \right\} \quad (4.1.6.19)$$

$$= \frac{\frac{2}{3} (z - \alpha \sin(\omega t)) \alpha \omega \cos(\omega t)}{[(x - x')^2 + (y - y')^2 + (z - \alpha \sin(\omega t))^2]^{\frac{5}{2}}} \quad (4.1.6.20)$$

$$+ \left\{ \frac{2}{3}(x - x')^2 - \frac{1}{3}(y - y')^2 - \frac{1}{3}(z - \alpha \sin(\omega t))^2 \right\} \left(\frac{5}{2} \right)$$

$$\{(x - x')^2 + (y - y')^2 + (z - \alpha \sin(\omega t))^2\}^{-\frac{7}{2}} \{2(z - \alpha \sin(\omega t))\alpha\omega \cos(\omega t)\}$$

$$= \left(\frac{1}{3} \right) \frac{2(z - \alpha \sin(\omega t))\alpha\omega \cos(\omega t)}{[(x - x')^2 + (y - y')^2 + (z - \alpha \sin(\omega t))^2]^{\frac{5}{2}}} \quad (4.1.6.21)$$

$$+ \frac{5\{2(x - x')^2 - (y - y')^2 - (z - \alpha \sin(\omega t))^2\}(z - \alpha \sin(\omega t))\alpha\omega \cos(\omega t)}{\{(x - x')^2 + (y - y')^2 + (z - \alpha \sin(\omega t))^2\}^{\frac{7}{2}}} \left(\frac{1}{3} \right)$$

$$= \frac{1}{3} \left\{ 2 + \frac{5\{2(x - x')^2 - (y - y')^2 - (z - \alpha \sin(\omega t))^2\}}{(x - x')^2 + (y - y')^2 + (z - \alpha \sin(\omega t))^2} \right\}$$

$$\frac{(z - \alpha \sin(\omega t))\alpha\omega \cos(\omega t)}{[(x - x')^2 + (y - y')^2 + (z - \alpha \sin(\omega t))^2]^{\frac{5}{2}}} \quad (4.1.6.22)$$

$$= \left\{ \frac{12(x - x')^2 - 3(y - y')^2 - 3(z - \alpha \sin(\omega t))^2}{(x - x')^2 + (y - y')^2 + (z - \alpha \sin(\omega t))^2} \right\}$$

$$\frac{(z - \alpha \sin(\omega t))\alpha\omega \cos(\omega t)}{[(x - x')^2 + (y - y')^2 + (z - \alpha \sin(\omega t))^2]^{\frac{5}{2}}} \left(\frac{1}{3} \right)$$

$$= \frac{(4(x - x')^2 - (y - y')^2 - (z - z')^2)(z - \alpha \sin(\omega t))\alpha\omega \cos(\omega t)}{[(x - x')^2 + (y - y')^2 + (z - \alpha \sin(\omega t))^2]^{\frac{7}{2}}} \quad (4.1.6.23)$$

Since α is very small compared to z , the $z - \alpha \sin(\omega t)$ terms are approximately equivalent to z , so

$$V_{xx} \sim \left\{ \frac{z \alpha \omega \cos(\omega t) (4(x-x')^2 - (y-y')^2 - z^2)}{[(x-x')^2 + (y-y')^2 + z^2]^{\frac{7}{2}}} \right\} \quad (4.1.6.24)$$

The lock-in sees (with proportionality constant terms)

$$S_{xx} = \frac{V_{xx}}{m_x} = \left(\frac{AN3\mu_0}{4\pi} \right) \left\{ \frac{z \alpha \omega (4(x-x')^2 - (y-y')^2 - z^2)}{[(x-x')^2 + (y-y')^2 + z^2]^{\frac{7}{2}}} \right\} \quad (4.1.6.25)$$

For xy terms:

$$\frac{\partial \Phi_{xy}}{\partial t} = \frac{3NmA\mu_0}{4\pi} \frac{(y-y')(x-x') \frac{5}{2} (2(z - \alpha \sin(\omega t)) \alpha \omega \cos(\omega t))}{\{(x-x')^2 + (y-y')^2 + (z - \alpha \sin(\omega t))^2\}^{\frac{7}{2}}} \quad (4.1.6.26)$$

Assuming $z - \alpha \sin(\omega t) \sim z$

$$= \frac{3Nm5A\mu_0}{4\pi} \frac{(y-y')(x-x') z \alpha \omega \cos(\omega t)}{\{(x-x')^2 + (y-y')^2 + z^2\}^{\frac{7}{2}}} \quad (4.1.6.27)$$

The lock-in sees

$$S_{xy} = \frac{V_{xy}}{m_y} = \frac{3N5A\mu_0}{4\pi} \frac{(y-y')(x-x') z \alpha \omega}{\{(x-x')^2 + (y-y')^2 + z^2\}^{\frac{7}{2}}} \quad (4.1.6.28)$$

For xz term, let's forget the proportionality constant

$$\begin{aligned} \frac{\partial \Phi_{xz}}{\partial t} &= \frac{(x-x')(\alpha \sin(\omega t)) \alpha \omega \cos(\omega t)}{[(x-x')^2 + (y-y')^2 + (z - \alpha \sin(\omega t))^2]^{\frac{5}{2}}} + \\ &\frac{(x-x')(z - \alpha \sin(\omega t)) \left(-\frac{5}{2}\right) \{2(z - \alpha \sin(\omega t)) \alpha \omega \cos(\omega t)\}}{\{(x-x')^2 + (y-y')^2 + (z - \alpha \sin(\omega t))^2\}^{\frac{7}{2}}} \end{aligned} \quad (4.1.6.29)$$

$$\begin{aligned}
&= \frac{(x - x')\alpha\omega \cos(\omega t)}{[(x - x')^2 + (y - y')^2 + (z - \alpha \sin(\omega t))^2]^{\frac{5}{2}}} \\
&\left\{ 1 - \frac{5(z - \alpha \sin(\omega t))^2}{(x - x')^2 + (y - y')^2 + (z - \alpha \sin(\omega t))^2} \right\} \\
&= \frac{(x - x')\alpha\omega \cos(\omega t) \{(x - x')^2 + (y - y')^2 - 4(z - \alpha \sin(\omega t))^2\}}{[(x - x')^2 + (y - y')^2 + (z - \alpha \sin(\omega t))^2]^{\frac{7}{2}}} \quad (4.1.6.30)
\end{aligned}$$

Now approximate, $z - \alpha \sin(\omega t) \sim z$ and with proportionality constant terms:

$$= \frac{3NA\mu_0}{4\pi} \left\{ \frac{(x - x')\alpha\omega \cos(\omega t) \{(x - x')^2 + (y - y')^2 - 4z^2\}}{[(x - x')^2 + (y - y')^2 + (z - \alpha \sin(\omega t))^2]^{\frac{7}{2}}} \right\} \quad (4.1.6.31)$$

The lock-in sees

$$S_{xz} = \frac{V_{xz}}{m_z} = \frac{3NA\mu_0}{4\pi} \left\{ \frac{(x - x')\alpha\omega \{(x - x')^2 + (y - y')^2 - 4z^2\}}{[(x - x')^2 + (y - y')^2 + z^2]^{\frac{7}{2}}} \right\} \quad (4.1.6.32)$$

These expressions are in agreement with the calculations of others [79]. Note that S_{xy} and S_{xz} are cross-talk terms.

For the Mallinson configuration, the pick-up coils are at positions $(X_c, 0, Z_c)$, $(-X_c, 0, Z_c)$, $(X_c, 0, -Z_c)$, $(-X_c, 0, -Z_c)$. This gives for the complete pick-up coil set the following S_{xx} :

$$S_{xx} = \frac{NA3\mu_0\alpha\omega Z_c}{4\pi} \cdot \left\{ \frac{(4(X_c - x')^2 - y'^2 - Z_c^2)}{[(X_c - x')^2 + y'^2 + Z_c^2]^{\frac{7}{2}}} + \frac{(4(X_c + x')^2 - y'^2 - Z_c^2)}{[(X_c + x')^2 + y'^2 + Z_c^2]^{\frac{7}{2}}} \right\}$$

$$\left. \frac{(4(X_c - x')^2 - y'^2 - Z_c^2)}{[(X_c - x')^2 + y'^2 + Z_c^2]^{\frac{7}{2}}} + \frac{(4(X_c + x')^2 - y'^2 - Z_c^2)}{[(X_c + x')^2 + y'^2 + Z_c^2]^{\frac{7}{2}}} \right\} \quad (4.1.6.33)$$

$$= \frac{NA3\mu_0\alpha\omega Z_c}{2\pi}$$

$$\cdot \left. \left\{ \frac{(4(X_c - x')^2 - y'^2 - Z_c^2)}{[(X_c - x')^2 + y'^2 + Z_c^2]^{\frac{7}{2}}} + \frac{(4(X_c + x')^2 - y'^2 - Z_c^2)}{[(X_c + x')^2 + y'^2 + Z_c^2]^{\frac{7}{2}}} \right\} \right\} \quad (4.1.6.34)$$

Note that S_{xx} is indeed even in x' and y' . Assuming that $x'=0$ S_{xx} will have the following y' dependence:

$$S_{xx}(y') = \frac{NA3\mu_0\alpha\omega Z_c}{4\pi} \cdot \left\{ \frac{(4X_c^2 - y'^2 - Z_c^2)}{[X_c^2 + y'^2 + Z_c^2]^{\frac{7}{2}}} + \frac{(4X_c^2 - y'^2 - Z_c^2)}{[X_c^2 + y'^2 + Z_c^2]^{\frac{7}{2}}} \right\}$$

$$\left. \frac{(4X_c^2 - y'^2 - Z_c^2)}{[X_c^2 + y'^2 + Z_c^2]^{\frac{7}{2}}} + \frac{(4X_c^2 - y'^2 - Z_c^2)}{[X_c^2 + y'^2 + Z_c^2]^{\frac{7}{2}}} \right\} \quad (4.1.6.35)$$

$$= \frac{NA3\mu_0\alpha\omega Z_c}{\pi} \cdot \frac{4X_c^2 - y'^2 - Z_c^2}{[X_c^2 + y'^2 + Z_c^2]^{\frac{7}{2}}} \approx K_1 - \frac{NA3\mu_0\alpha\omega Z_c}{\pi[X_c^2 + Z_c^2]^{\frac{7}{2}}} y'^2 \quad (4.1.6.36)$$

Where K_1 is a constant independent of y' and for the approximation, it is assumed that $y'^2 \ll X_c^2 + Z_c^2$. Note that S_{xx} is maximum when the sample is centered in between the y pick-up coils, i.e. when $y'=0$. This is used to align the sample prior to the measurements.

Assuming that $y'=0$, S_{xx} will have the following x' dependence:

$$S_{xx}(x') = \frac{NA3\mu_0\alpha\omega Z_c}{4\pi} \cdot \left\{ \frac{(4(X_c - x')^2 - Z_c^2)}{[(X_c - x')^2 + Z_c^2]^{\frac{7}{2}}} + \frac{(4(X_c + x')^2 - Z_c^2)}{[(X_c + x')^2 + Z_c^2]^{\frac{7}{2}}} \right\} +$$

$$\frac{(4(X_c - x')^2 - Z_c^2)}{[(X_c - x')^2 + Z_c^2]^{\frac{7}{2}}} + \frac{(4(X_c + x')^2 - Z_c^2)}{[(X_c + x')^2 + Z_c^2]^{\frac{7}{2}}} \quad (4.1.6.37)$$

$$= \frac{NA3\mu_0\alpha\omega Z_c}{2\pi} \cdot \left\{ \frac{(4(X_c - x')^2 - Z_c^2)}{[(X_c - x')^2 + Z_c^2]^{\frac{7}{2}}} + \frac{(4(X_c + x')^2 - Z_c^2)}{[(X_c + x')^2 + Z_c^2]^{\frac{7}{2}}} \right\} \quad (4.1.6.38)$$

$$\approx \frac{NA3\mu_0\alpha\omega Z_c}{2\pi[X_c^2 + Z_c^2]^{\frac{7}{2}}} \cdot (4(X_c - x')^2 - Z_c^2) + (4(X_c + x')^2 - Z_c^2) \quad (4.1.6.39)$$

$$= \frac{NA3\mu_0\alpha\omega Z_c}{2\pi[X_c^2 + Z_c^2]^{\frac{7}{2}}} \cdot (8X_c^2 - 2Z_c^2 + 8x'^2) = K_2 + \frac{NA4\mu_0\alpha\omega Z_c}{\pi[X_c^2 + Z_c^2]^{\frac{7}{2}}} x'^2 \quad (4.1.6.40)$$

Where K_2 is a constant independent of x' and it is assumed that $|x'| \ll X_c^2 + Z_c^2$. Note that S_{xx} is minimum when the sample is centered between the x pick-up coils, i.e. $x'=0$.

As it is difficult to center the sample on the sample-rod (0.5-1 mm placement error), and as the sample-rod axis does not coincide with the rotation axis of the sample-rod rotator, the position of the sample depends on the field angle. Videos taken with a camera while rotating the sample show that the sample describes a circle when it is rotated over 360 degrees. We refer to this as a wobble.

For the current setup, the radius of the circle depends on the orientation of the quartz rod in the sample-rod holder, the orientation of the Dremel insert in the sample-rod holder, and the position of the sample on the quartz rod. The wobble radius is approximately 2 mm. The position of the wobble circle depends on the sample alignment. As for a typical VSM measurement, the sample is just aligned at 0 degrees, the center of the circle does not coincide with the center of the pick-up coil set. Assuming that the location of the

wobble circle is given by (x_o, y_o) . Furthermore, we define the radius of the wobble circle to be r . See figure below (fig. 4.9) for our definition. Furthermore, we assume that the exact location of the sample depends on the field angle θ according to the following expressions and the center of the pick-up coil set is at the origin:

$$x'(\theta) = r \cdot \cos(\theta) + x_o \quad (4.1.6.41)$$

$$y'(\theta) = r \cdot \sin(\theta) + y_o \quad (4.1.6.42)$$

So for this particular wobble $S_{xx}(\theta)$ will be given by:

$$S_{xx} = \frac{NA^3 \mu_0 \alpha \omega Z_c}{4\pi} \cdot \left\{ \frac{(4(X_c - r \cdot \cos(\theta) - x_o)^2 - (r \cdot \sin(\theta) + y_o)^2 - Z_c^2)}{[(X_c - r \cdot \cos(\theta) - x_o)^2 + (r \cdot \sin(\theta) + y_o)^2 + Z_c^2]^{\frac{7}{2}}} + \frac{(4(X_c + r \cdot \cos(\theta) + x_o)^2 - (r \cdot \sin(\theta) + y_o)^2 - Z_c^2)}{[(X_c + r \cdot \cos(\theta) + x_o)^2 + (r \cdot \sin(\theta) + y_o)^2 + Z_c^2]^{\frac{7}{2}}} \right\} \quad (4.1.6.43)$$

$$\approx \frac{NA^3 \mu_0 \alpha \omega Z_c}{4\pi [X_c^2 + Z_c^2]^{\frac{7}{2}}} \cdot \{4(X_c - x_o)^2 + 4(X_c + x_o)^2 - 2(y_o^2 + Z_c^2) + 3r^2 +$$

$$4r^2 \cos(2\theta) + 16x_o r \cdot \cos(\theta) - 4y_o r \cdot \sin(\theta)\} \quad (4.1.6.44)$$

$$= K_3 + K_4 \cos(2\theta) + K_5 \cos(\theta + \theta_o) \quad (4.1.6.45)$$

With K_3 , K_4 , K_5 , and θ_o constants. For the approximation, we assumed that $X_c^2 + Z_c^2 \gg (r \cdot \cos(\theta) + x_o)^2 + (r \cdot \sin(\theta) + x_o)^2$. This equation indicates that the $S_{xx}(\theta)$ contains oscillating terms with period 2π and π whose relative amplitudes and phases depend on the wobble radius (r) and the position of the wobble center (x_o, y_o) . In the further text the

term with period 2π is referred to as the 1θ term and the term with period π referred to as 2θ term. For $r=0$ the oscillating terms are zero. For the case the wobble center is at the origin, i.e. $(x_0, y_0)=(0,0)$ the 1θ -term is zero. Note that $S_{xx}(\theta)+S_{xx}(\theta+\pi)$, which we refer to as symmetric sensitivity, only contains the 2θ component. From the equation above one can see that the symmetric angular sensitivity function only depends on the wobble radius and is to first order independent of the position of the wobble center. The use of the symmetric angular sensitivity function is therefore preferred if the type of sample permits this approach.

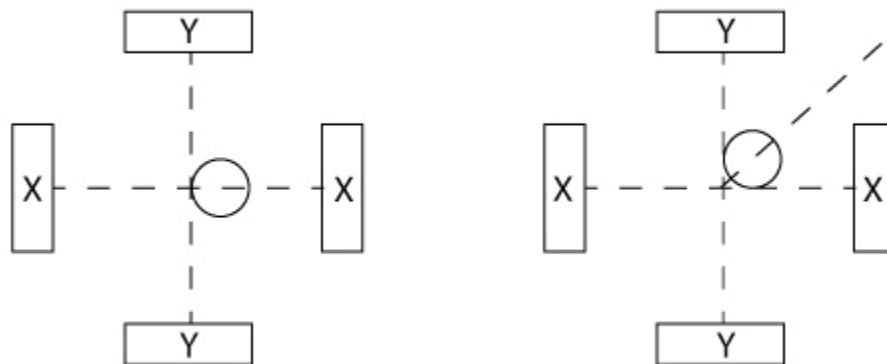


Figure 4. 9. wobble circle ($r=1$) at position $(1,0)$ (left) and at wobble circle ($r=1$) at position $(1,1)$.

The figure below shows the X-coil and Y-coil signal of a circular 3.5" floppy disk sample as a function of the field angle. Prior to taking the measurements, this sample was aligned at 0, 90, 180, and 270 degrees. For each alignment, the x and y micrometers were recorded. The average position was calculated from the recorded alignment positions and

the sample was moved to that average position before starting the measurement. Then the angular sensitivity was measured shown in the graph on the left in the figure below. One can see that still a small 1θ angular sensitivity is present, which shows the challenge of centering the sample by hand. The graph on the right shows the symmetric angular sensitivity calculated by averaging the sensitivity at θ and $\theta+180$ degrees. Both the sensitivity for the x and y-direction are sinusoidal and have approximately the same angle. These results confirm the above calculations in particularly equation 4.1.6.45.

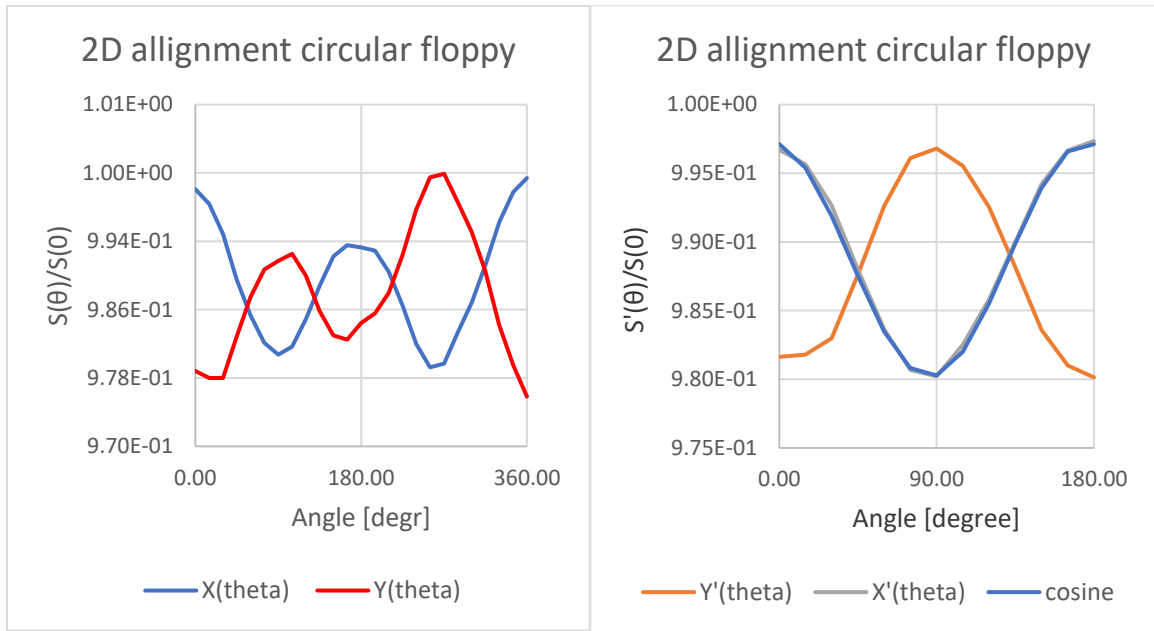


Figure 4. 10. Normalize angular dependence of sensitivity: sample centered by positioning at average alignment position (left) and normalized symmetric angular sensitivity ($S_{xx}'(\theta)/S_{xx}(0)=0.5(S_{xx}(\theta)/S_{xx}(0)+S_{xx}(\theta+\pi)/S_{xx}(0))$) calculated by averaging the normalized sensitivity at θ and $\theta+180$ degrees (right).

For the cross-talk term S_{xy} of the complete pick-up coil set we find:

$$S_{xy} = \frac{15NA\mu_0\alpha\omega}{4\pi} \cdot \left\{ -\frac{y'(X_c - x') Z_c}{[(X_c - x')^2 + y'^2 + Z_c^2]^{\frac{7}{2}}} + \frac{y'(X_c + x') Z_c}{[(X_c + x')^2 + y'^2 + Z_c^2]^{\frac{7}{2}}} - \frac{y'(X_c - x') Z_c}{[(X_c - x')^2 + y'^2 + Z_c^2]^{\frac{7}{2}}} + \frac{y'(X_c + x') Z_c}{[(X_c + x')^2 + y'^2 + Z_c^2]^{\frac{7}{2}}} \right\} \quad (4.1.6.46)$$

$$= \frac{30NA\mu_0\alpha\omega y' Z_c}{4\pi} \cdot \left\{ -\frac{X_c - x'}{[(X_c - x')^2 + y'^2 + Z_c^2]^{\frac{7}{2}}} + \frac{X_c + x'}{[(X_c + x')^2 + y'^2 + Z_c^2]^{\frac{7}{2}}} \right\} \quad (4.1.6.47)$$

Note that S_{xy} is odd in x' and y' . Note that S_{xy} is zero if $x'=0$ and/or $y'=0$. So, both

$S_{xy}(x')|_{y'=0}$ and $S_{xy}(y')|_{x'=0}$ or zero.

To understand the effect of the wobble we consider two cases, i.e. the wobble center close to the origin or the wobble center farther away from the origin. If the wobble center is close to the origin one expects that the cross-talk will be zero for four different angles assuming that the wobble trajectory intersects both the x and y-axis. If the wobble center is farther away from the origin than the wobble radius, there will be cross-talk for all angles. In the intermediate case where the sample position is adjusted for a single angle, the number of angles for which the cross talk is zero depends on wobble radius r and the position of the wobble center (x_0, y_0) and can be two or three. The effect of cross-talk is

shown in the figure on the left below which shows the m_y hysteresis curve at 0, 180, and 360 degrees of a circular 3.5% floppy disk sample. This measurement was done using the transverse rod. The sample was aligned at 180 degrees, so we believe that the m_y curve measured at 180 degrees shows the true m_y hysteresis curve. The m_y hysteresis curves measured at 0 and 360 degrees look like the m_x hysteresis curve and we believe it mainly originates from cross-talk. The high field dependence of all three m_y curves is caused by the field dependence of the m_y as the m_x is mostly saturated for those fields. The low field dependence of the curves measured at 0 and 360 degrees is mainly caused by the field dependence of the sample's M_x . The figure below on the right shows the M_x hysteresis curve of the sample. Note that the M_x hysteresis curve of a 3.5" floppy sample is independent of the angle.

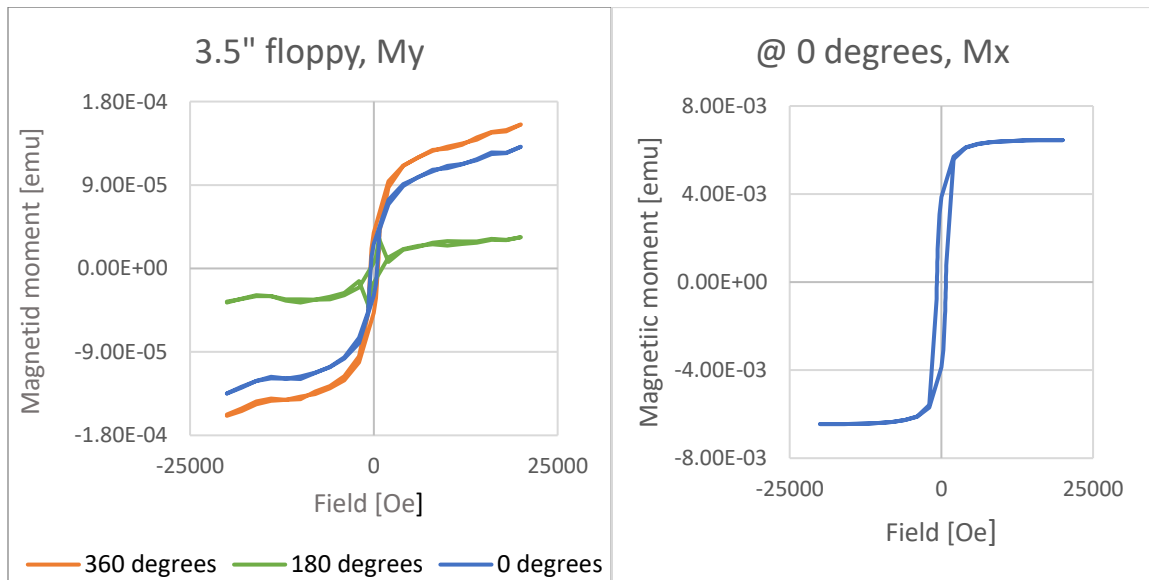


Figure 4. 11. M_y hysteresis curve measured at 0, 180, and 360 degrees, and M_x hysteresis curve of circular 3.5" floppy sample at 0 degrees.

To further understand the effect of a wobble on the cross-talk, expressions (4.1.6.41) and (4.1.6.42) are substituted in the expression for S_{xy} given above (i.e. equation 4.1.6.47).

$$S_{xy}(\theta) = \frac{30NA\mu_0\alpha\omega(r \cdot \sin(\theta) + y_o)Z_c}{4\pi}.$$

$$\left\{ \begin{aligned} & - \frac{X_c - r \cdot \cos(\theta) - x_o}{[(X_c - r \cdot \cos(\theta) - x_o)^2 + (r \cdot \sin(\theta) + y_o)^2 + Z_c^2]^{\frac{7}{2}}} \\ & + \frac{X_c + r \cdot \cos(\theta) + x_o}{[(X_c + r \cdot \cos(\theta) + x_o)^2 + (r \cdot \sin(\theta) + y_o)^2 + Z_c^2]^{\frac{7}{2}}} \end{aligned} \right\} \quad (4.1.6.48)$$

$$\approx \frac{60NA\mu_0\alpha\omega(r \cdot \sin(\theta) + y_o)(r \cdot \cos(\theta) + x_o)Z_c}{4\pi[X_c^2 + Z_c^2]^{\frac{7}{2}}} \quad (4.1.6.49)$$

$$= \frac{60NA\mu_0\alpha\omega Z_c}{4\pi[X_c^2 + Z_c^2]^{\frac{7}{2}}} \left\{ \frac{1}{2}r^2 \sin(2\theta) + r(x_o \cos(\theta) + y_o \sin(\theta)) + x_o y_o \right\} \quad (4.1.6.50)$$

$$= K_6 + K_7 \sin(2\theta) + K_8 \sin(\theta) \quad (4.1.6.51)$$

Where K_6 , K_7 , and K_8 are constants and we assumed that $X_c^2 + Z_c^2 \gg r^2 + x_o^2 + y_o^2$.

Note that the angular dependence of the cross-talk contains a 2θ , a θ term, and an offset.

The amplitude and the relative phase of the θ and 2θ terms depend on the wobble radius r and the wobble center (x_o, y_o) . If the wobble radius is zero, the angular dependence of the cross-talk will be zero. If the wobble center is positioned at the origin, the cross-talk will not contain an offset or a θ -term.

The exact position of the wobble center and wobble radius can be calculated from the relative amplitude and phase of the θ and 2θ components in the angular sensitivity function for the X-coils. We can rewrite the angular part of the sensitivity (from equation 4.7.44) as:

$$4r^2 \cos(2\theta) + 4y_o r \cdot \left(\frac{4x_o}{y_o} \cdot \cos(\theta) - \sin(\theta) \right) \quad (4.1.6.52)$$

$$= 4r^2 \cos(2\theta) + 4y_o r \cdot \left(\frac{1}{\tan(\theta_c)} \cdot \cos(\theta) - \sin(\theta) \right) \quad (4.1.6.53)$$

$$= 4r^2 \cos(2\theta) + \frac{4y_o r}{\sin(\theta_c)} \cdot (\cos(\theta_c) \cdot \cos(\theta) - \sin(\theta_c) \cdot \sin(\theta)) \quad (4.1.6.54)$$

$$= 4r^2 \cos(2\theta) + \frac{4y_o r}{\cos(\theta_c)} \cdot \cos(\theta + \theta_c) \quad (4.1.6.55)$$

So, the relative phase shift between the θ and 2θ components of the angular sensitivity, i.e. θ_c and the relative amplitude ratio of the θ and 2θ components of the angular sensitivity relate to wobble center and wobble radius via the following equations:

$$\tan(\theta_c) = \frac{y_o}{4x_o} \quad (4.1.6.56)$$

$$\frac{K_4}{K_5} = \frac{r}{y_o} \cos(\theta_c) \quad (4.1.6.57)$$

Note that the wobble radius can be calculated from the symmetric sensitivity function after which one can determine the wobble center (x_o, y_o) from the equation provided above.

Similarly, it is possible to determine the wobble center from the angular dependence of the crosstalk.

$$\frac{1}{2}r^2 \sin(2\theta) + y_o r \left(\frac{x_o}{y_o} \cos(\theta) + \sin(\theta) \right) \quad (4.1.6.58)$$

$$= \frac{1}{2}r^2 \sin(2\theta) + y_o r (\tan(\theta_s) \cos(\theta) + \sin(\theta)) \quad (4.1.6.59)$$

$$= \frac{1}{2}r^2 \sin(2\theta) + \frac{y_o r}{\cos(\theta_s)} (\sin(\theta_s) \cos(\theta) + \cos(\theta_s) \sin(\theta)) \quad (4.1.6.60)$$

$$= \frac{1}{2}r^2 \sin(2\theta) + \frac{y_o r}{\cos(\theta_s)} \sin(\theta + \theta_s) \quad (4.1.6.61)$$

So, the relative phase shift between the θ and 2θ components of the angular crosstalk, i.e. θ_s and the relative amplitude ratio of the θ and 2θ components of the angular crosstalk relate to wobble center and wobble radius via the following equations:

$$\tan(\theta_s) = \frac{x_o}{y_o} \quad (4.1.6.62)$$

$$\frac{K_7}{K_8} = \frac{r}{y_o} \cos(\theta_s) \quad (4.1.6.63)$$

Note that the (x_o, y_o) is the wobble center with respect to the x-coil-set origin.

For any sample that can be saturated, one can determine $S_{xx}(\theta)$ and $S_{yx}(\theta)$. One would saturate the sample and measure the M_x and the M_y as a function of the field angle. From the angle dependence of the symmetric sensitivity, i.e. $0.5(S_{xx}(\theta)+S_{xx}(\theta+180))$, one will be able to determine the wobble radius. Then one can determine the position of the wobble center in the x-coils coordinate system (x_{ox},y_{ox}) using equations (4.1.6.56) and (4.1.6.57) and the position of the wobble center in the y-coils coordinate system (x_{oy},y_{oy}) using equations (4.1.6.62) and (4.1.6.63). This will allow us to model angular sensitivity and angular crosstalk using 5 parameters to remove the effect of wobble on the signals.

At this moment it is not clear if this method will work on asymmetric samples. The wobble of asymmetric samples can be described by the wobble of two samples that have a different wobble radius.

4.1.7 Calculation of Sensitivity and cross talk

Using the expressions derived in the previous section we calculated the sensitivity and cross-talk as a function of the position for the Mallinson's coil configuration using arbitrary values for A, N, and the positions of the coils [79]. For this calculation, the sign configuration was done according to Bernards and Schrauwen [80]. Contour plots for the normalized sensitivity in the x-direction (S_{xx}) and the normalized cross-talk (S_{xy}) are given in the figure below.

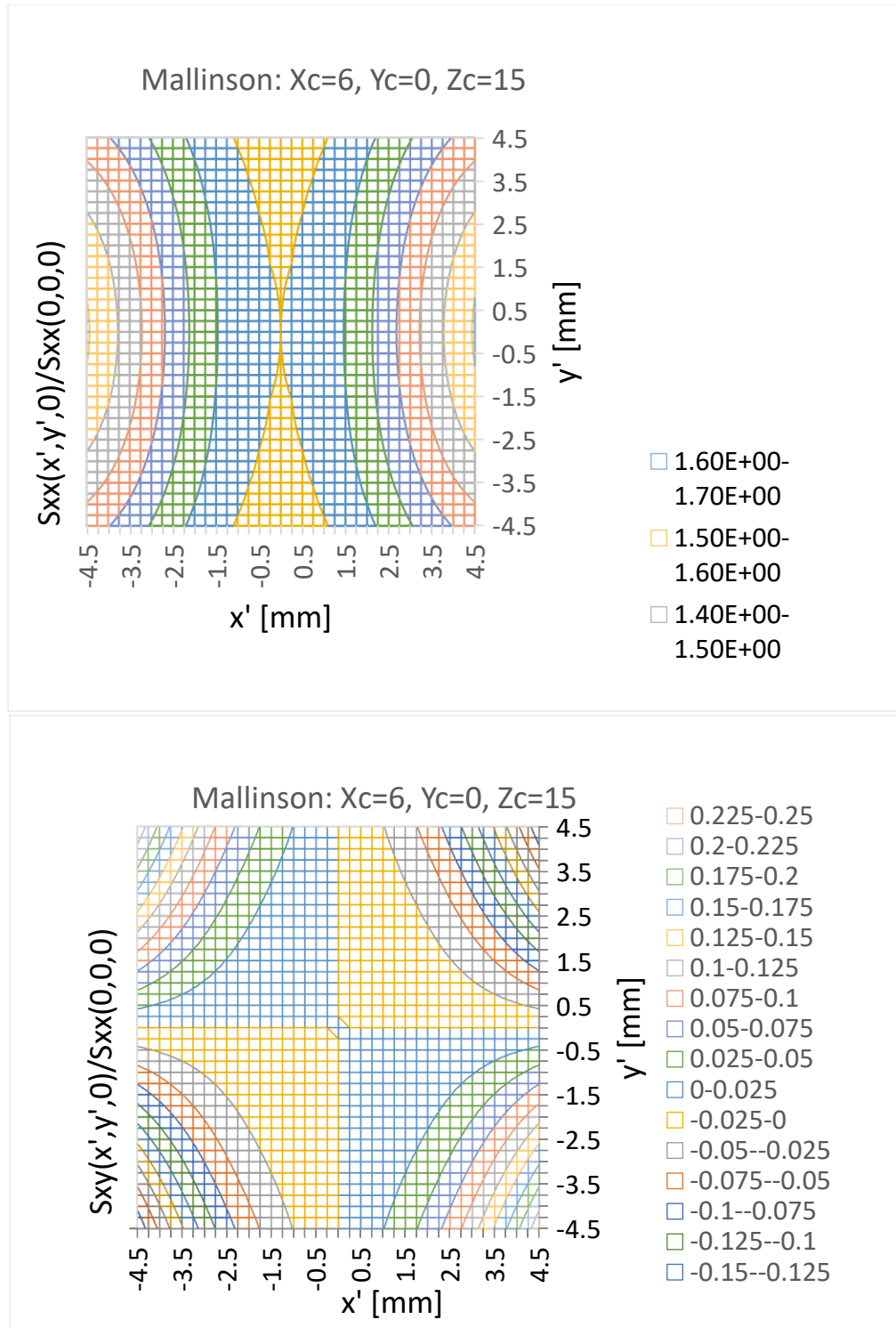


Figure 4. 12. Normalized Sensitivity (top) and normalized cross talk (bottom) as a function of the position for the Mallinson's coil configuration. Coil position in mm.

The left contour plot shows the sensitivity function for the x-coils, and the right shows the contour plot of the cross-talk term. The sensitivity function is even in x and y and has a local extreme at the origin between the pick-up coils. The cross-term function is odd in x and y and is zero at the center in between the pick-up coils but has a non-zero slope and might give a larger contribution to the measured signal for slightly misaligned samples than the S_{xx} term.

4.1.7.1 Dependence of sensitivity and cross talk on the position of the sample

Fig 4.13(a) shows the position dependence of the normalized sensitivity ($S_{xx}(x',0,0)/S_{xx}(0,0,0)$) on the sample position for a sample displacement in x-direction assuming perfect alignment along y' and z' -direction. It has been shown that S_{xx} is minimum if the sample is exactly in the middle of the x-coils. Figure 4.13(b) shows the dependence of $S_{xx}(0,y',0)/S_{xx}(0,0,0)$ on the sample position for the displacement in y' -direction assuming perfect alignment along x' and z' -direction. The S_{xx} is maximum if the sample's y' -coordinate is zero. These results are consistent with the alignment procedure of Fig. 2.3.

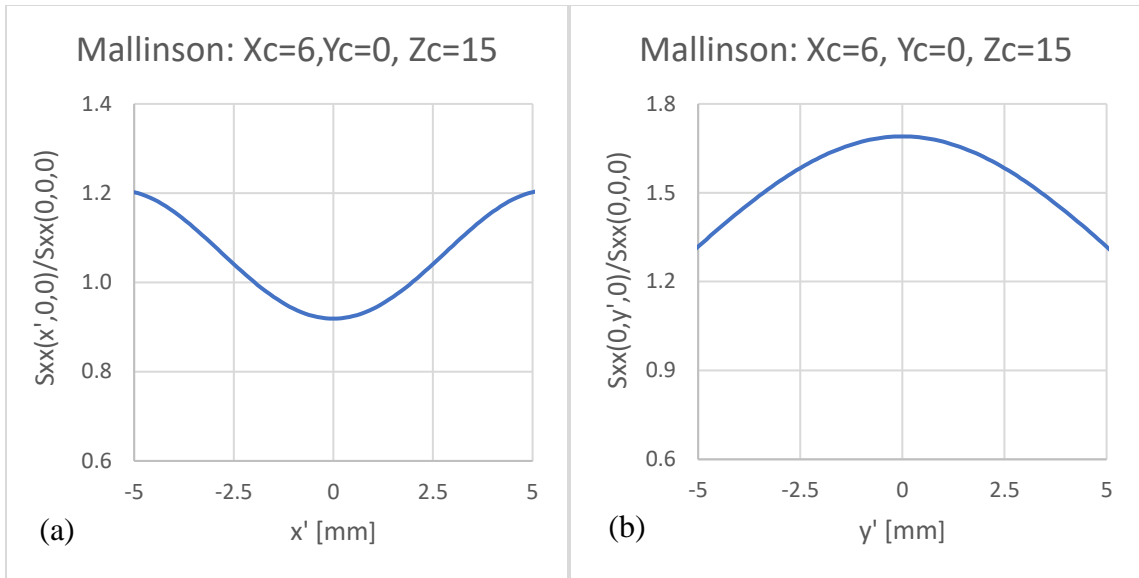


Figure 4. 13. Dependence of normalized sensitivity (S_{xx}) on the sample position for the sample displacement in (a) x' -direction assuming perfect alignment for y' and z' (b) y' -direction assuming perfect alignment for x' and z' .

Figure 4.14(a) below shows the variation of the normalized cross-talk ($S_{xy}(x', -1, 0) / S_{xx}(0, 0, 0)$) on the sample position for the sample displacement in x' -direction assuming $y' = -1$ mm and perfect alignment for z' . Figure 4.14(b) below shows the variation of cross talk (S_{xy}) on the sample position for the sample displacement in the y' -direction assuming $x' = -1$ mm and perfect alignment for z' . The cross talk is zero if the sample is exactly at the x' -center of the y -coils. Similarly, figure 4.14(b) shows that the cross talk is zero when the sample is exactly at the y' -center of the y -coils. This suggests that if the wobble center coincides with the center of the y' -pickup coils the measured signal has no cross-talk component. It has been shown that the cross-talk signal is

identical on either direction from the center of pick-up coils. However, the x' dependence is different from the y' -dependence.

Above results leads us toward a useful alignment procedure. The correct alignment of the sample is very important when studying anisotropic samples. Only when the sample is perfectly centered the cross talk will be zero and the measured x-signal only depends on the sample's m_x . Therefore, before the start of the measurement, the x-signal should be minimized by adjusting the x-position and maximized by adjusting the y-position. This moves the sample exactly to the center of the x-pick-up coil set. If the origin of the x-pick-up coil set coincides with the y-pick-up coil set the measured signal will be free from cross talk. In reality both origins are slightly difference therefore MicroSense recommends after above described alignment procedure to make adjustments to the y' -position to reduce the cross-talk. Strictly speaking the position of the sample need to be adjusted after each field angle change as because of concentricity issues of the sample-sample-rod system the sample's position varies with the field angle. Since the cross talk is zero for $x'=0$ and or $y'=0$ it might be difficult to center both the x' and y' position of the sample using just the cross-talk signal. Therefore, above described two-step process is recommended.

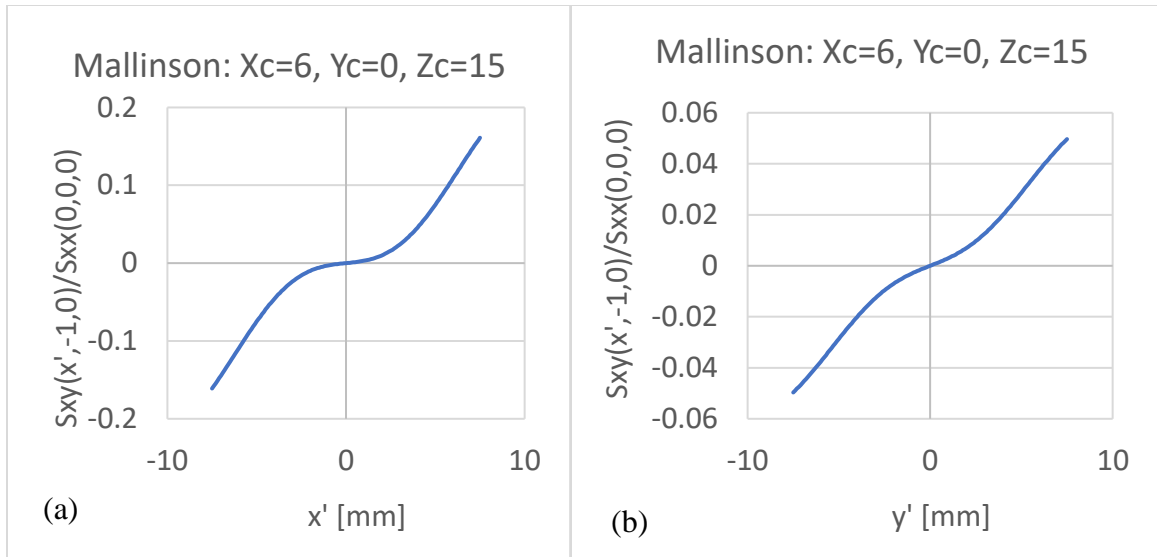
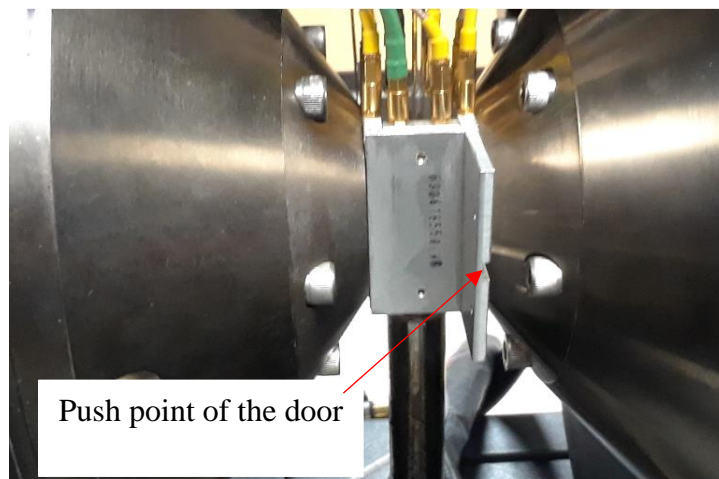


Figure 4. 14. Position dependence of normalized cross-talk on the sample position for the sample displacement in (a) x' -direction assuming perfect alignment for z' and $y'=-1$, (b) y' -direction assuming perfect alignment for z and $x'=-1$.

Note: The exact center of Y-coils depends on the distance between pole pieces and how one pushes the door to lock it before starting the measurements.



4.1.7.2 Angular dependence of sensitivity and cross-talk

Figure 4.15 shows the calculated normalized angular dependence of the sensitivity of the X-coils and Y-coils. The calculations were done based on the sensitivity derived in section 4.1.6. When the wobble is centered at the origin, the angular dependence shows a 2θ dependence (fig 4.15, left). A wobble that is off-centered will cause angular dependence that contains a 2θ dependent term and a θ dependent term (fig 4.15, right). The angular dependence of the normalized x and y-sensitivities seem to be opposite to each other.

Figure 4.16 shows the calculated normalized angular dependence of the cross-talk. When the wobble is centered at the origin (fig.4.16, left) the cross-talk signal is a nice sine function. On the other hand, if the wobble center is off-center (right figure), the cross-talk signal is partly bell-shaped.

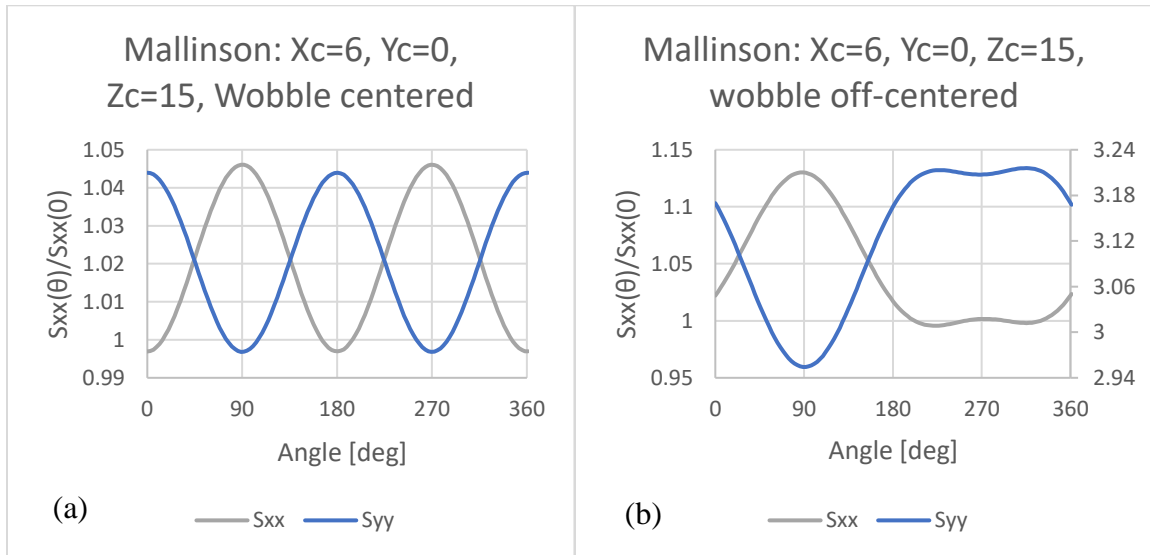


Figure 4. 15. Angular dependence of normalized sensitivity with (a) wobble center at the origin, (b) wobble off-centered.

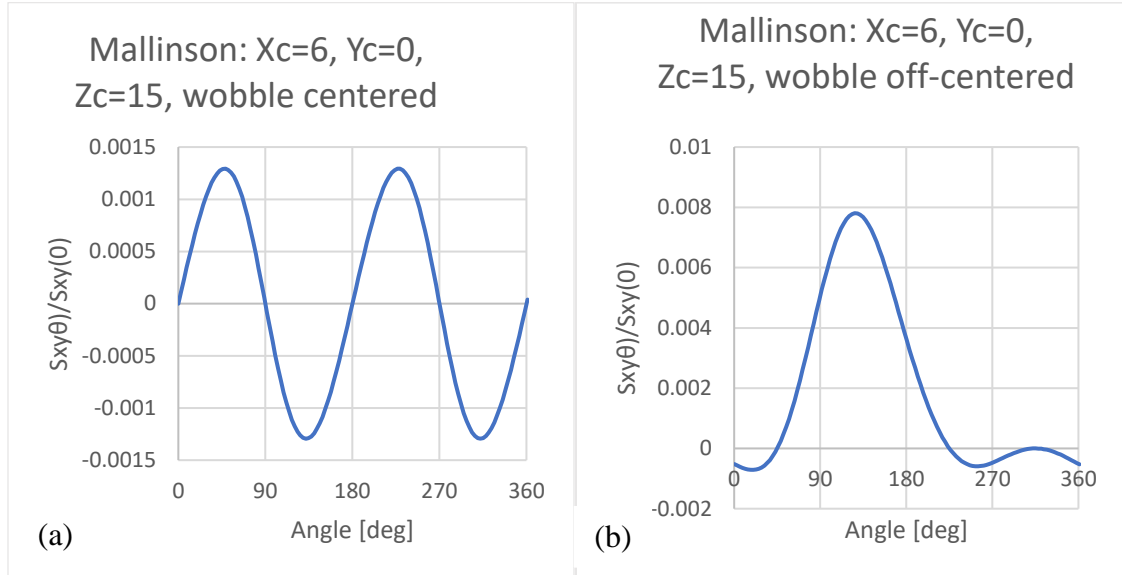


Figure 4. 16. Angular dependence of normalized cross-talk with (a) wobble centered at the origin, (b) wobble off-centered.

4.2 VSM Measurement Results

4.2.1 IRM and DCD Measurement of 3.5" floppy

The magnetization irreversible process can be investigated through remanence curves including IRM and DCD. The remanence measurements can sense the irreversible magnetization component and allows for the determination of the switching field distribution [81]. Under both IRM and DCD remanence measurements, an increasing positive field is applied and removed to allow the measurement of the remanent magnetic moment at zero fields. These two measurements differ only with the initial magnetic

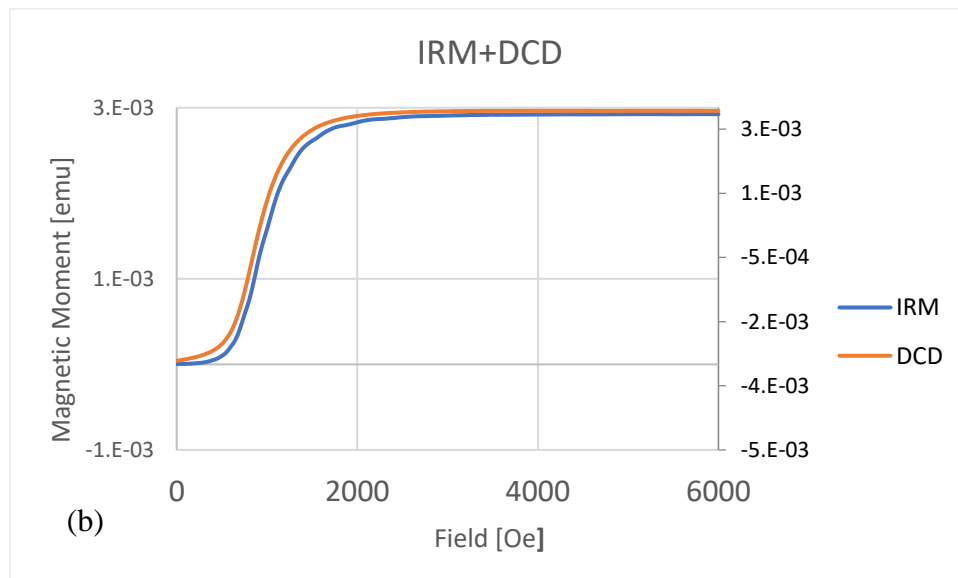
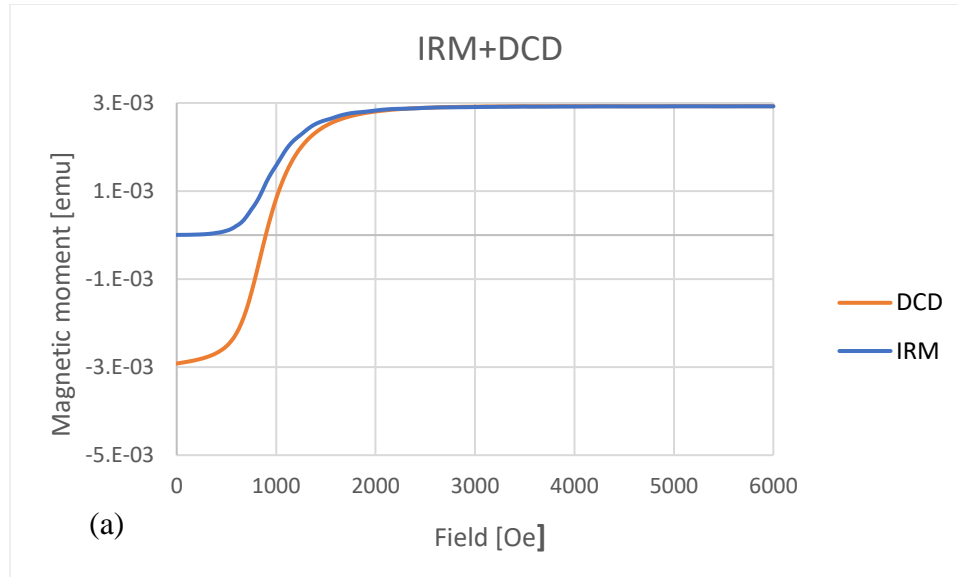
state. IRM is measured from the demagnetized state whereas the DCD is measured from the saturated state. For more details on the measurement procedure see sections 2.5.3 and 2.5.4.

4.2.2 IRM and DCD measurement of 3.5” floppy

The IRM and DCD curves of a circular 3.5” floppy are shown in figure 4.17(a). The magnetic moment exhibits a stable character with nearly zero for the IRM and nearly negative saturation value for the DCD curve when the applied field is below 500 Oe. A fast increase is observed in both IRM and DCD remanence curves in the field range 500 Oe -1500 Oe followed by slower variations at higher fields. The derivative of both curves tells something about the switching field distribution of the particles or domains. Both curves do not have the exact same field dependence which can be seen when we plot the graphs on two different y-axes as shown in figure 4.17(b). The DCD has a larger slope at small fields than the IRM which is caused by the interaction of the domains. The interaction is believed to be negligible for low fields of the IRM curves when the sample is in the demagnetized state.

By comparing the normalized remanences in a Henkel plot or delta M plot, the nature of magnetic interaction can be easily identified. In figure 4.17(c), the Henkel plot shows that the measured curve lies below the Wohlfarth line, a behaves as a system of non-exchange interacting particles which means that strong negative interaction exists between the grains of the floppy sample. In figure 4.17(d), the delta M plot shows the negative peak

around 800 Oe -1000 Oe revealing the domination of strong negative interaction between the particles of the floppy sample.



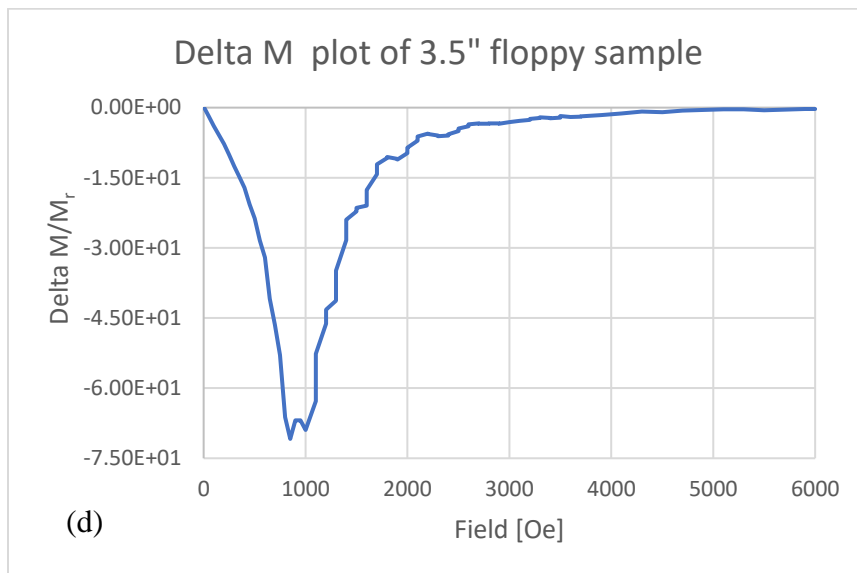
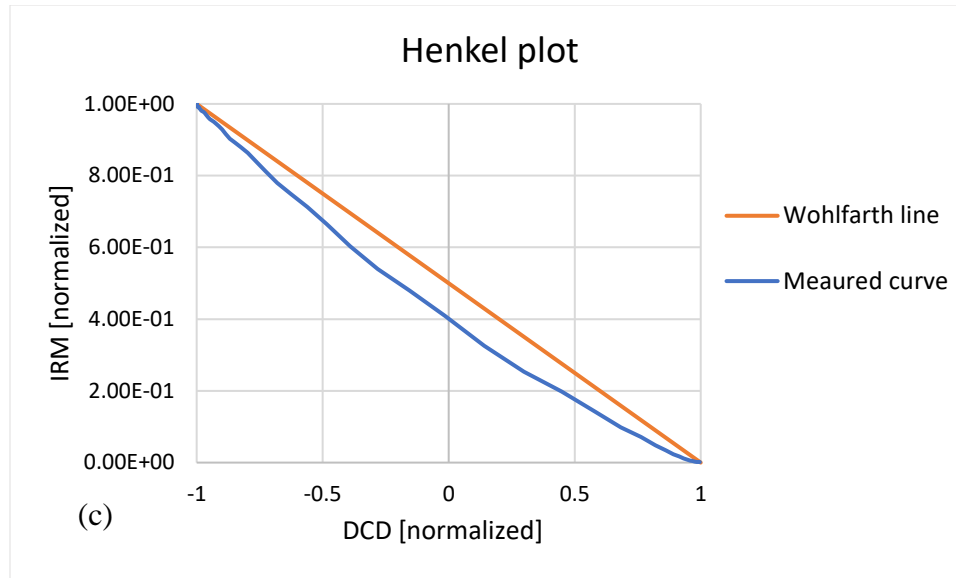
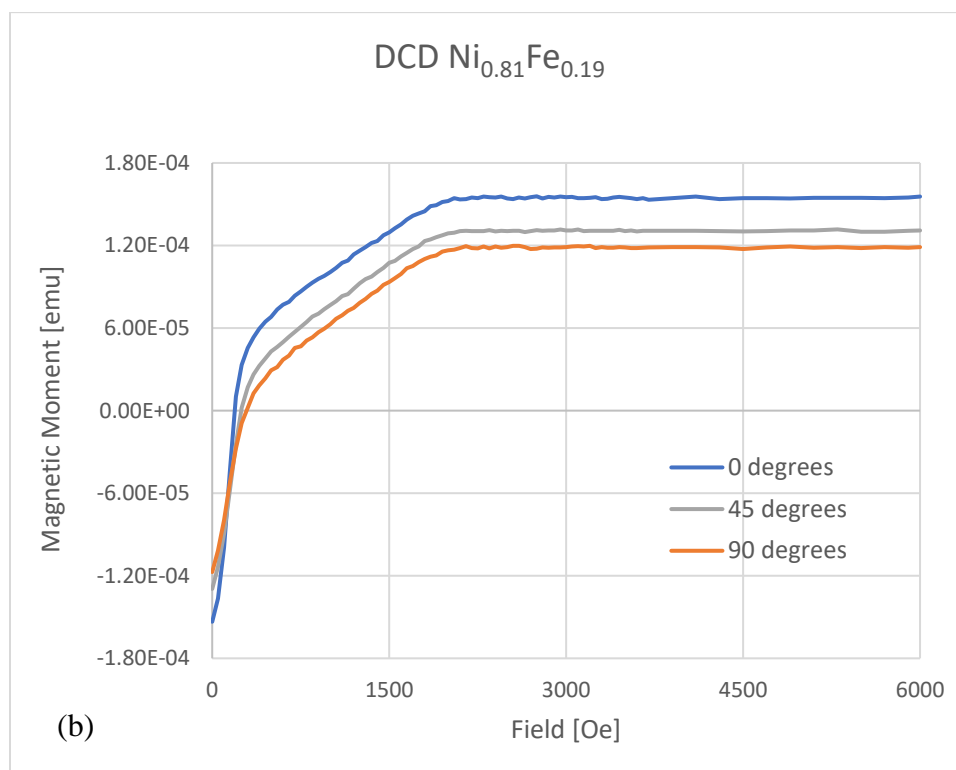
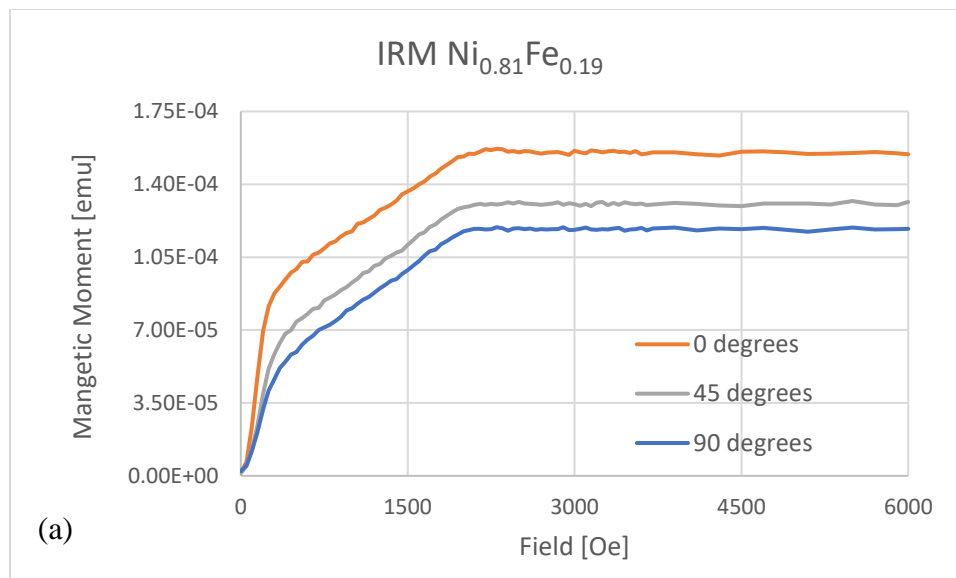


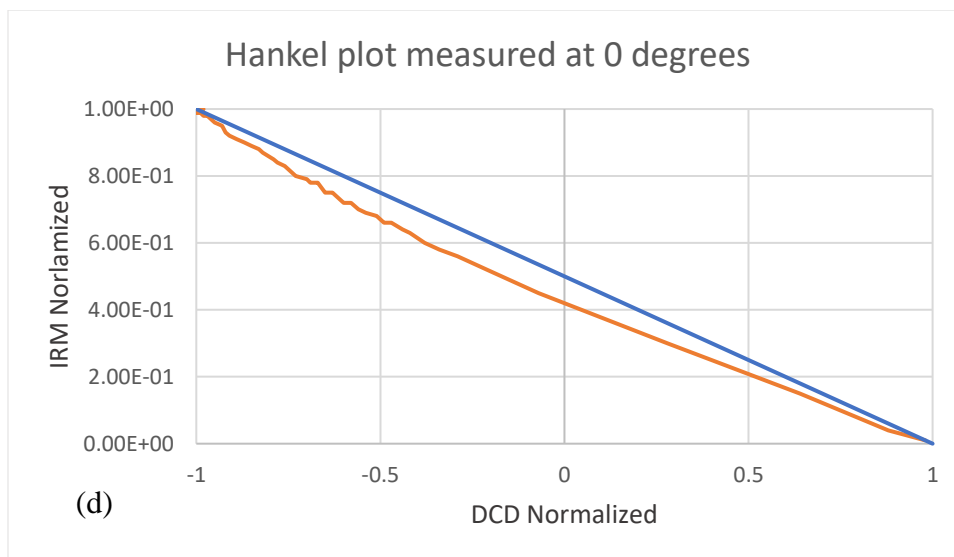
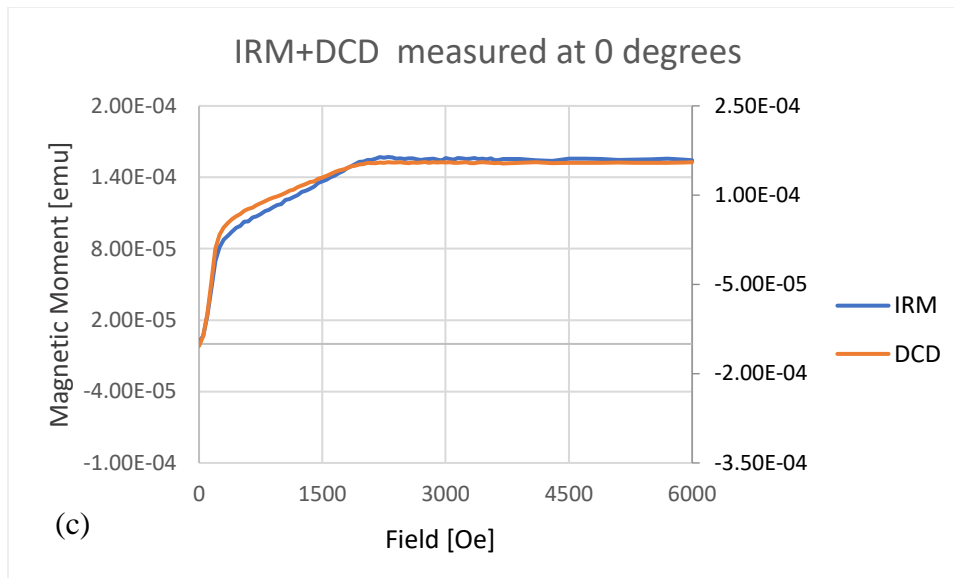
Figure 4. 17. (a) and (b) IRM and DCD measured between 0- 6000 Oe. (c) Hankel plot and (d) Delta m plot showing the negative magnetic coupling of floppy.

4.2.3 IRM and DCD measurement of Ni_{0.81}Fe_{0.19} sample

The IRM and DCD plot of a Ni_{0.81}Fe_{0.19} sample sputtered in a magnetic field is shown in figure 4.18. The measurements were done along three different angles: i.e. 0 degrees (easy axis), 90 degrees (hard axis) and 45 degrees (intermediate angle). A sharp increase is observed in both the IRM (fig 4.18a) and DCD (fig 4.18b) remanence curves when the applied field is below 250 Oe. In the field range 0-2000 Oe, both IRM and DCD curves measured at zero degrees has the highest slope and 90 degrees has the lowest slope. It has been shown that there is a very slow variation of all IRM and DCD remanence curves at higher fields. Both curves have the exact same field dependence at the small fields. The DCD has a larger slope than IRM in the field range of 250 Oe-1800 Oe which can be seen when we plot the graphs on two different y-axes as shown in figure 4.18(c).

The magnetic interactions that exist in Ni_{0.81}Fe_{0.19} sample are explored by the Hankel plot (fig. 4.18d) and the Delta M plot (fig.4.18e) shown in the figure below. The measured curve in the Hankel plot lies below the Wohlfarth line, suggesting the film acts like a system of noninteracting domains which means that strong negative interaction exists between the domains of the Ni_{0.81}Fe_{0.19} sample. The delta M plot shows the negative peak around 200 Oe -400 Oe revealing the domination of a strong negative interaction between the domains of the Ni_{0.81}Fe_{0.19} sample. Although the Delta M plot shows more noise, it also suggests negative interaction between the domains.





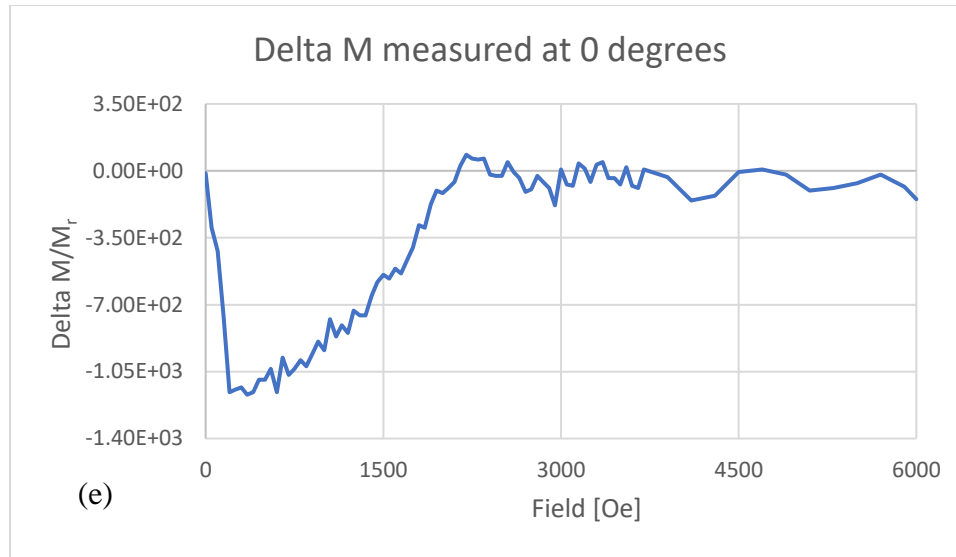


Figure 4. 18.(a) IRM, (b) DCD, (c) IRM and DCD measured 0-6000 Oe, (d) Hankel plot, (e) Delta M plot showing the negative magnetic coupling of $\text{Ni}_{0.81}\text{Fe}_{0.19}$ sample.

4.2.4 Time-Dependent Measurements

Time-dependent measurements investigate the stability of magnetization over time. This can be performed in two ways: (a) measuring the magnetization of a sample as a function of time in the presence of a constant field ;(b) measuring the coercivity as a function of the rate at which the field is changed from the hysteresis loop. In this section, we have adopted the first method. The time-dependent phenomenon in magnetic materials arises from a variety of sources including for example shape or crystalline anisotropy in fine particle system or pinning mechanism in materials dominated by domain wall motion [82]. The switching of the magnetization from one stable direction to another in the opposite direction to the initial magnetization which may be described as metastable

involves the overcoming of the energy barrier that arises from thermal activation of the metastable magnetization states over an energy barrier [74][83]. The height of the energy barrier determines the probability per unit time of switching. The applied magnetic field promotes magnetic reversal by reducing the effective barrier height. Thus the occurrence of switching depends not only the strength of the applied field but also on how long that field is applied [75]. Street et al. [74] have been shown that the change in magnetization with time(t) is given by:

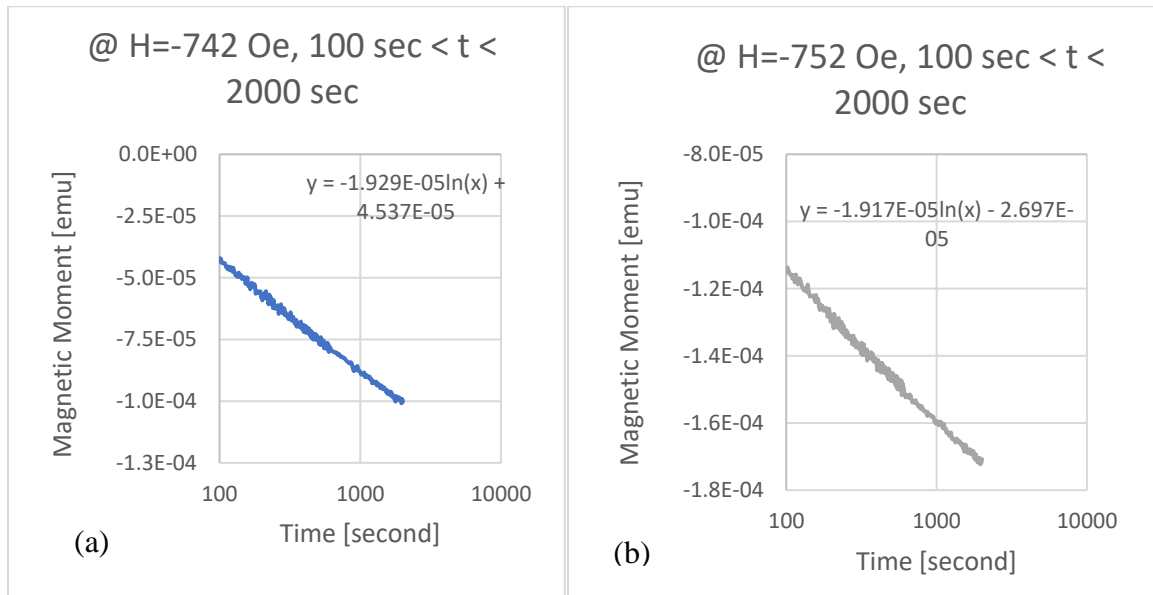
$$\Delta M = AkT \left\{ (\log t) - C \exp\left(-\frac{E_0}{kT}\right) t + \text{constant} \right\} \quad (4.2.4.1)$$

Where A and C are constants, k is Boltzmann constant and T is absolute temperature and E_0 is the activation energy. Since $E_0 \gg kT$ and $C \exp\left(-\frac{E_0}{kT}\right) \ll t$ the equation (4.9.1) is linear in semi-log only for large values of t . Therefore, one often removes the data measured for small t values when determining the slope of a semi-log plot. For the derivation of equation (4.91) Street et al. assumed a uniform distribution of energy barriers.

The largest time dependence is often observed for field values close to zero magnetic moment, which corresponds to the coercivity values of the hysteresis curve. In fact, Coercivity is often defined as the field where the time-dependency is largest. Therefore, any time-dependent measurements should start with measuring the hysteresis curve in step mode for that particular field angle. One should then carefully determine the field intervals for which the hysteresis curve has a large slope. It is recommended to do time-dependent measurements at more field values for that field range where the slope of the hysteresis curve is largest.

4.2.4.1 Calculation of slope from the time-dependent measurement of 3.5” floppy

In figure 4.19 (a) through (f) M-t behavior is shown for different field values for a circular 3.5” floppy sample. The slope was calculated by using the data points from $t=100$ to $t=2000$ seconds. The first 100 seconds of data is not used for the fit for two reasons: (a) Theory (see previous sections) does show that only for large t the time dependence is linear on a semi-log graph (see also above) [74][83][75]; (b) It is difficult to realize a perfect applied field step with an electromagnet, so there is always some form of overshoot. It has been shown by Serletis et al. [83] that a small field overshoot mainly affects the time dependence directly after the field step and has a minor effect on the time dependence for larger t . The semi-log fit has been employed to calculate the slope to three meaningful significant digits. The slope versus field curve in figure 4.20 shows that the slope is maximum around coercivity and decreases on either side of the coercivity.



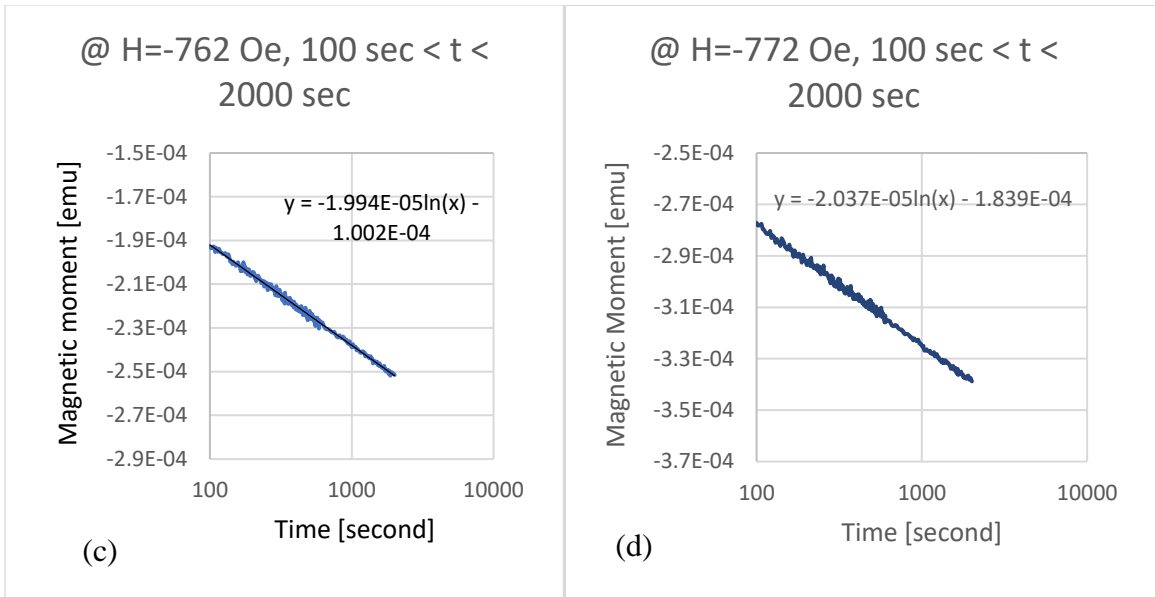


Figure 4. 19. calculation of the slope of magnetic moment versus time graph of circular 3.5" floppy disc sample as a function of the magnetic field.

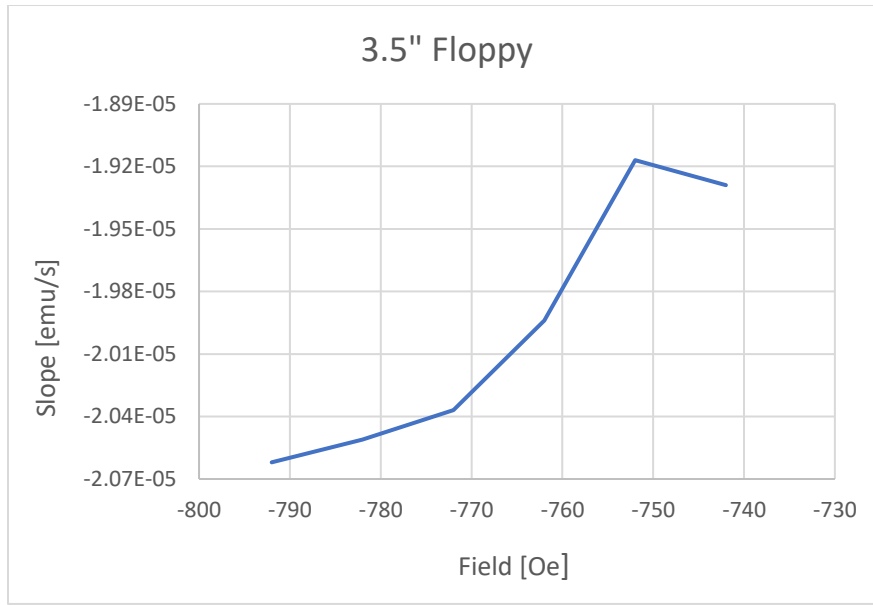


Figure 4. 20. variation of the slope with applied magnetic fields in the opposite direction of initial magnetic moment.

4.2.4.2 Time-dependent measurement of VHS tape

The time-dependent measurements of VHS tape performed at room temperature are shown in figure 4.21 and 4.22. Figure 4.21 is the plot of the magnetic moment versus the time passed after the field step at three different constant fields varying from the coercive field (-750 Oe) to the negative saturation field (-2400 Oe). All curves are measured along the easy axis direction. The maximum time dependence of magnetization is near the coercive field and there is almost no change in magnetic moment far away from the coercive field i.e at the negative saturation field. Figure 4.22 shows the variation of change in magnetization with applied fields measured along the easy axis (90 degrees), hard axis (0 degrees) and the axis between these two extremes (45 degrees). The

maximum change in magnetic moment is found along the easy axis and the minimum change in magnetic moment is along the hard axis.

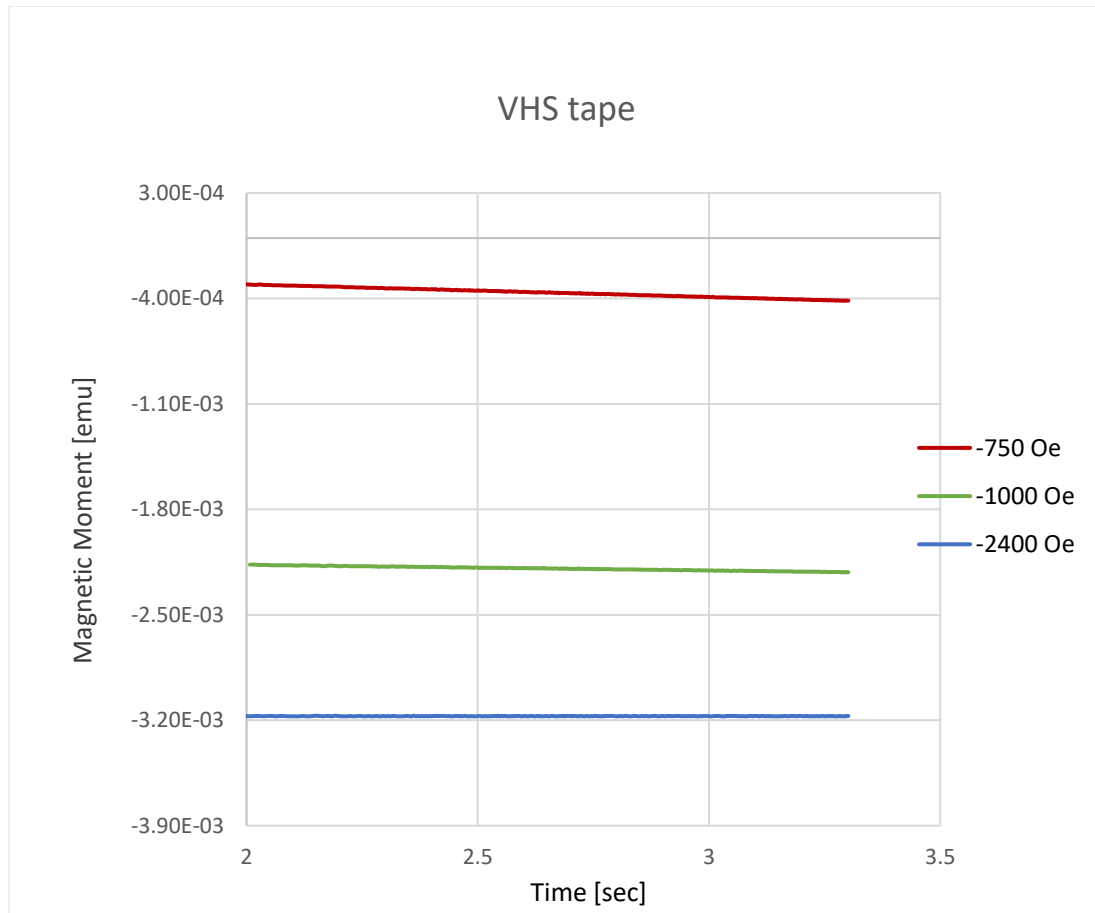


Figure 4. 21. Decay of magnetic moment in the presence of the constant magnetic fields of VHS tape.

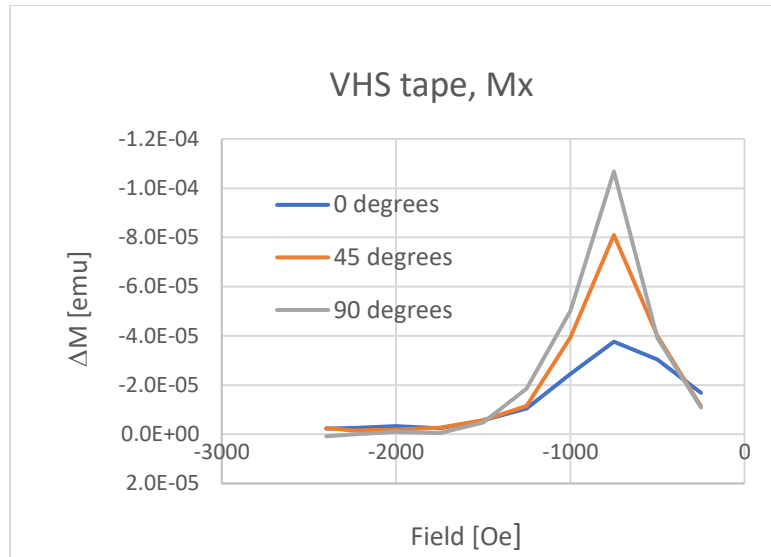


Figure 4. 22. Variation of change of magnetic moment with the applied fields of VHS tape.

4.2.4.3 Time-dependent slope of $\text{Ni}_{0.81}\text{Fe}_{0.19}$ sample

The time-dependent measurements of the $\text{Ni}_{0.81}\text{Fe}_{0.19}$ sample sputtered in the magnetic field when using the data from 100 to 2000 seconds are shown below. The measurements were done at room temperature along with three different angles: 0 degrees (easy axis direction), 90 degrees (hard axis direction) and 45 degrees. Figure 4.23 shows the variation of slopes of both X coils signals. It has been shown that the slope is maximum along the easy axis and minimum along the hard axis. The slope is maximum near the coercive field (-99 Oe) and decreases on either side. Figure 4.24 shows the variation of the slope of Y-coils signals. For the measurements that were done along easy axis has a negative slope at -149 Oe; however strange behavior is observed in the Y-signal that was measured along the hard axis (at 90 degrees). It has a positive slope at -99 Oe. All M_y -signals are smaller in magnitude than M_x -signals shown in figure 4.25. It can be seen that

the high slope of x-signals for easy axis measurements shifts towards the lower field and y-signals shift towards the higher field. But the situation is different for hard axis measurements i.e the time-dependent of both signals look similar.

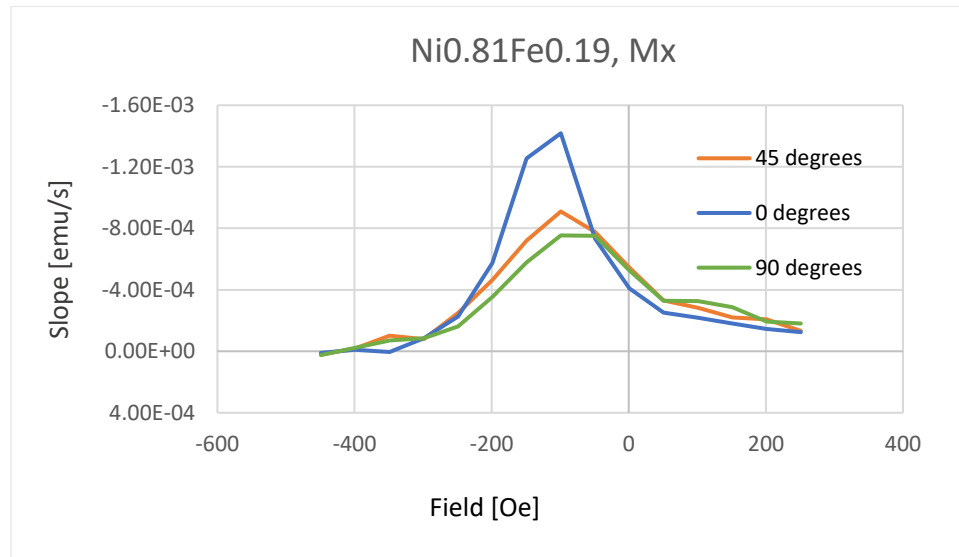


Figure 4. 23. Variation of X- signal slope with applied fields of o Ni_{0.81}Fe_{0.19} sample.

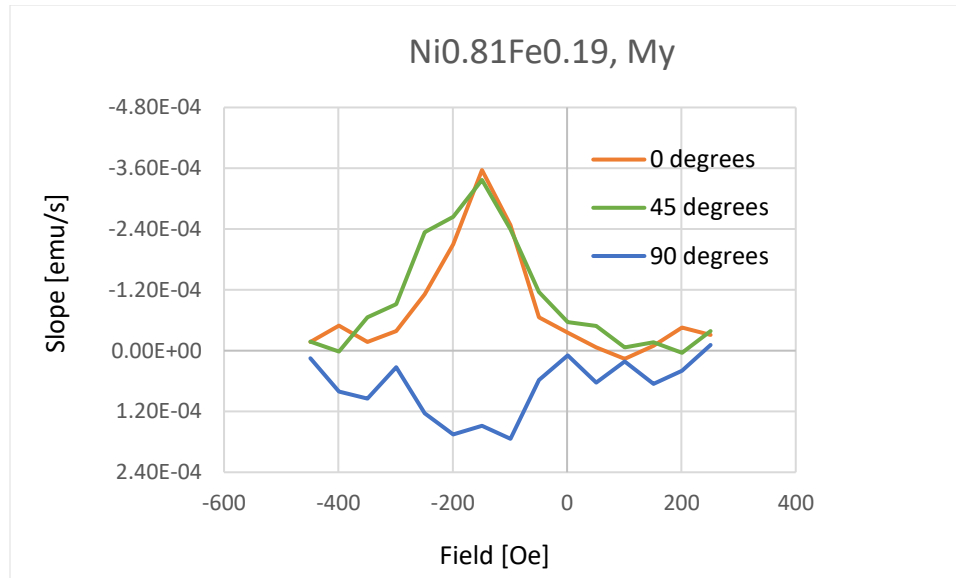
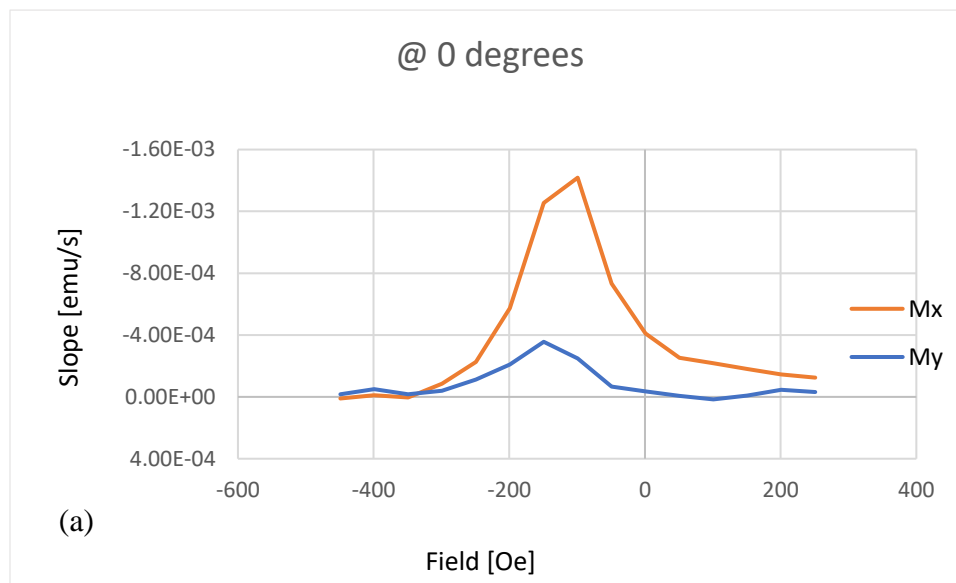


Figure 4. 24. Variation of the Y-signal slope with an applied field of $\text{Ni}_{0.81}\text{Fe}_{0.19}$ sample.



(a)

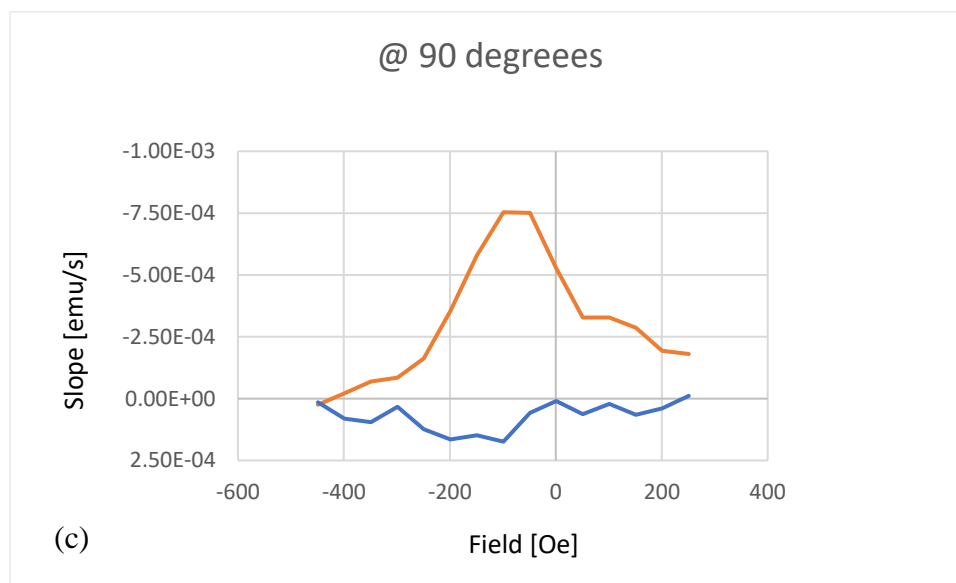
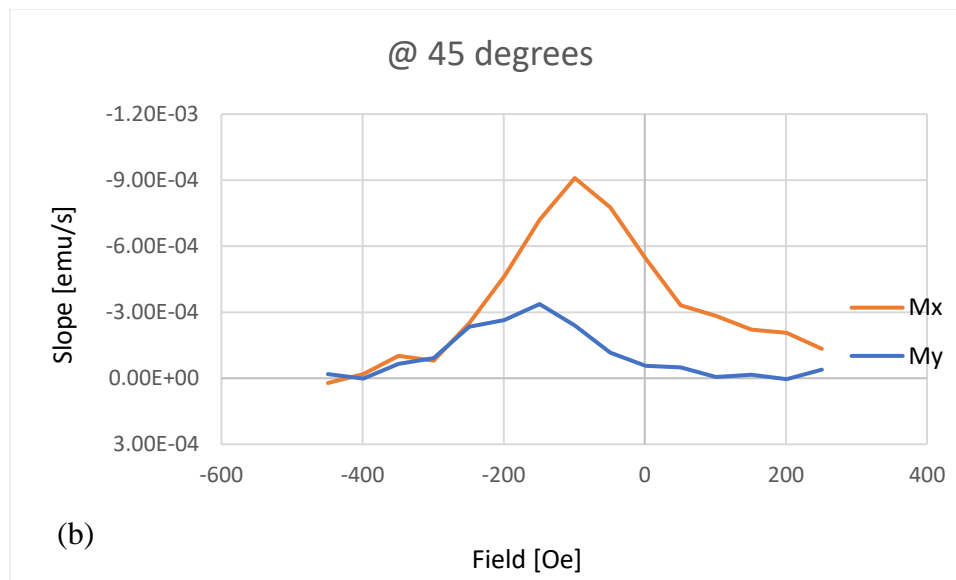


Figure 4. 25. Comparison of variation of slope of M_x and M_y signals of $Ni_{0.81}Fe_{0.19}$ samples measured at (a) 0 degrees, (b) 45 degrees and (c) 90 degrees.

4.2.5 Angle-dependent coercivity of Ni_{0.81}Fe_{0.19} sample

Angular measurements were done on a Permalloy thin film sputtered on Si. The sample was sputtered in a magnetic field of 1500 Oe. The hysteresis curves were measured for different field angles. Prior to the measurements, the sample was aligned at zero-degree field angle. No angular sensitivity correction was applied but the raw data was corrected for the image effect and for the background signal of the sample rod. Since the sample is sputtered in a magnetic field, it is believed that it has a field induced anisotropy. The field-induced easy axis originates from the preferential orientations of the NiFe bonds with respect to the applied magnetic field during deposition. The angular dependence of the coercivity is shown in figure 4.26 below. It has been shown that the coercivity is minimum along the hard axes i.e at 90, and 270 degrees and a maximum along the easy axes i.e 0, 135, 315 and 360 degrees. The effect is small but noticeable.

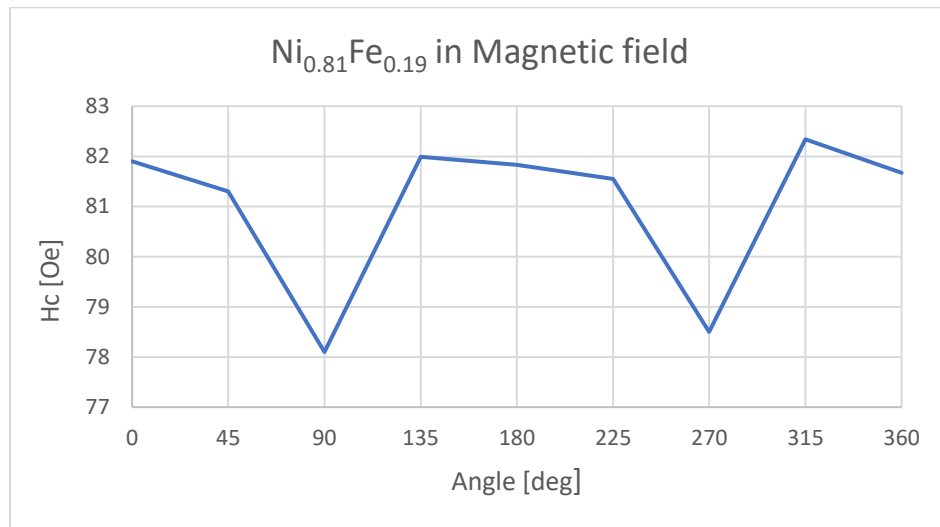


Figure 4. 26. Variation of coercivity of NiFe sample.

5 OVERALL SUMMARY

In this thesis research, the properties of RF sputtered Permalloy and Permalloy oxide thin films were investigated. Specifically (1) XPS was used to investigate the chemical state of reactive RF sputtered Permalloy oxide thin films that can be used as memory medium in RRAM devices; (2) XRD was used to study the texture of thin RF sputtered Permalloy films doing pole figure measurements on samples sputtered in a magnetic field.

Permalloy films with a field-induced magnetic anisotropy find wide application in spintronic devices and novel sensors; (3) Two VSAs were used to explore various magnetic properties of both Permalloy and Permalloy-oxide thin films at room temperature. (4) Additional magnetic measurements were performed on floppy disk samples and VHS tape samples to unravel the biaxial, the IRM/DCD, and the time-dependent measurement methods. A better understanding of how size and sample position affect the angular sensitivity variation was targeted.

Here the most important conclusions of this thesis work are summarized:

1. XPS and magnetic study of reactive RF-sputtered NiFeO thin films: In the study of the deposition process of Permalloy oxide thin films it is found that at low oxygen flow rates, the deposition rate increases with oxygen flow. This increase is due to the introduction of oxygen in the system resulting in the oxidation of the freshly deposited Permalloy film. At higher oxygen flow, i.e. above 5 sccm, the deposition rate decreases strongly. We believe that this is caused by the oxidation of the targets. Theory shows that NiFe-Oxide has a rock salt structure and is antiferromagnetic. Similarly, to NiO powder,

reactive RF-sputtered Permalloy oxide thin films have a small magnetic moment that depends on the oxygen concentration during the deposition process. A decrease in the saturation magnetization is observed for higher oxygen flows. This might be due to a more fully oxidation of the films sputtered at high oxygen flow. A sharp decrease in the magnetic moment was observed when the oxygen flow was increased above 1.25 sccm. The XPS study shows that the ratio of the Ni⁰ to Ni²⁺ decreases with oxygen flow, and that the films sputtered at 20 sccm oxygen flow are fully oxidized. The Fe-XPS spectra of the films sputtered at a different oxygen flow look very similar to each other. The absence of a distinct Fe⁰ peak suggests that most Fe is oxidized, and oxygen vacancies prefer to reside next to nickel atoms. This conclusion is in agreement with the DFT calculations of John Peterson.

2. XRD texture measurements on Permalloy thin films.

XRD measurements on Permalloy thin films on silicon show that one can get rid of the large substrate (silicon) peak by rotating chi or rotating omega and phi. It is best to rotate chi rather than to rotate Omega and phi as the former will have a smaller impact on the Permalloy film peaks. The result shows that chi should be rotated by at least 5 degrees for the complete removal of silicon peak without affecting the film peak.

The sputter gas pressure field during the RF deposition of Permalloy influences the films texture. The pole figure measurements show a strong (111) texture along with a parasitic (220) texture for the samples sputtered at high gas pressure (30 sccm). For the samples sputtered at low gas pressure (5 sccm) samples, a competing (200)/ (111) texture is observed. The texture of Permalloy also depends on the thickness. The pole figure data of

the sample sputtered in the magnetic field shows stronger texture than samples sputtered without the magnetic field of the same thickness. We believe that this is caused by the preferential orientation of magnetic grains. A thorough analysis was performed to correct the pole figures measured of Permalloy thin films sputtered on 3" fused quartz wafers for (a) the background of the substrate; (b) the absorption in the film; (c) and defocusing issues. To do the defocusing correction, a Ni defocusing calibration sample was realized from Ni-powder, a fused quartz wafer, and double-sided tape. Corrected pole figures depend on measurement conditions revealing that the corrections are not complete and performing quantitative pole figure measurements on Permalloy films below 500 nm might not be possible.

3. Magnetic properties of Permalloy thin films:

DCD and IRM measurements show negative interactions between the domains of the Permalloy film. The time-dependent measurement results of the Permalloy sample sputtered in a magnetic field show that the time dependence is maximum at or near the coercive field and decreases on either side. For the Permalloy sample, the slope is maximum along the easy axis and minimum along the hard axis. Furthermore, the high slope of x-signals for easy axis measurements shift towards the lower field and y-signals shift towards the higher field but for the hard axis time-dependent both signals look similar

4. Magnetic case studies on floppy and VHS samples to better understand the

MicroSense VSM and its measurement methods:

Measurements on samples cut from a 3.5" floppy disk show that the sample position of the sample rod, the sample asymmetry, the angular dependence of the sample rod

position (wobble), and the magnetic anisotropy all influence the angular dependence of the measured hysteresis curve. As it is challenging to separate those contributions from each other, it is recommended that the sample is re-centered after each field angle change, so all measurements are made with the sample at exactly the same position. Therefore, the measured moment of an isotropic circular symmetric sample is field angle independent and contains no cross-talk terms. For such a measurement strategy, the angular sensitivity calibration curve can be used to compensate for the sample's asymmetry. Expressions for the sensitivity and the cross-talk of a Mallinson biaxial VSM pick-up coil set were derived for a point sample saturated along the x, y, or z-axis. These 3D functions were used to determine the x, y, and θ dependence of the X-coil and Y-coil sensitivities ($S_{xx}(x)$, $S_{xx}(y)$, $S_{xx}(\theta)$, $S_{xy}(x)|_{y=c}$, $S_{xy}(y)|_{x=c}$, $S_{xy}(\theta)$). $S_{xx}(x)$ and $S_{xx}(y)$ are parabolic. The cross-talk terms $S_{xy}(x)|_{y=c}$ and $S_{xy}(y)|_{x=c}$ are odd functions. The angular sensitivity and angular cross-talk, $S_{xx}(\theta)$ and $S_{xy}(\theta)$ contain θ and 2θ components. The calculations suggest that the amplitude ratio and phase difference between the θ and 2θ terms in the $S_{xx}(\theta)$ curve can be used to estimate the coordinates of the wobble center in the coordinate system of the x-coils. The wobble radius can be estimated from the amplitude of the symmetric sensitivity function. The amplitude ratio and phase difference between the θ and 2θ terms in the $S_{xy}(\theta)$ curve can be used to estimate the coordinates of the wobble center in the coordinate system of the y-coils.

For future research, it would be interesting to replace the micrometers for the x and y sample position control with step motors that can be controlled by the computer. This will allow the sample position to be adjusted after each field angle change and keep the

cross-talk zero and the sensitivity independent of the field angle. The angular sensitivity calibration of the MicroSense system can then be used to compensate for an asymmetric sample shape. Furthermore, it would be interesting to further explore how the normalized angular sensitivity of the X-coils and the normalized angular cross talk can be used to optimize the sample position to reduce or eliminate cross talk.

REFERENCES

- [1] Chang Liu *et al.*, “Out-of-plane permalloy magnetic actuators for delta-wing control,” no. February 1995, p. 7, 2005.
- [2] K. J. M. Eijkel, “A thin-Film Magnetoresistive Angle Detector, thesis, research carried out at the Twente University of Technology TDM faculty of the Electronical Engineering, The Netherlands,” pp. 9–164, 1959.
- [3] R. M. de Rider, “Thin-Film Magnetoresistive Magnetometer, thesis, research carried out at University Twente, The Netherlands,” pp. 6–153, 1988.
- [4] Anna A. Chlenova *et al.*, “Permalloy-Based Thin Film Structures: Magnetic Properties and the Giant Magnetoimpedance Effect in the Temperature Range Important for Biomedical Applications,” *Sensors*, vol. 17, no. 8, p. 8, 2017.
- [5] J. P. J. Groenland, “Thin-Film Magnetoresistive Absolute Position Detector, Thesis, research carried out at University of Twente, the Netherlands,” no. 7–129, pp. 2780–2788, 1990.
- [6] T. R. M. A. R. I. POTTER, “Anisotropic Magnetoresistance in Ferromagnetic 3d Alloys,” *IEEE Trans.*, vol. 11, no. 4, pp. 1–9, 1975.
- [7] I. Hotovy, J. Huran, L. Spiess, S. Hascik, and V. Rehacek, “Preparation of nickel oxide thin films for gas sensors applications,” *Sensors Actuators, B Chem.*, vol. 57, no. 1–3, pp. 147–152, 1999.
- [8] G. Mihajlović *et al.*, “Enhanced spin signals due to native oxide formation in Ni₈₀Fe₂₀ /Ag lateral spin valves,” *Appl. Phys. Lett.*, vol. 97, no. 11, pp. 1–4, 2010.

- [9] G. McMahon *et al.*, “Hematite-Based Water Splitting with Low Turn-On Voltages,” *Angew. Chemie Int. Ed.*, vol. 52, no. 48, pp. 12692–12695, 2013.
- [10] S. E. Rios, A. K. Bandyopadhyay, C. Smith, and C. J. Gutierrez, “The enhancement of magnetically ordered oxide layered structures using oxygen radical processing,” *J. Magn. Magn. Mater.*, vol. 286, no. SPEC. ISS., pp. 455–462, 2005.
- [11] I. R. Harris and A. J. Williams, “Magnetic Materials, (School of Metallurgy and Materials, University of Birmingham, Birmingham, UK), Materials Science and Engineering— Magnetic Materials (2009).,” vol. II.
- [12] P. Prieto, J. Camarero, J. F. Marco, E. Jiménez, J. M. Benayas, and J. M. Sanz, “Characterization of nanocrystalline permalloy thin films obtained by nitrogen IBAD,” *IEEE Trans. Magn.*, vol. 44, no. 11 PART 2, pp. 3913–3916, 2008.
- [13] Z. Ali, “Growth, Transport, and Magnetic properties of oblique-angle deposited permalloy thin films, A Thesis Submitted to the Faculty of Miami University in partial fulfillment of the requirements for the degree of Master of Science Miami University Oxford, Ohio,” p. 103, 2008.
- [14] O. D. Roshchupkina, T. Strache, J. McCord, A. Mücklich, C. Bähz, and J. Grenzer, “Structural modifications of thin magnetic Permalloy films induced by ion implantation and thermal annealing: A comparison,” *Acta Mater.*, vol. 74, pp. 278–284, 2014.
- [15] J. C. A. Huang, T. E. Wang, C. C. Yu, Y. M. Hu, P. B. Lee, and M. S. Yang, “Permalloy.Pdf,” vol. 171, pp. 442–446, 1997.

- [16] E. B. Park, S. U. Jang, J. H. Kim, and S. J. Kwon, "Induced magnetic anisotropy and strain in permalloy films deposited under magnetic field," *Thin Solid Films*, vol. 520, no. 18, pp. 5981–5984, 2012.
- [17] X. Li, X. Sun, J. Wang, and Q. Liu, "Magnetic properties of permalloy films with different thicknesses deposited onto obliquely sputtered Cu underlayers," *J. Magn. Mater.*, vol. 377, pp. 142–146, 2015.
- [18] G. Wang *et al.*, "Observation of rotatable stripe domain in permalloy films with oblique sputtering," *J. Appl. Phys.*, vol. 112, no. 9, 2012.
- [19] M. Goto, H. Tange, and T. Kamimori, "Thickness Dependence Of Field induced Uniaxial Anisotropy," *J. Magn. Mater.*, vol. 62, pp. 251–255, 1986.
- [20] M. Romera, R. Ranchal, D. Ciudad, M. Maicas, and C. Aroca, "Magnetic properties of sputtered Permalloy/molybdenum multilayers," *J. Appl. Phys.*, vol. 110, no. 8, 2011.
- [21] M. Maicas, R. Ranchal, C. Aroca, P. Sánchez, and E. López, "Magnetic properties of permalloy multilayers with alternating perpendicular anisotropies," *Eur. Phys. J. B*, vol. 62, no. 3, pp. 267–270, 2008.
- [22] F. Czerwinski, J. A. Szpunar, and U. Erb, "Structural and magnetic characterization of nanocrystalline Ni-20%Fe permalloy films," *J. Mater. Sci. Mater. Electron.*, vol. 11, no. 3, pp. 243–251, 2000.
- [23] C. S. Ha and Y. B. Park, "Development of Growth Texture in Nanocrystalline Fe-Ni Alloys," *Mater. Sci. Forum*, vol. 495–497, no. September 2005, pp. 749–754, 2009.

- [24] Y. B. Park, J. Park, C. S. Ha, and T. H. Yim, "Texture and Grain Growth in Nanocrystalline Permalloy * Department of Materials Science and Metallurgical Engineering , Korea Institute of Industrial Technology , Chonan 330-820 , Korea," pp. 1–4.
- [25] H. Li, F. Czerwinski, and J. A. Szpunar, "Monte-Carlo simulation of texture and microstructure development in nanocrystalline electrodeposits," *Nanostructured Mater.*, vol. 9, no. 1–8, pp. 673–676, 1997.
- [26] J. H. Seo, J. K. Kim, T. H. Yim, and Y. B. Park, "Textures and Grain Growth in Nanocrystalline Fe-Ni Alloys," *Mater. Sci. Forum*, vol. 475–479, pp. 3483–3488, 2009.
- [27] D. N. Lee, "Changes in Lattice Constants and Orientation of <100> and <111> Grains in Nanocrystalline Ni and Ni-Fe Electrodeposits after Annealing," *Mater. Sci. Forum*, vol. 539–543, no. January, pp. 149–154, 2009.
- [28] S. F. Cheng, P. Lubitz, Y. Zheng, and A. S. Edelstein, "Effects of spacer layer on growth, stress and magnetic properties of sputtered permalloy film," *J. Magn. Magn. Mater.*, vol. 282, no. 1–3, pp. 109–114, 2004.
- [29] M. Kateb, E. Jacobsen, and S. Ingvarsson, "Application of an extended van der Pauw method to anisotropic magnetoresistance measurements of ferromagnetic films," *J. Phys. D. Appl. Phys.*, vol. 52, no. 7, pp. 1–10, 2019.
- [30] Y. H. Lin *et al.*, "Ferromagnetism and electrical transport in Fe-doped NiO," *Phys. Rev. B - Condens. Matter Mater. Phys.*, vol. 73, no. 19, pp. 3–6, 2006.
- [31] A. P. Douvalis, L. Jankovic, and T. Bakas, "The origin of ferromagnetism in 57Fe-doped NiO," *J. Phys. Condens. Matter*, vol. 19, no. 43, pp. 0–25, 2007.

- [32] F. J. Twagirayezu, M. A. A. Talukder, and W. J. Geerts, "Magnetic properties of RF-sputtered NiO and Ni_{0.8}Fe_{0.2}O_{1-δ} samples grown on SiO₂/Si substrates," *Mater. Res. Innov.*, vol. 00, no. 00, pp. 1–8, 2018.
- [33] A. C. Gandhi *et al.*, "Understanding the Magnetic Memory Effect in Fe-Doped NiO Nanoparticles for the Development of Spintronic Devices," *ACS Appl. Nano Mater.*, vol. 2, no. 1, pp. 278–290, 2019.
- [34] K. O. Moura, R. J. S. Lima, C. B. R. Jesus, J. G. S. Duque, and C. T. Meneses, "Fe-doped NiO Nanoparticles: Synthesis, Characterization, and Magnetic Properties," *Rev. Mex. Física S*, vol. 58, no. 2, pp. 167–170, 2012.
- [35] P. M. Ponnusamy *et al.*, "Structural, optical and magnetic properties of undoped NiO and Fe-doped NiO nanoparticles synthesized by wet-chemical process," *Mater. Charact.*, vol. 114, pp. 166–171, 2016.
- [36] S. Manna, A. K. Deb, J. Jagannath, and S. K. De, "Synthesis and room temperature ferromagnetism in Fe doped NiO nanorods," *J. Phys. Chem. C*, vol. 112, no. 29, pp. 10659–10662, 2008.
- [37] S. Liu *et al.*, "Synthesis of Fe-doped NiO nanofibers using electrospinning method and their ferromagnetic properties," *J. Magn. Magn. Mater.*, vol. 324, no. 13, pp. 2070–2074, 2012.
- [38] J. Wang, J. Cai, Y. H. Lin, and C. W. Nan, "Room-temperature ferromagnetism observed in Fe-doped NiO," *Appl. Phys. Lett.*, vol. 87, no. 20, pp. 1–3, 2005.

- [39] J. Khemprasit, S. Kaen-Ngam, B. Khumpaitool, and P. Kamkhou, "Effects of calcining temperature on structural and magnetic properties of nanosized Fe-doped NiO prepared by diol-based sol-gel process," *J. Magn. Magn. Mater.*, vol. 323, no. 18–19, pp. 2408–2412, 2011.
- [40] S. Foner, "Versatile and Sensitive Vibrating-Sample Magnetometer," *Rev. Sci. Instrum.*, vol. 30, no. 7, 1959.
- [41] MicroSense, "Easy VSM manual, Operating software for the MicroSense Vibrating Sample Magnetometer."
- [42] Sakshat Virtual Labs, "Free Vibration of a Cantilever Beam (Continuous System)," *Indian Inst. Technol.*, no. M, pp. 1–6, 2012.
- [43] "Pipe and Tubing Formulas,
<http://www.kellypipe.com/assets/files/pipeformulas.pdf>."
- [44] MicroSense, "EZ Vibrating Sample Magnetometers (Accessed: December 1, 2016.) <http://www.microsense.net/products-vsm.htm>."
- [45] E. Samwel, "Magnetic characterization of Recording materials: Design, Instrumentation and Experimental method. Chapter.4, p. 81-72," in *Research carried out at University of Twente, The Netherlands*, 1995.
- [46] NPTEL, "Introduction Lecture 05 : Soft and Hard magnetic materials and Stoner-Wohlfarth theory (Accessed: 26 November,2013).<https://nptel.ac.in/courses/115103038/5>," pp. 17–20, 2019.
- [47] S. Chikazumi, "Physics of Ferromagnetism," *J. Chem. Inf. Model.*, vol. 53, no. 9, pp. 1–649, 1996.

- [48] “AJA International Inc, Sputtering system; <http://www.ajaint.com/sputtering-systems.html>.”
- [49] N. R. Murphy, L. Sun, J. T. Grant, J. G. Jones, and R. Jakubiak, “Molybdenum Oxides Deposited by Modulated Pulse Power Magnetron Sputtering: Stoichiometry as a Function of Process Parameters,” *J. Electron. Mater.*, vol. 44, no. 10, pp. 3677–3686, 2015.
- [50] M. Klicpera, P. Javorský, and M. Diviš, “Magnetization and electrical resistivity measurements on CeCuAl₃ single crystal,” *J. Phys. Conf. Ser.*, vol. 592, no. 1, 2014.
- [51] “‘Privacy Policy’, Physical Property Measurement System (PPMS), Quantum Design Inc., <http://www.qdusa.com/products/ppms.html> (Accessed, April 6, 2017).,” pp. 1070–150.
- [52] J. Hack, M. H. Ludwig, W. Geerts, and R. E. Hummel, “Ferromagnetic Properties of Spark-Processed Photoluminescing Silicon,” *MRS Proc.*, vol. 452, pp. 147–152, 1996.
- [53] E. O. Samwel, T. Bolhuis, and J. C. Lodder, “An alternative approach to vector vibrating sample magnetometer detection coil setup,” *Rev. Sci. Instrum.*, vol. 69, no. 9, pp. 3204–3209, 1998.
- [54] Fidele J. Twagirayezu, “Theoretical and experimental determination of properties of NiO and Fe-doped NiO,” *A thesis Submitt. to Grad. Counc. Texas State Univ. Partial fulfillment Requir. degree Master Sci. with a Major Phys. August, 2017.*

- [55] M. A. A. Talukder, Y. Cui, M. Compton, W. Geerts, L. Scolfaro, and S. Zollner, "FTIR Ellipsometry Study on RF sputtered Permalloy-Oxide Thin Films," *MRS Adv.*, vol. 1, no. 49, pp. 3361–3366, 2016.
- [56] A. K. Bandyopadhyay, S. E. Rios, A. Tijerina, and C. J. Gutierrez, "The influence of ion beam sputtering geometry on metastable (Ni₈₁Fe₁₉)O/Ni₈₁Fe₁₉ exchange biased bilayers," *J. Alloys Compd.*, vol. 369, no. 1–2, pp. 217–221, 2004.
- [57] J. E. Petersen, F. Twagirayezu, L. M. Scolfaro, P. D. Borges, and W. J. Geerts, "Electronic and optical properties of antiferromagnetic iron doped NiO - A first principles study," *AIP Adv.*, vol. 7, no. 5, 2017.
- [58] "Privacy policy, X-ray Photoelectron Spectroscopy, <http://www.elettra.trieste.it/lightsources/labs-and-services/surface-lab/x-ray-photoelectron-spectroscopy.html> (Accessed on 4 October 2012).," pp. 1–17.
- [59] J. F. Watts and J. Wolstenholme, "An Introduction to Surface Analysis by XPS and AES," p. 224, 2003.
- [60] C. D. Wagner, W. M. Riggs, L. E. Davis, J. F. Moulder, and G. E. Muilenberg, "Handbook of x-ray photoelectron spectroscopy : a reference book of standard spectra for identification and interpretation of XPS data - Catalog - UW-Madison Libraries," p. 261, 1995.
- [61] M. Salou, B. Lescop, S. Rioual, A. Lebon, J. Ben Youssef, and B. Rouvellou, "Initial oxidation of polycrystalline Permalloy surface," *Surf. Sci.*, vol. 602, no. 17, pp. 2901–2906, 2008.

- [62] S. Uhlenbrock, C. Scharfschwerdt, M. Neumann, G. Illing, and H. J. Freund, "The influence of defects on the Ni 2p and O 1s XPS of NiO," *J. Phys. Condens. Matter*, vol. 4, no. 40, pp. 7973–7978, 1992.
- [63] W. L. Bragg, "The diffraction of short electromagnetic waves," *Proc. Camb. Phil. Soc*, vol. 17, no. 45, p. 43, 1913.
- [64] C. M. C. Dutrow Barbara L, "Geochemical Instrumentation and Analysis, X-ray Powder Diffraction (XRD)," vol. 2015, pp. 4–7.
- [65] P. Schiebel, "Determination of the Rocking Curve and Reflection Efficiency of a Quartz Crystal X-ray Imager," 2012.
- [66] Fewster and M. Birkholz, *Thin Film Analysis by X-ray*. 2006.
- [67] R. L. S. S.T. Misture, "Preferred orientation, Encyclopedia of Materials: Science and Technology," pp. 1–14, 2001.
- [68] C. V Thompson and R. Carel, "MATERIALS SCIENCE & ENGINEERING B Texture development in polycrystalline thin films," vol. 32, no. 95, pp. 211–219, 1995.
- [69] D. B. Knorr and D. P. Tracy, "A review of microstructure in vapor deposited copper thin films," *Mater. Chem. Phys.*, vol. 41, no. 3, pp. 206–216, 1995.
- [70] K. Nagao and E. Kagami, "X-ray thin film measurement techniques: VII. Pole figure measurement," *Rigaku J.*, vol. 27, no. 2, pp. 6–14, 2011.
- [71] P. Walker, "*X-ray texture analysis of CVD diamond*", thesis May 2018. .
- [72] H. Omar, "Intensity Correction and Pole Figure Measurement of Copper Metallic by XRD," *J. Basic Appl. Sci.*, vol. 12, pp. 320–322, 2016.
- [73] P. Walker, "X-ray Texture analysis of CVD diamond," no. May, 2018.

- [74] J. C. Woolley and R. Street, "A Study of Magnetic Viscosity," *Proc. Phys. Soc. Sect. A*, vol. 62, no. 9, pp. 562–572, 2002.
- [75] M. P. Sharrock, "Time-dependent magnetic phenomena and particle-size effects in recording media," *IEEE Trans. Magn.*, vol. 26, no. 1, pp. 193–197, 1990.
- [76] J. P. . Bernards, "Design of a detection coil system for a biaxial vibrating sample magnetometer and some applications," *Rev. Sci. Instrum.*, vol. 64, no. 7, pp. 1918–1930, 1993.
- [77] D. J. Griffiths, *Introduction to Electrodynamics Fourth Edition*. 1999.
- [78] A. F. Gregory, "The Effect of plastic deformation on a series of thin magnetic films," *Thesis*, no. December, 2010.
- [79] X. Xu, A. Sun, X. Jin, H. Fan, and X. Yao, "Method for calculating the induced voltage in a vibrating sample magnetometer detection coil system," *Rev. Sci. Instrum.*, vol. 67, no. 11, pp. 3914–3923, 1996.
- [80] C. P. . S. J.P.C. Benards, "Co-Cr layers for perpendicular magnetic recording," *Thesis*, 1959.
- [81] A. Lisfi, S. Pokharel, O. Akioya, N. H. Alqhtany, and M. Wuttig, "Irreversible magnetization process and switching mechanism in L10 FePt thin films," *AIP Adv.*, vol. 7, no. 5, 2017.
- [82] K. O. A.M. de Witte, "Activation volumes in ultrfine paricles and recording media," *J. Magn. Magn. Mater.* 88 183-193, vol. 88, pp. 183–193, 1990.
- [83] C. Serletis and K. G. Efthimiadis, "On the measurement of magnetic viscosity," *J. Magn. Magn. Mater.*, vol. 324, no. 16, pp. 2547–2552, 2012.